

Department of Physics and Astronomy
University of Heidelberg

Master thesis in Physics
submitted by
Christopher Fuchs
born in Mutlangen
2019

**Imaging of volcanic trace gases by
Fabry-Perot interferometer correlation spectroscopy**

This Master thesis has been carried out by

Christopher Fuchs

at the

Institute of Environmental Physics

under the supervision of

Prof. Dr. Ulrich Platt

Imaging of volcanic trace gases by Fabry-Perot interferometer correlation spectroscopy:

Imaging of atmospheric trace gas distributions by optical remote sensing allows for a direct assessment of the dynamics of both physical and chemical processes. In particular, the fast evolution of trace gases emitted by point sources (e.g., volcanic plumes) can be studied comprehensively by imaging approaches.

Presently applied imaging techniques still either lack in spatio-temporal resolution like, e.g., Imaging DOAS or in selectivity and sensitivity like sulphur dioxide (SO₂) cameras.

Throughout this thesis, a novel imaging approach based on Fabry-Perot interferometer correlation spectroscopy (FPI CS) is presented. The technique exploits the periodic transmission profile of a Fabry-Perot interferometer (FPI) and its correlation to the (approximately periodically varying) target trace gas spectral absorbance.

The feasibility of the novel technique for SO₂, bromine monoxide (BrO), and formaldehyde (HCHO) is examined in a model study. A prototype of a one-pixel FPI instrument for HCHO is characterised and tested in the laboratory yielding a good agreement between the modelled and measured sensitivity for HCHO. The sensitivity (weighted mean trace gas absorption cross section) of the one-pixel HCHO instrument is $2.28 \times 10^{-20} \text{ cm}^2 \text{ molec}^{-1}$. From the HCHO sensitivity, a BrO sensitivity of $6.21 \times 10^{-18} \text{ cm}^2 \text{ molec}^{-1}$ can be inferred due to the spectral similarity of the BrO and HCHO absorption cross section. Finally, an imaging FPI CS prototype is designed, built, and tested in field measurements. The SO₂ detection limit of $3.8 \times 10^{17} \text{ molec cm}^{-2} \text{ s}^{-1/2}$ is comparable to present SO₂ cameras, however, the selectivity is drastically increased. FPI CS therefore shows a promising potential to allow for fast imaging measurements of most of the trace gases that can be measured by DOAS.

Bildgebende Fernerkundung vulkanischer Spurengase mittels Fabry-Perot Interferometer Korrelationsspektroskopie:

Bildgebende Messungen atmosphärischer Spurengase, durch optische Fernerkundung, ermöglichen eine direkte Abschätzung der Dynamik von physikalischen und chemischen Prozessen. Insbesondere kann die Entwicklung von Spurengasen, die von Punktquellen wie Vulkanen emittiert werden, durch bildgebende Verfahren detailliert untersucht werden.

Den derzeit angewandten bildgebenden Messmethoden mangelt es jedoch entweder an räumlich und zeitlicher Auflösung wie bei der Imaging-DOAS Technik, oder an Selektivität und Empfindlichkeit, wie bei Schwefeldioxid (SO₂) Kameras.

In dieser Arbeit wird ein neuartiger Ansatz für eine bildgebende Technik vorgestellt, die Fabry-Perot Interferometer Korrelationsspektroskopie (FPI CS). Das grundlegende Prinzip dieser Technik basiert auf dem periodischen Transmissionsspektrum eines Fabry-Perot Interferometer (FPI) und dessen Korrelation mit der (idealerweise periodischen) spektralen Absorption des Spurengases.

In einer Modellstudie wird die Anwendbarkeit der neuen Methode auf SO₂, Brommonoxid (BrO) und Formaldehyd (HCHO) untersucht. Ein Ein-Pixel FPI Prototyp für HCHO wird im Labor charakterisiert und getestet. Es wird gezeigt, dass eine gute Übereinstimmung zwischen modellierten und gemessenen Daten vorliegt. Die Empfindlichkeit (gewichteter mittlerer Absorptionswirkungsquerschnitt) des Ein-Pixel HCHO Gerätes beträgt $2.28 \times 10^{-20} \text{ cm}^2 \text{ molec}^{-1}$. Aufgrund der spektralen Ähnlichkeit der Absorptionswirkungsquerschnitte von HCHO und BrO kann eine BrO Empfindlichkeit von $6.21 \times 10^{-18} \text{ cm}^2 \text{ molec}^{-1}$ abgeleitet werden. Letztlich, wird eine bildgebende FPI-Kamera entwickelt und in Feldmessungen auf SO₂ angewendet. Die SO₂ Nachweisgrenze liegt bei $3.8 \times 10^{17} \text{ molec cm}^{-2} \text{ s}^{-1/2}$ und ist damit vergleichbar mit heutig genutzten SO₂ Kameras, besitzt jedoch eine deutlich erhöhte Selektivität. FPI CS ist daher eine vielversprechende Methode für schnelle bildgebende Messungen der meisten Spurengase, die auch über DOAS detektiert werden können.

Contents

1	Introduction	1
2	Theoretical Background	5
2.1	UV-Vis radiation in Earth's atmosphere	5
2.1.1	Elastic scattering	5
2.1.2	Inelastic Scattering	6
2.1.3	Absorption	7
2.1.4	Radiative transfer	7
2.2	Absorption Spectroscopy	8
2.2.1	Differential optical absorption spectroscopy	8
2.2.2	Impacts of DOAS instruments on the recorded intensity spectrum	11
2.3	Imaging of atmospheric trace gases	12
2.3.1	Imaging DOAS	12
2.3.2	The SO ₂ camera	13
2.4	Fabry-Perot Interferometer Correlation Spectroscopy	15
2.4.1	The Fabry-perot Interferometer	15
2.4.2	Trace gas detection by FPI Correlation Spectroscopy	18
3	Model study	21
3.1	The FPI instrument response model	21
3.2	Model parameters and results	23
3.2.1	Model results for SO ₂	25
3.2.2	Model results for BrO	25
3.2.3	Model results for HCHO	27
4	The realistic Fabry-Perot Interferometer	31
4.1	The FPI wedge angle alignment	33
4.2	Determination of the FPI zero position	34
4.3	Determination of the FPI plate distance	36
5	The one-pixel FPI instrument	37
5.1	The one-pixel FPI instrument setup	37
5.2	Output noise characterisation	38
5.3	Selection of a suitable light source for calibration	40
5.4	Trace gas detection with the OP FPI	42
5.4.1	Preparation and experimental handling of HCHO gas cells	42

5.4.2	Experimental setup	43
5.4.3	Interferograms of HCHO	44
5.4.4	Two FPI-position measurements of HCHO	46
6	The FPI imaging instrument	51
6.1	Optical setup of the FPI camera	51
6.2	The imaging detector	53
6.3	The stepper motor	54
6.4	Electronic setup	55
6.5	The complete FPI-camera setup	56
6.6	Calibration of the stepper motor position	58
6.7	SO ₂ measurements: Mt. Etna	59
6.7.1	Calibration of the FPI camera AA	60
6.7.2	Evaluation of the FPI camera measurement	62
6.7.3	Estimation of SO ₂ emission rates	65
7	Conclusion & outlook	67
A	Appendix	71
A.1	Linearisation of AA_{FPI} for small column densities	71
A.2	BrO model results for filter with CWL 337 nm, 10 nm FWHM	72
A.3	The inclination angle inside the etalon due to the FPI wedge angles	73
B	Lists	75
B.1	List of Figures	75
B.2	List of Tables	76
C	Bibliography	77

1 Introduction

The atmosphere is one of the most fascinating systems that can be observed on our planet. It regulates various essential phenomena on Earth, for example, the greenhouse effect, weather conditions, and it supplies shielding against extraterrestrial high energy radiation. Thereby the atmosphere is facilitating life on Earth as we know it. Due to its vast complexity, many processes are still not entirely understood, revealing a big field for scientific research.

The main constituents of Earth's atmosphere are nitrogen ($\approx 78.1\%$), oxygen ($\approx 20.9\%$), and argon ($\approx 0.9\%$) making up 99.9% of the total composition. However, the multitude of trace gas species accounting for the remaining 0.1% have despite their low concentration, profound impacts on the physical and chemical processes within the atmosphere. For example, the increase of carbon dioxide from a pre-industrial level of 280 ppm to present values of 410 ppm (2019, NOAA) is amongst others greenhouse gases, the driving force of the human-induced climate change. Another interesting trace gas species is sulphur dioxide (SO_2) with atmospheric background mixing ratios < 1 ppb (Seinfeld and Pandis, 2016) for rural sites. It is one of the main agents causing acid rain and is capable of decreasing global temperature if it is injected into the stratosphere (Hansen et al., 1996).

Halogen radicals like e.g., Cl, Br, I, and their oxides like, e.g., ClO, BrO, IO are another important group of trace gas species and are present in the atmosphere with mixing ratios in the ppt regime (Saiz-Lopez and von Glasow, 2012). They are highly reactive and thereby short-lived and play an important role in the chemistry and oxidizing capacity of the atmosphere. For instance, they reduce the lifetime of the greenhouse gas methane or lead to the destruction of ozone (O_3) via autocatalytic reaction cycles.

Volcanoes are exceptional from many points of view, besides their touristic attraction and potential hazard to its periphery, they are capable of linking a multitude of different fields of recent scientific research. Volcanoes are strong point sources of various gas species, which are often emitted directly into the atmosphere. The composition of volcanic emission plumes is very different from other atmospheric environments. Therefore, the chemistry of volcanic plumes mixing with the atmosphere is still not well understood.

The quantification of volcanic degassing allows to study processes in Earth's interior. The gases are primarily exsolved from ascending magma in the volcanic conduit (Oppenheimer et al., 2014). The volcanic emissions can be used to monitor the activity and to draw conclusions on geological and geochemical processes. Some well-

1 Introduction

established tracers used for monitoring volcanoes are SO₂ emission rates (Salerno et al., 2009) or molar ratios between two trace gas species like, e.g., CO₂ to SO₂ (Aiuppa et al., 2007). These can be utilised as a proxy for volcanic activity as they often reveal strong variations previous to changes in the volcanic systems and eruptions.

A meanwhile well-established approach to investigate volcanic emissions is to use atmospheric remote sensing techniques. They allow continuous measuring from a safe distance so that even erupting volcanoes can be monitored. In this field, bromine monoxide (BrO) could be a potentially useful tracer for volcanic activity. BrO can be retrieved from UV scattered-sunlight spectra (via Differential Optical Absorption spectroscopy, DOAS), and the atmospheric background concentration of BrO is low compared to plume concentrations. This makes the retrieval by automated monitoring systems much easier in contrast to the retrieval of, e.g., CO₂ with high atmospheric background concentrations.

However, volcanoes do not emit BrO as a primary species (Bobrowski et al., 2007). Bromine already went through several reactions within the volcanic plume before it is detected as BrO. Due to the complex reaction kinetics of BrO many properties like, e.g., the chemistry limiting factors and timescales of the reactions are not well understood yet. Therefore, volcanic plumes are not only interesting for volcanological research but also for atmospheric chemistry.

An imaging technique able to resolve the spatial and temporal dynamics of halogen species, especially BrO, is therefore desirable. However, the latest applied imaging techniques are either too slow, e.g., Imaging DOAS (Louban et al., 2009), or exhibits a too weak sensitivity and selectivity, e.g., SO₂ cameras (Mori and Burton, 2006) and are hence not applicable to halogen species. Thus, there is an urgent need for novel measurement techniques that can give insight into fast and small-scale processes and that are deployable at volcanoes.

This thesis is continuing the work of Kuhn (2012, 2015) and Kuhn et al. (2014, 2019), by further investigating a novel technique for trace gas remote sensing of volcanic plumes. The requirements are to develop a non-dispersive imaging instrument that is fast enough to resolve chemical dynamics, transport, and mixing processes inside a volcanic plume on its intrinsic time scales. In particular, this means it should be faster (in the order of Hz) than the Imaging DOAS approach and have higher selectivity than SO₂ cameras to be applicable to other gases (e.g., BrO).

The foundation of the new concept is to employ a Fabry-Perot Interferometer (FPI) that exhibits transmission features matching the periodicity of the differential absorption structures of the investigated trace gas. By tuning (spectral shifting) the FPI transmission spectrum, it is possible to adjust the spectrum so that it is either correlating or anti-correlating with molecular absorption features, and thereby identifying and quantifying a particular gas. Therefore, the FPI can be implemented in full-frame imaging setups reaching high spatio-temporal resolution accompanied by high trace gas selectivity.

In this thesis, the feasibility of the new technique called Fabry-Perot Interferometer

Correlation Spectroscopy (FPI CS) on the trace gas species SO₂, BrO, and formaldehyde (HCHO) is examined. Recently, Kuhn et al. (2019) demonstrated the FPI CS concept by measuring volcanic SO₂ with a one-pixel FPI prototype. In Chapter 3, model calculations are used to obtain the required sensitivity for an instrument applied under volcanic measurement conditions. In Chapter 4, the physical properties of the employed FPIs are characterised and specified. In the following part, Chapter 5, first characterisation measurements of HCHO in the laboratory with a prototype of a one-pixel FPI instrument are described. The measurements constitute a proof of concept of the FPI CS technique for HCHO and are in good agreement with the modelled data. The last part, Chapter 6, covers the design, construction, and characterisation of an imaging FPI CS prototype (FPI camera). It is applied in first field measurements of SO₂ at Mt. Etna, Sicily, yielding a high spatio-temporal resolution sufficient to estimate SO₂ emission rates. The FPI camera shows a detection limit comparable with present SO₂ cameras but exhibits a higher trace gas selectivity due to reduced cross sensitivities to other trace gases and for aerosols. The imaging FPI CS technique can now be applied to other trace gases, like e.g. volcanic BrO or atmospheric HCHO.

2 Theoretical Background

In this chapter, the theoretical background required for this thesis will be introduced. A particular focus will be on the conceptual theory behind a Fabry-Perot Interferometer (FPI) and its utilisation in atmospheric science.

The first part will treat the most important interactions between electromagnetic waves with matter, in our case, solar radiation, and Earth's atmosphere, respectively. In the following section, the principles of absorption spectroscopy in the ultraviolet and visible (UV-Vis) wavelength range are explained. The third part deals with imaging techniques in atmospheric remote sensing, highlighting trace gas imaging of volcanic plumes. In the last section of this chapter, both the general theory and fundamental characteristics of an FPI are outlined. Further, its possible applications in atmospheric remote sensing will be demonstrated.

2.1 UV-Vis radiation in Earth's atmosphere

The propagation of electromagnetic waves in an absorbing and scattering medium like Earth's atmosphere leads to a variety of interactions. The kind of interaction underlies classical electrodynamic properties and depends on both the size, shape and composition of the scattering particle and whether energy is transferred to the particle or not. With these preconditions, a coarse classification of interactions can be made into elastic scattering, inelastic scattering, and absorption. Each interaction removes photons from the incoming electromagnetic radiation and therefore causes extinction.

In Figure 2.1, the extinction features of the atmosphere can be seen by comparing the spectral solar top of atmosphere radiation with radiation at sea level surface.

2.1.1 Elastic scattering

Elastic scattering is an interaction between light and particles that conserves its energy (frequency), while the direction of the electromagnetic wave is changed. Depending on the characteristic dimension r of the particle relative to the wavelength λ , which is expressed by the size parameter $x = \frac{2\pi r}{\lambda}$, one can distinguish between Mie and Rayleigh Scattering.

Rayleigh scattering is dominating, if the particles are much smaller than the wavelength ($x \ll 1$), which in the UV-Vis wavelength range holds for air molecules and small aerosol particles. The oscillating field of the incident light induces a magnetic dipole in the particle that, analogous to a Hertzian Dipole, re-emits the incoming radiation. The probability of radiation to be scattered in the direction ϑ relative to

2 Theoretical Background

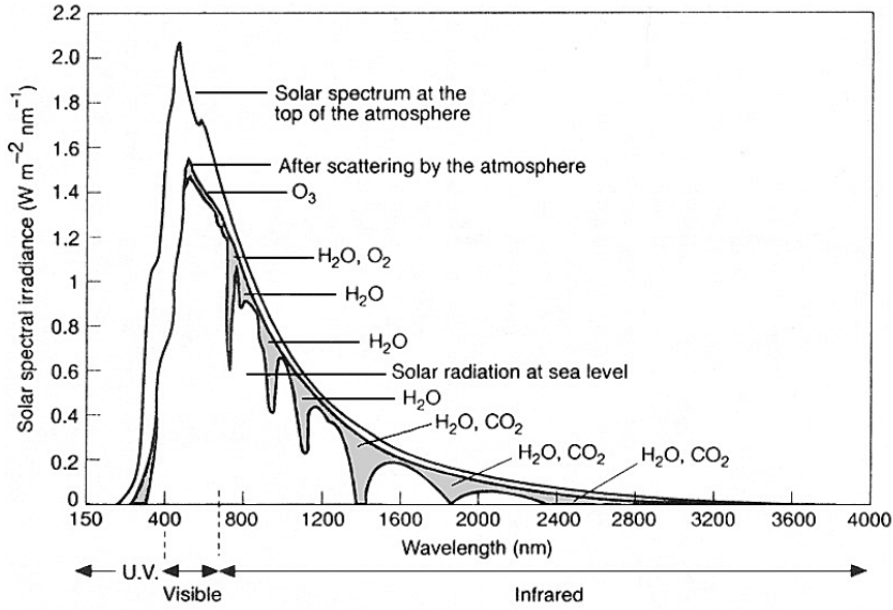


Figure 2.1: The spectral distribution of solar radiation at the top of the atmosphere and sea level. Light propagating through Earth's atmosphere is attenuated by both scattering and absorption. Exemplarily, some absorbing molecules and their impact on the incoming radiation (shaded area) are shown. Taken from Dickey and Falkowski (2002).

the incident light is given by the Rayleigh phase function $\Theta(\vartheta) = \frac{3}{4}(1 + \cos^2(\vartheta))$, which is symmetric in ϑ and exhibits a strong preference in forward and backward scattering direction. The simplified Rayleigh scattering cross section $\sigma_R(\lambda)$ can be approximated by $\sigma_R(\lambda) \approx \sigma_{R0} \cdot \lambda^{-4}$, with $\sigma_{R0} \approx 4.4 \cdot 10^{-16} \text{cm}^2 \text{nm}^4 \text{molec}^{-1}$ (Platt and Stutz, 2008).

In Earth's atmosphere, the particle size varies over several orders of magnitude, like cloud droplets, volcanic ash, or dust particles. Therefore the size parameter can reach unity or even higher values. In this regime, the wavelength of incident radiation and the dimension of particles are comparable. Hence, the incoming radiation can cause a coherent excitation of the elementary dipoles within the aerosol particles. These elementary dipoles emit electromagnetic waves simultaneously, which then can interfere with each other. As a consequence, scattering angle dependent maxima and minima occur with a strong dominance in forward scattering direction. The generalization of this process is referred to as **Mie scattering**, and in contrast to Rayleigh scattering, there is a much weaker wavelength dependency typically proportional to $\lambda^{-1.3}$ (Roedel and Wagner, 2017).

2.1.2 Inelastic Scattering

Inelastic scattering events or **Raman scattering** occurs with a fraction of 2-4 % compared to Rayleigh scattering (Roedel and Wagner, 2017) and changes both, direction and energy of incident electromagnetic waves. A discrete amount of energy is passed

to or taken from a molecule that changes its state of rotational or vibrational excitation. The filling-in of narrow structured lines in the Fraunhofer spectra can be traced back to Raman scattering Solomon et al. (1987). This impact is called Ring effect, which was first described by Grainger and Ring (1962), and needs to be considered in measurements of scattered sunlight.

2.1.3 Absorption

If electromagnetic radiation propagates in a medium, like Earth's atmosphere, molecules and aerosols are capable of absorbing radiation. If photon energy is transferred to a molecule, it can cause a transition of the molecule into a higher excited quantum dynamical state. Thereby, the initial radiance will be attenuated. A quantitative description for absorption is given by Bouguer-Lambert-Beer's law

$$dI(\lambda) = -I_0(\lambda) \cdot \sigma(\lambda) \cdot c(l) dl \quad (2.1)$$

in differential form, where $I_0(\lambda)$ is the initial emitted radiance, while $dI(\lambda)$ is the observed radiance after traversing a medium of infinitesimal thickness dl and particle concentration $c(l)$. The quantity $\sigma(\lambda)$ denotes the absorption cross section and is an absorber specific quantity that contains the spectral characteristic absorption features of the present absorbing species. The integration over a light path length of L yields

$$-\ln \left(\frac{I(\lambda)}{I_0(\lambda)} \right) = \sigma(\lambda) \int_0^L c(l) dl = \sigma(\lambda) \cdot S = \tau(\lambda) \quad (2.2)$$

which corresponds to the optical density $\tau(\lambda)$. In this equation, S , the column density, can be identified as the integrated amount of absorbing particles along a light path. Rearranging and generalising the equation for a medium with i absorbing species a summation of the different optical densities has to be included

$$I(\lambda) = I_0(\lambda) \cdot \exp \left(- \sum_i \sigma_i(\lambda) S_i \right) = I_0(\lambda) \cdot \exp \left(- \sum_i \tau_i(\lambda) \right) \quad (2.3)$$

2.1.4 Radiative transfer

By observing scattered sunlight, the radiation can undergo all of the before stated processes several times on its way through the atmosphere. Assuming a detector with specific viewing direction and a certain field of view: The Incident radiation on its way to the detector can be absorbed or scattered out of the viewing direction leading to attenuation. Further, the preliminary scattered radiation or radiation emitted from a different source into an arbitrary direction can be scattered into the detector's field of view. This will cause an enhancement of the observed radiance. The radiative transfer equation combines all the contributions and therefore represents the fundamental equation of measurement techniques using scattered sunlight. Thermal emissions do

2 Theoretical Background

not need to be accounted for in the UV-Vis wavelength regime. The spectral change of radiance within an infinitesimal path length ds is given by:

$$\frac{dI(\lambda)}{ds} = -(\tau_a + \tau_s) \cdot I(\lambda) + \tau_s \int_S I'(\lambda, \Omega) \Theta(\Omega) d\Omega \quad (2.4)$$

Where the first term represents Bouguer-Lambert-Beer's law with the addition of scattering extinction $\tau_s = \tau_R + \tau_M$ by Rayleigh and Mie scattering. The second term accounts for the increase of radiance by photons scattered into the viewing direction, where $I'(\lambda, \Omega)$ is the intensity and $\Theta(\Omega)$ the phase function at scattering location.

2.2 Absorption Spectroscopy

In Section 2.1.3, the fundamental principle of absorption, according to Bouguer-Lambert-Beer's law, was introduced. Absorption spectroscopy exploits that the molecular structure of different molecule species generates characteristic quantum mechanical energy levels corresponding to electronic, rotational, and vibrational states. The molecule can absorb photons that carry the energy difference between two of these levels. If none of the quantum mechanical selection rules is violated, a molecular transition into a higher excited state will be induced. This results in unique spectral absorption characteristics for each molecule species and is denoted as the absorption cross section $\sigma(\lambda)$. This quantity allows distinguishing a multitude of absorbing species by spectroscopic measurements. An exemplary selection of $\sigma(\lambda)$ for different atmospheric molecular species in the UV-Vis wavelength range can be seen in Figure 2.2.

2.2.1 Differential optical absorption spectroscopy

Differential optical absorption spectroscopy (DOAS) is a well-established measurement technique to determine the presence and concentration of atmospheric trace gases in the UV-Vis wavelength range simultaneously. In this chapter, a brief introduction into the DOAS measurement technique and the underlying principles is given according to Platt and Stutz (2008).

As introduced in Section 2.1, light that travels through the atmosphere, undergoes absorption, and scattering processes that reduce the initial intensity. Likewise, the DOAS instrument that has transmissivity smaller than one will attenuate the intensity due to imperfect optical elements. Considering these factors an extension of Bouguer-Lambert-Beer's law (Equation 2.3) can be applied resulting in

$$I(\lambda) = I_0(\lambda) \cdot \exp \left(- \sum_i \sigma_i(\lambda) S_i + \varepsilon_R(\lambda) + \varepsilon_M(\lambda) \right) \cdot A(\lambda) \quad (2.5)$$

where $\varepsilon_R(\lambda)$ and $\varepsilon_M(\lambda)$ are Rayleigh and Mie extinction respectively and $A(\lambda)$ represents the instrumental attenuation factor. The need for $A(\lambda)$ arises from the fact

2.2 Absorption Spectroscopy

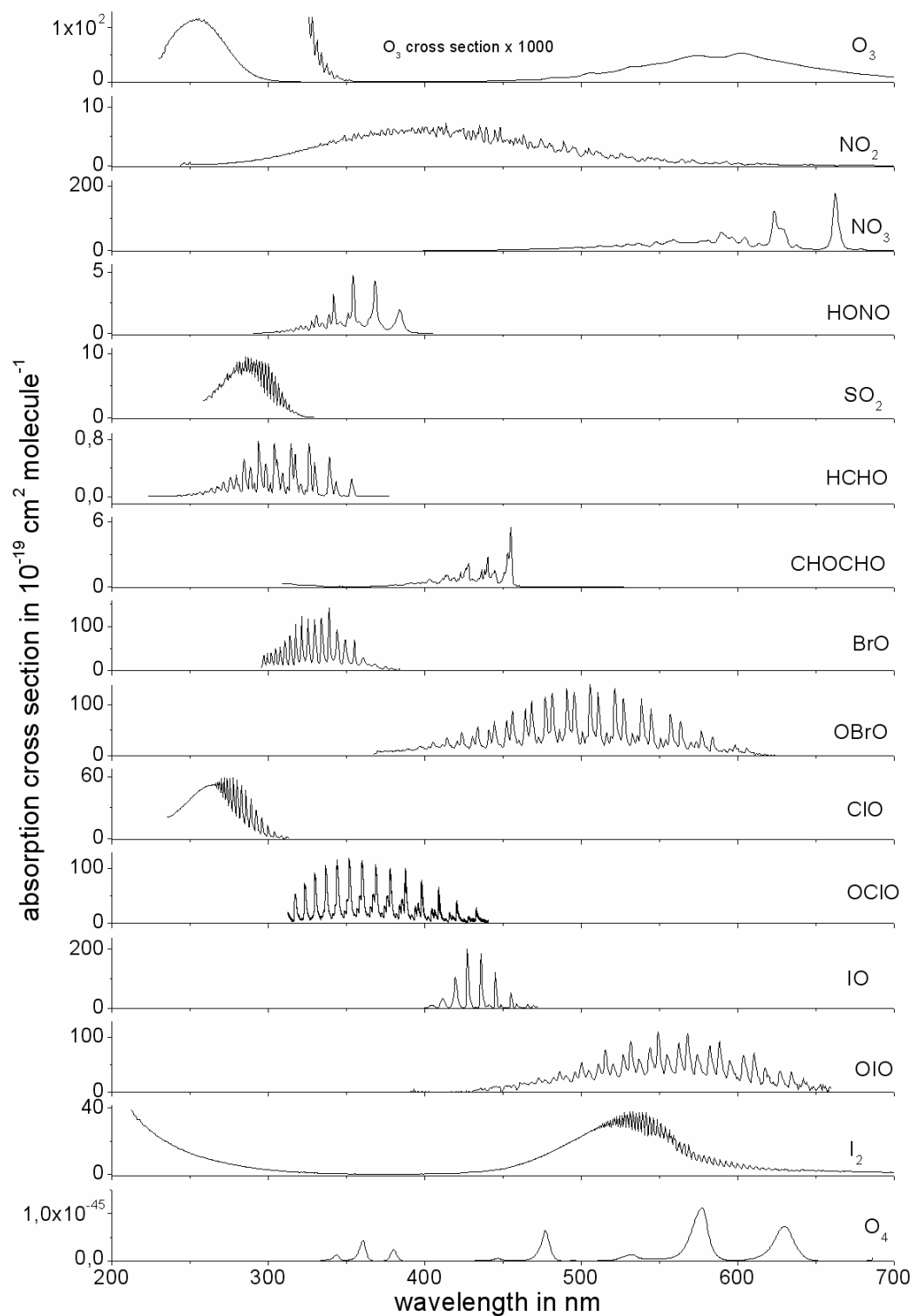


Figure 2.2: Absorption cross sections and their strength are displayed as a function of wavelength. Taken from Platt and Stutz (2008).

2 Theoretical Background

that scattered light is measured and the scattering properties for both spectra ($I(\lambda)$ and $I_0(\lambda)$) are usually different. To determine gas specific column densities S_i , like in Equation 2.3, all influencing factors of equation 2.5 have to be quantified, which is not always achievable under atmospheric measurements conditions. To overcome this problem, the broadband and differential (narrowband) spectral features of the absorption spectrum can be used. The absorption of many trace gases and extinction due to scattering show broad spectral characteristics. However, most trace gases further exhibit high frequency absorption structures superimposed with the broad band absorption (e.g. SO_2 , see Figure 2.3). The fundamental principle of the DOAS technique is now to separate the spectral absorption into broadband and narrowband structured parts to identify the narrowband trace gas absorption features (Platt and Stutz, 2008). This separation can be applied to the absorption cross section $\sigma_i(\lambda)$ by

$$\sigma_i(\lambda) = \sigma_{i,b}(\lambda) + \sigma_{i,n}(\lambda) \quad (2.6)$$

where $\sigma_{i,b}(\lambda)$ contains all broadband features and $\sigma_{i,n}(\lambda)$ constitutes the gas specific narrowband absorption cross section. The principle is shown in Figure 2.3 where the separation of the SO_2 absorption cross section into $\sigma_{i,b}(\lambda)$ and $\sigma_{i,n}(\lambda)$ is shown. By inserting the separated cross section of equation 2.6 into equation 2.5 it is possible to perform a separation of the intensity into a broadband and narrowband part on the same manner

$$I(\lambda) = I_0(\lambda) \cdot \exp\left(-\sum_i \sigma_{i,b}(\lambda) S_i + \varepsilon_R(\lambda) + \varepsilon_M(\lambda)\right) \cdot A(\lambda) \cdot \exp\left(-\sum_i \sigma_{i,n}(\lambda) S_i\right). \quad (2.7)$$

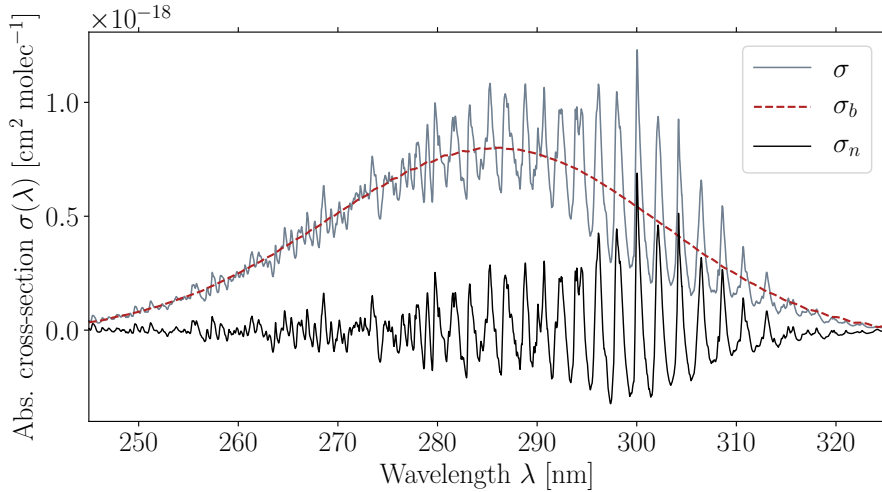


Figure 2.3: The DOAS principle illustrated by the separation of the total SO_2 absorption cross section σ into the broadband cross section σ_b and narrowband cross section σ_n . SO_2 cross section adapted from Vandaele et al. (2009).

Thereby the first three factors contain the broadband and the last factor the narrow-band information only. Thus, it is possible to define a new quantity $I'_0(\lambda)$,

$$I'_0(\lambda) = I_0(\lambda) \cdot \exp \left(- \sum_i \sigma_{i,b}(\lambda) S_i + \varepsilon_R(\lambda) + \varepsilon_M(\lambda) \right) \cdot A(\lambda) \quad (2.8)$$

which represents the intensity with broadband absorption only. Analogous to Equation 2.2 we can now define the differential optical density $\tau'(\lambda)$ as

$$\tau_n(\lambda) = -\ln \left(\frac{I(\lambda)}{I'_0(\lambda)} \right) = -\sum_i \sigma_{i,n}(\lambda) S_i. \quad (2.9)$$

The separation into broadband and narrowband parts is only possible under the pre-conditions that measured intensities exhibit sufficient high spectral information to identify the differential structures of numerous gas species simultaneously. By fitting the literature narrowband cross sections $\sigma_{i,n}$ to the detected differential optical densities $\tau_{i,n}$ the column densities S_i can be retrieved numerically as a fit coefficient. The DOAS technique, therefore, features high sensitivity and specificity for a coincident measurement of a multitude of atmospheric gas species without the requirement of an absolute calibration.

2.2.2 Impacts of DOAS instruments on the recorded intensity spectrum

The theory explained in the above section is an idealised approach and neglects the impacts of realistic measurement devices. The term „passive“ DOAS is commonly applied when natural light sources (e.g. sun) are used for measurements. A spectrum is in general recorded by grating spectrometers where the incoming spectral intensity $I(\lambda)$ is focused on the entrance slit of a spectrograph. The intensity spectrum is dispersed by a grating or prism and is then recorded by a multi-pixel CCD detector. As the optical and spectral resolution is finite, the initial spectrum is altered. The impacts on recorded spectra can mathematically be described by a convolution with the instrument line function $H(\lambda)$, giving the recorded spectra $I^*(\lambda)$

$$I^*(\lambda) = I(\lambda) \star H(\lambda) = \int I(\lambda - \lambda') H(\lambda') d\lambda'. \quad (2.10)$$

As the recording detector exhibits a finite and discrete amount of pixels i a wavelength-interval λ_i to λ_{i+1} of $I^*(\lambda)$ is mapped onto a pixel. Therefore, the discretised signal $I^*(i)$ is given by:

$$I^*(i) = \int_{\lambda_i}^{\lambda_{i+1}} I^*(\lambda) d\lambda \quad (2.11)$$

This mapping is dependent on temperature changes. Hence, variations in the detector temperature can cause a relative shift and squeeze between captured spectra.

2.3 Imaging of atmospheric trace gases

Imaging measurements allow for spatial mapping of atmospheric trace gas concentrations. Depending on the temporal resolution different atmospheric processes of interest can be studied, including large scale atmospheric transport (e.g., Warnach et al., 2018; Carn et al., 2016), turbulence processes (e.g. Dinger et al., 2018), chemical dynamics (e.g. Louban et al., 2009) and high resolution emission rates from point sources (e.g. Kern et al., 2015).

An image can be recorded by a two-dimensional detector (i.e., CCD or CMOS arrays) consisting of discrete pixels. Optical elements are used to produce a clear picture and defining the image field of view (FOV). Depending on the measurement technique, a coarse classification into dispersive and non-dispersive instruments can be done. Dispersive methods determine the complete spectral information for each spatial pixel using gratings or prisms (e.g., imaging DOAS). As one detector dimension is used for spectral information, spatial scanning of the FOV is required. Non-dispersive techniques (e.g. SO₂ camera), in contrast, can record full-frame images but are constrained to a few spectral channels defined by wavelength selecting elements (WSE) (Platt et al., 2015).

2.3.1 Imaging DOAS

The imaging DOAS (IDOAS) technique is a dispersive measurement method using the principles explained in Section 2.2.1. The gas column densities are retrieved from three-dimensional data sets consisting of two spatial and one spectral dimension. As three dimensions have to be mapped on a usually one or two-dimensional detector array, scanning is required, which can be performed in two ways. By applying whiskbroom scanning, the spectral data are recorded by a one-dimensional detector array consecutively for all distinct pixels of the FOV. In the second approach based on pushbroom, the FOV is either scanned line or column-wise, where the spectral and spatial information are recorded by a two-dimensional detector array (Lohberger et al., 2004).

The major advantage of this technique is that the full spectral information is contained in each pixel. This allows to retrieve the column densities of several trace gases simultaneously, and thus, chemical dynamics within the image can be studied (e.g., Bobrowski et al., 2006; Louban et al., 2009). However, depending on the spatial resolution and the concentration of the studied trace gas, the temporal resolution is low in comparison to other techniques as scanning is required. It can lie in the regime of minutes (Platt et al., 2015). Lately, Manago et al. (2018) carried out NO₂ measurements applying a hyperspectral camera based on the imaging DOAS technique with a considerably temporal resolution of around ≈ 0.08 Hz. A further application of the IDOAS technique are satellite-based measurements. It facilitates the possibility to monitor trace gases column densities and their transport processes on a global scale. Besides the detection of volcanic emissions (e.g., Warnach et al., 2018; Khokhar et al., 2005) it is possible to monitor sources of atmospheric pollution

(e.g. cities) as they appear like point sources from satellite-based measurements (e.g., Leue et al., 2001; Griffin et al., 2019). However, the temporal resolution is restricted to the satellite overpass time and is therefore usually in the order of days and the spatial resolution is coarse in comparison with ground based techniques.

2.3.2 The SO₂ camera

The SO₂ camera is a non-dispersive optical remote sensing technique mostly used to measure SO₂ emission rates of point sources like volcanoes (e.g., Mori and Burton, 2006; Bluth et al., 2007). The instruments record full-frame images using UV sensitive two-dimensional detectors to get spatial information, whereas the spectral data is obtained from interference filters. A bandpass filter is used to analyse the characteristic SO₂ absorption in scattered solar light in the UV range between 300 and 320 nm. The central wavelength of the filter lies around 310 nm (usually referred to as filter A, transmittance $T_A(\lambda)$) as there is sufficient scattered solar light available while the SO₂ absorption is still strong, see Figure 2.4.

By recording the integrated intensity over the wavelength channel $T_A(\lambda)$ it is possible to retrieve SO₂ column densities (S_{SO_2}) pixel-wise, analogous as shown in Equation 2.2 by calculating the optical density τ_A ,

$$\tau_A = -\ln \frac{I_A}{I_{A,0}} = -\ln \frac{\int I(\lambda) T_A(\lambda) d\lambda}{\int I_0(\lambda) T_A(\lambda) d\lambda} \propto S_{\text{SO}_2} \quad (2.12)$$

where $I_{A,0}(\lambda)$ is the incident radiance and $I_A(\lambda)$ the radiance of light after propagating through a SO₂ containing volcanic plume. $I_{A,0}(\lambda)$ can be obtained by changing the camera viewing direction onto a FOV that is not containing SO₂. Another method

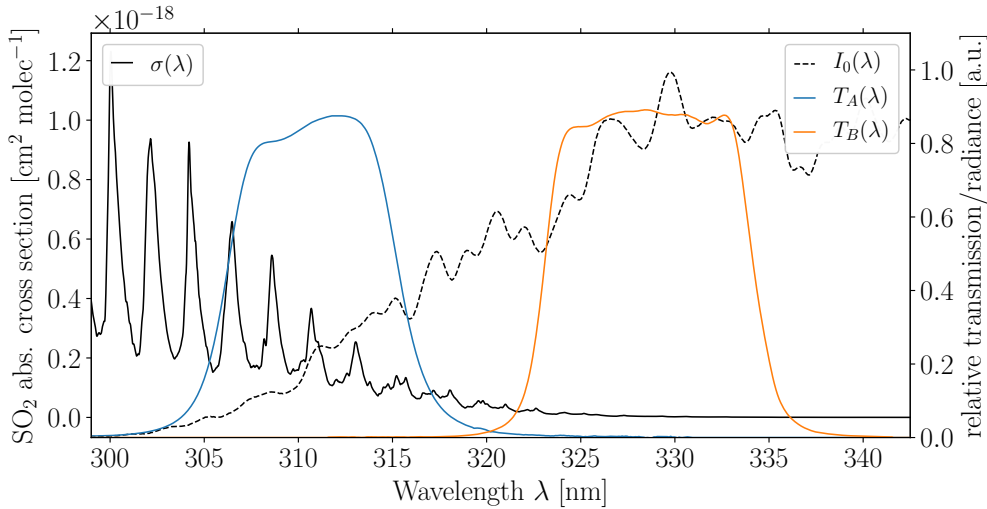


Figure 2.4: The SO₂ absorption cross section $\sigma(\lambda)$ (adapted from Vandaele et al. (2009)), relative scattered sunlight intensity $I_0(\lambda)$ and transmittance of filter A $T_A(\lambda)$ and filter B $T_B(\lambda)$.

2 Theoretical Background

is to extrapolate $I_0(\lambda)$ from the pixels within an image, not containing the plume. The optical density τ_A is, however, not only sensitive to fluctuations of volcanic S_{SO_2} but to variations in the radiative transfer within a volcanic plume. These can be induced by ash, aerosols or condensation causing additional extinction. A first order correction to those impacts is achieved by using a second filter with a slightly higher central wavelength around 330 nm (usually referred to as filter B, transmittance $T_B(\lambda)$). In this spectral region, the SO_2 absorption is much smaller in comparison to filter A, see Figure 2.4. Therefore, the spectral channel of filter B is only weakly influenced by the absorption of SO_2 . As the aerosol extinction effects show broadband characteristics, they are relatively constant over this 20 nm spectral separation. Applying the correction to the optical density τ_A the instrument response, referred to as apparent absorbance AA can be defined as:

$$AA = \tau_A - \tau_B = -\ln \frac{I_A \cdot I_{B,0}}{I_{A,0} \cdot I_B} = (\bar{\sigma}_{A,\text{SO}_2} - \bar{\sigma}_{B,\text{SO}_2}) \cdot S_{\text{SO}_2} = k_{\text{SO}_2} \cdot S \quad (2.13)$$

with the weighted SO_2 absorption cross section $\bar{\sigma}_{i,\text{SO}_2}$, averaged over the respective wavelength range $i = A, B$ and k_{SO_2} the weighted mean SO_2 absorption cross section. The quantity k_{SO_2} , is the effective SO_2 absorption seen by the camera and can thereby be interpreted as the instrument's sensitivity.

Since the recorded AA is proportional to S_{SO_2} a simple absolute calibration for SO_2 cameras is possible. One method of calibration is to use a set of gas cells filled with SO_2 that are placed in front of the camera, covering the FOV (e.g., Kantzas et al., 2010). Since the concentration inside the cells is known a calibration curve between the AA and S_{SO_2} can be derived, yielding the sensitivity k_{SO_2} . Another approach is to employ a co-aligned DOAS instrument, which obtains S_{SO_2} in a small region of the FOV. By variations of the SO_2 concentration inside the plume and if the position of the DOAS FOV inside the SO_2 camera FOV is known, the sensitivity k_{SO_2} between the instrument AA and DOAS S_{SO_2} can be retrieved (e.g., Lübcke et al., 2013).

One of the major advantages of SO_2 cameras in comparison to dispersive imaging techniques is that the frame rate is in the order of one Hertz. This allows quantifying emission rates by acquiring a temporally high resolved series of SO_2 gas distribution (e.g., Kern et al., 2015). The image series furthermore allows to determine the plume speed and propagation direction (e.g., Klein et al., 2017) and to study turbulences in the atmosphere as shown by Dinger et al. (2018).

One of the drawbacks is the lack of spectral information. This has the consequence that the selectivity and sensitivity of a camera is mostly restricted to a single gas, and only gas species exhibiting appropriate strong absorption features (i.e. SO_2) can be detected (Platt et al., 2015). Besides this, the background reference images $I_{A,0}$ and $I_{B,0}$ should represent the sky conditions behind the volcanic plume. Since these images are required to be SO_2 free the camera's viewing direction has to be changed, yielding a change in the sky illumination as it depends on the relative solar azimuth and zenith angle. Additionally, the stratospheric ozone shows cross sensitivities because σ_{O_3} exhibits structures similar to σ_{SO_2} (Kuhn et al., 2014). The illumination aspects further restrict the application of SO_2 cameras to weather conditions with ad-

equate homogenous sky illuminations. Moreover, the consideration made of aerosols extinction to be constant over a wavelength range of 20 nm does not always hold. Interferences can occur if the aerosol optical density (AOD) changes considerably within the spectral separation of the two filters. Especially if the volcanic plume shows high AODs (condensation), the radiative transfer changes and multiple scattering events will affect the light path within the absorbing plume resulting in a biased SO₂ signal (Kuhn et al., 2014).

2.4 Fabry-Perot Interferometer Correlation Spectroscopy

The wavelength selective elements (WSE) are the reason of the major drawbacks of the SO₂ camera described in the preceding section, in particular, the large gap of ≈ 20 nm between the two spectral channels. Exchanging the filters by a better suitable WSE, like a Fabry-Perot Interferometer (FPI), should improve the measurements.

The FPI is a non-dispersive WSE based on the principle of an optical resonator. It is composed of two plane-parallel reflecting surfaces, using the concept of multiple-beam interference. This section covers the basic theory underlying an FPI, a more comprehensive description can be found in e.g. Perot and Fabry (1899) or Demtröder (2013). Further, its application to trace gas remote sensing will be explained.

2.4.1 The Fabry-perot Interferometer

The separation of electromagnetic radiation into a reflected and refracted (transmitted) part at the interface of two optical media with different refractive indices n is described by the Fresnel equations. In addition, absorption within the media can occur. The three quantities reflectivity R transmissivity T and absorptivity A have to fulfil energy conservation and therefore to meet the criterion $R + T + A = 1$. As all optical materials used in this thesis are near-complete translucent, absorptivity will be neglected in the following, resulting in $R + T \approx 1$. Reflectivity and transmissivity are functions of the difference between the refractive indices of the two media and the incident angle of incoming radiation. The radiances of the reflected and transmitted beams I_R and I_T are dependent on the incident radiance I_0 and are given by

$$I_R = R \cdot I_0 \quad (2.14)$$

$$I_T = T \cdot I_0 = (1 - R) \cdot I_0 \quad (2.15)$$

Since the FPI consists of two plane parallel surfaces with reflectivity R and spatial separation d filled by a medium with refractive index n (see Figure 2.5), the transmission and reflection functions of the entire setup are more complex. As electromagnetic radiation traverses the first interface, multiple reflections arise between the two surfaces causing interference (see Figure 2.5). If transmitted light beams have a phase

2 Theoretical Background

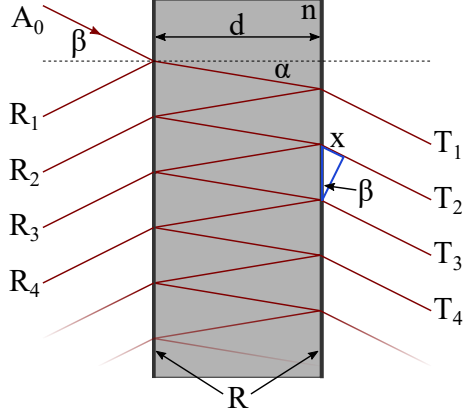


Figure 2.5: Schematic of an FPI. Incoming beam A_0 gets reflected between the two plane-parallel surfaces of the FPI, causing multiple-beam interference. The interference is generating the characteristic FPI transmission and reflection spectra, which are dependent on the plate separation d , the refractive index n , the incident angle α , and the surface reflectivity R .

difference of $\Delta\varphi = 2m \cdot \pi$ with $m \in \mathbb{N}$, constructive interference occurs corresponding to high transmission. If the beams are out-of-phase, showing a phase difference of $\Delta\varphi = (2m + 1) \cdot \pi$, destructive interference will induce a minimum in transmission, vice versa for reflection. A quantitative description for the reflected and transmitted beams can be given considering the propagation of a single beam of light with amplitude $|A_0| \propto \sqrt{I_0}$, incident under the angle β onto the first surface. Each time the initial beam is hitting one of the surfaces the beam will split. This results in groups of transmitted and reflected partial beams with amplitudes $|T_i|$ and $|R_i|$ respectively, given by:

$$\begin{aligned}
 |R_1| &= \sqrt{1-R} \cdot |A_0| & |T_1| &= (1-R) \cdot |A_0| \\
 |R_2| &= R^{1/2} \cdot (1-R) \cdot |A_0| & |T_2| &= R \cdot (1-R) \cdot |A_0| \\
 |R_3| &= R^{3/2} \cdot (1-R) \cdot |A_0| & |T_3| &= R^2 \cdot (1-R) \cdot |A_0| \\
 |R_4| &= R^{5/2} \cdot (1-R) \cdot |A_0| & |T_4| &= R^3 \cdot (1-R) \cdot |A_0| \\
 \Rightarrow |R_{i+1}| &= R \cdot |R_i| \quad \forall i \geq 2 \in \mathbb{N} & \Rightarrow |T_{i+1}| &= R \cdot |T_i| \quad \forall i \geq 1 \in \mathbb{N}
 \end{aligned}$$

Two of the successively transmitted partial beams e.g. $|T_{i+1}|$ and $|T_i|$ therefore feature an optical path length difference Δs of

$$\Delta s = \frac{2nd}{\cos \alpha} - x = 2nd \cos \alpha \quad (2.16)$$

which can be derived from geometric considerations (see Figure 2.5). The optical path length difference Δs is leading to a phase shift $\Delta\varphi$ between the two beams of

$$\Delta\varphi = \frac{2\pi\Delta s}{\lambda} + \phi \quad (2.17)$$

where ϕ accounts for the phase jumps upon transmission or reflection. The phase jump can be either $\phi = 0$ or $\phi = \pi$, depending on whether the reflection occurs on a surface with a higher or a lower refractive index and if the transversal or longitudinal part of the electromagnetic radiation is considered. In the case of an FPI, all transmitted beams are reflected on a surface by either zero times (T_1 see Figure 2.5) or in

a even number (T_2, T_3, \dots see Figure 2.5). As the phase jump for transmitted beams thereby is always either 0 or 2π it can be neglected. In case of the reflected radiation the first beam $|R_1|$ will show a different phase jump with respect to all other beams $|R_i| \forall i \geq 2 \in \mathbb{N}$.

A general expression for the total reflected and transmitted intensities, R_{FPI} and T_{FPI} respectively, of an FPI can be derived by a summation over the squared reflected and transmitted partial beams yielding the Airy formulas

$$R_{FPI} = \frac{I_R}{I_0} = \frac{\tilde{F} \cdot \sin^2(\Delta\varphi/2)}{1 + \tilde{F} \cdot \sin^2(\Delta\varphi/2)} \quad (2.18a)$$

$$T_{FPI} = \frac{I_T}{I_0} = \frac{1}{1 + \tilde{F} \cdot \sin^2(\Delta\varphi/2)} \quad (2.18b)$$

with the finesse coefficient \tilde{F}

$$\tilde{F} = \frac{4R}{(1-R)^2}. \quad (2.19)$$

The Airy formulas fulfil the law of energy conservation ($R_{FPI} + T_{FPI} = 1$) and describe the structure of the FPI transmission and reflection as a function of the optical path difference $\Delta\varphi$. In this thesis, only the transmitted radiation will be relevant, therefore hereafter, by talking about the FPI spectrum, I refer to the transmission function 2.18b only. In Figure 2.6 the characteristic comb-shaped spectrum T_{FPI} is shown as a function of $\Delta\varphi$. It shows periodic maxima $\lambda_m (I_T = I_0)$ for every

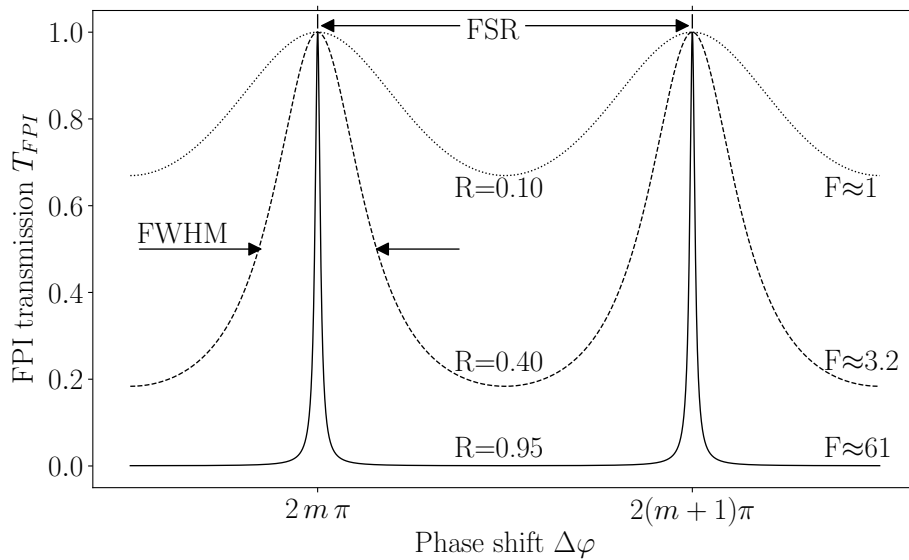


Figure 2.6: The FPI transmittance spectrum T_{FPI} as a function of the phase shift $\Delta\varphi$ shown for different reflectivity R resulting in different finesse F . The transmission peaks are characterised by the free spectral range (FSR) $\Delta\lambda$ between two peaks and the full width half maximum (FWHM) $\delta\lambda$.

2 Theoretical Background

$\Delta\varphi = 2\pi \cdot m$ at high orders of $m \in \mathbb{N}$. The maxima positions are given by

$$\lambda_m = \frac{\Delta s}{m} = \frac{2nd}{m} \cos \alpha. \quad (2.20)$$

In other words, the FPI is a WSE or acts as a spectral filter that only transmits wavelength according to Equation 2.20. Due to the proportionality $\Delta\varphi \propto \frac{1}{\lambda}$ (see Equation 2.17), the obtained maxima can only be assumed to be equidistant in wavelength for high orders of m . As shown in Figure 2.6 two quantities can be used to characterise the FPI spectrum, the free spectral range (FSR) $\Delta\lambda$ and the full width half maximum (FWHM) ε . The former gives the separation of two peaks in the transmittance spectrum. The FSR is always equal to 2π in units of phase shift. In units of wavelength it is the difference between two transmission peaks e.g. λ_m and λ_{m+1} given by

$$\Delta\lambda = \lambda_m - \lambda_{m+1} = \frac{\Delta s}{m} - \frac{\Delta s}{m+1} = \frac{\Delta s}{m(m+1)} = \lambda_m \lambda_{m+1} \frac{1}{\Delta s} \approx \frac{\lambda_m^2}{\Delta s}, \quad (2.21)$$

where the last approximation holds for $m \gg 1$. The FWHM ε of a maxima is determined by the position where the transmission function is $T_{FPI} = 1/2$, given by

$$\varepsilon = 4 \arcsin \left(\frac{1}{\sqrt{F}} \right) = 4 \arcsin \left(\frac{1-R}{2\sqrt{R}} \right) \approx \frac{2(1-R)}{\sqrt{R}} \quad (2.22)$$

where the last approximation is valid for $R > 0.5$. In units of wavelength the FWHM reads $\delta\lambda = \frac{\varepsilon \lambda_m^2}{2\pi \Delta s} \cdot 1$. Now it is possible to define the finesse F , that is the ratio between the FSR and FWHM

$$F = \frac{\Delta\lambda}{\delta\lambda} = \frac{\lambda_m^2 \varepsilon}{2\pi \Delta s^2} = \frac{2\pi}{\varepsilon} \approx \frac{\pi\sqrt{R}}{1-R} \quad (2.23)$$

The finesse is a measure for the number of interfering beams and a function of reflectivity R . Therefore, for higher values of F the interference is more pronounced resulting in sharper transmission peaks.

2.4.2 Trace gas detection by FPI Correlation Spectroscopy

The FPI correlation spectroscopy (FPI CS) is a novel remote sensing technique based on a working principle similar to the SO₂ camera described in Section 2.3.2. The FPI is used as WSE replacing the two filters applied in SO₂ cameras. The comb-shaped spectrum T_{FPI} of Equation 2.18b is a function of the parameters $\{d, n, \alpha, R\}$. Altering one of these parameters will change T_{FPI} accordingly, inducing both a shift and a change of the FSR (stretch) to the spectrum. However, if the FPI is deployed in the regime of high orders in m , the stretch will be small and can be neglected. Changing

$${}^1\varepsilon = \frac{2\pi\Delta s}{\lambda_m} - \frac{2\pi\Delta s}{\lambda_m + \delta\lambda} = 2\pi\Delta s \frac{\delta\lambda}{\lambda_m(\lambda_m + \delta\lambda)} \approx 2\pi\Delta s \frac{\delta\lambda}{\lambda_m^2}, \text{ for } m \gg 1 \Rightarrow \delta\lambda = \frac{\varepsilon \lambda_m^2}{2\pi\Delta s}$$

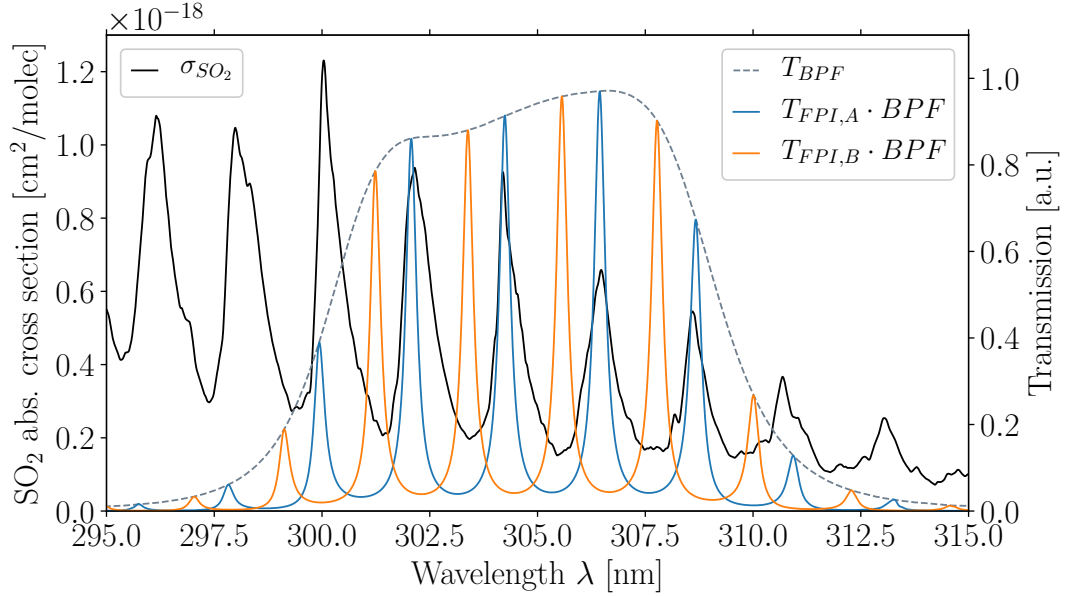


Figure 2.7: The periodic FPI transmission maxima in setting A ($T_{FPI,A}$; on-band) and setting B ($T_{FPI,B}$; off-band) over wavelength is matched to the narrowband absorption structures of SO_2 (σ_{SO_2} ; adapted from Vandaele et al. (2009)). The spectral range is selected by a band pass filter (T_{BPF} , dashed grey).

parameters will thereby result in essentially a spectral shift of the transmission spectrum only.

The application of an FPI facilitates the exploitation of periodic molecular differential absorption structures originating from vibro-rotational states of the respective molecule. This is accomplished by matching the transmission maxima of T_{FPI} to the narrowband (usually vibrational) structures of molecular absorption. The variation of the FPI's physical parameters allows to tune the transmission spectrum to achieve a setting where the FPI peaks coincide with the molecular absorption structures (on-band; setting A) and anti-correlate (off-band; setting B). An additional band pass filter is used to select the spectral range of the highest correlation to the according to molecular absorption. The principle for SO_2 is shown in Figure 2.7 .

The general detection principle is now analogous to the SO_2 camera principle explained before in Equation 2.13, where the FPI setting A and setting B correspond to filter A and filter B respectively. The apparent absorbance AA_{FPI} therefore is given by

$$AA_{FPI} = \tau_{FPI,A} - \tau_{FPI,B} = k \cdot S \quad (2.24)$$

with optical densities $\tau_{FPI,i}$ acquired by a camera with the FPI in setting $i = A, B$ and k the weighted mean trace gas absorption cross section (instruments' sensitivity). The proportionality factor to the column density can be determined as for the SO_2 camera by performing a gas cell calibration or by the utilisation of a co-aligned DOAS setup. As the spectral shift between the two channels in setting A and B is in the order

2 Theoretical Background

of a few nanometres (in the case of $\text{SO}_2 \approx 1 \text{ nm}$) the broadband cross interferences, e.g. to aerosols and ozone, are drastically reduced in comparison to the SO_2 camera. Furthermore, the SO_2 sensitivity is increased (Kuhn et al., 2014, 2019). Another advantage of the FPI technique is that due to the small spectral shift, the background illumination will change only weakly between setting A and B. And since the ozone and aerosol interference is reduced drastically, there should be no need to acquire background images. This fact further enlarges the applicability to weather conditions with clouds in the FOV. Finally, the high selectivity allows applying the FPI CS technique to other trace gas species than SO_2 , which are relevant in volcanic plumes and other fields of atmospheric research. The FPI transmission peaks are matched as before to (ideally periodic) narrowband absorption structures of other species. Trace gas species with suitable periodic structures present in volcanic plumes are for example bromine monoxide (BrO) and chlorine dioxide (ClO). Imaging their spatial distribution allows to get a better insight into chemical processes inside volcanic plumes. Further, the FPI CS technique can be applied to other atmospheric trace gas species emitted by point sources, like formaldehyde (HCHO) and nitrogen dioxide (NO_2), to study, for example, air pollution.

3 Model study

In order to investigate FPI correlation spectroscopy (FPI CS) and anticipate its performance, model calculations were performed based on the theory described in the preceding section. The FPI CS can be applied in various measurement scenarios (e.g., stack emissions, ship emission, volcanoes, etc.) and for a multitude of atmospheric trace gases. However, this study, concentrates on remote sensing of volcanic plumes, investigating the trace gases SO₂ and BrO. Further, the model calculations are used to examine the theoretical impact of cross sensitivities to other gas species, in particular the cross sensitivity between BrO and HCHO is of importance.

A simplified model, considering only non-divergent (parallel) light beams, is used in this thesis. For a more comprehensive study, see Kuhn (2015); Kuhn et al. (2019).

3.1 The FPI instrument response model

An FPI CS instrument consists of an optics, the band pass filter, the FPI, and a detector (see Figure 5.1). Here, for simplicity, we only consider parallel light incidence (e.g., the light traversing the instrument on the optical axis). The instrument's optical transfer function can be determined by the spectral integral over the product of the FPI transmission function $T_{FPI}(\lambda)$ and the band pass filter transmittance curve $T_{BPF}(\lambda)$. The influences of the instrument's optics and the detector's spectral response to the transfer function are assumed to be constant as only small spectral ranges (≈ 10 nm) are considered. They are set to unity in this study. Further, photon noise will not be considered in this model study. For a more concise treatment I thereby refer to Kuhn (2015) and Kuhn et al. (2019).

In the model $T_{FPI}(\lambda)$ is given by the Airy function (Equation 2.18b) and the finesse coefficient (Equation 2.19)

$$T_{FPI}(\lambda; d, n, \alpha, R) = \left[1 + \frac{4R}{(1-R)^2} \sin^2 \left(\frac{2\pi d n \cos \alpha}{\lambda} \right) \right]^{-1} \quad (3.1)$$

The reflectivity R and refractive index n are in general functions of λ . As before, this variation is neglected since only narrow spectral ranges are studied. The FPIs used in this thesis consist of two static plane-parallel fused silica plates mounted at a distance d as shown in Figure 4.2. The gap between the plates is filled with air setting $\{d, n, R\} = const$. The, variables of the FPI transmission function are hence reduced to the wavelength (λ) and incident angle (α) dependencies yielding $T_{FPI} = T_{FPI}(\lambda; \alpha)$.

A band pass filter is used to pre-select the spectral range exhibiting the highest correlation between the considered trace gas absorption cross section $\sigma(\lambda)$ and $T_{FPI}(\lambda; \alpha)$.

3 Model study

The theoretical spectral transmission profiles $T_{BPF}(\lambda)$ of filters available on the market were used. Those yielding best correlations were purchased and the real band pass filter transmission $T_{BPF}(\lambda)$ was measured in the laboratory and used in this model. As incident scattered radiation $I_{0,TOA}(\lambda)$ a high-resolution top of atmosphere (TOA) solar spectrum is used (Chance and Kurucz, 2010). It is first multiplied by the ozone absorption $\exp(-\sigma_{O_3}(\lambda) \cdot S_{O_3})$ with the total atmospheric ozone slant column density S_{O_3} and weighted with λ^{-4} as a Rayleigh atmosphere is assumed, approximating scattered light from blue sky yielding

$$I_0(\lambda) = I_{0,TOA}(\lambda) \cdot e^{-\sigma_{O_3}(\lambda) \cdot S_{O_3}} \cdot f(\lambda^{-4}). \quad (3.2)$$

Finally, the trace gas absorption cross sections of species i of interest are added to Equation 3.2 with their corresponding column density S_i according to Bouguer-Lambert-Beer's law giving the radiation $I(\lambda) = I_0(\lambda) \cdot \exp(-\sum_i \sigma_i S_i)$ incident onto the aperture of the measurement device.

After traversing the optical components of the measurement device the radiance seen by each pixel of the detector is given by spectrally integrated radiance I_{FPI}

$$I_{FPI}(\alpha) = \int_{\lambda} I_0(\lambda) \cdot \exp(-\sum_i \sigma_i S_i) \cdot T_{BPF}(\lambda) \cdot T_{FPI}(\lambda; \alpha) d\lambda. \quad (3.3)$$

It is now possible to determine the optical density τ_{FPI} seen by the FPI as

$$\begin{aligned} \tau_{FPI}(\alpha) &= -\ln \left(\frac{I_{FPI}(\alpha)}{I_{0,FPI}(\alpha)} \right) \\ &= -\ln \left(\frac{\int_{\lambda} I_0(\lambda) \cdot \exp(-\sum_i \sigma_i(\lambda) S_i) \cdot T_{BPF}(\lambda) \cdot T_{FPI}(\lambda; \alpha) d\lambda}{\int_{\lambda} I_0(\lambda) \cdot T_{BPF}(\lambda) \cdot T_{FPI}(\lambda; \alpha) d\lambda} \right) \end{aligned} \quad (3.4)$$

where $I_{0,FPI}$ represents the trace gas free radiance as before derived in Equation 2.12. The FPI optical density $\tau_{FPI}(\alpha)$ is now a function of the incident angle α and the absorbing trace gas species i . The apparent absorbance AA_{FPI} can now be calculated as before, in Equation 2.24, for $\tau_{FPI}(\alpha_A)$ and $\tau_{FPI}(\alpha_B)$ with different light incident angles $\alpha_{A,B}$. In the model $\alpha_{A,B}$ are then independently varied until a maximum in AA_{FPI} is obtained

$$AA_{FPI} \stackrel{!}{=} AA_{FPI,max} = \tau_{FPI}(\alpha_A) - \tau_{FPI}(\alpha_B) = \tau_{FPI,A} - \tau_{FPI,B} = k_{max} \cdot S. \quad (3.5)$$

This yields the final operating settings α_A and α_B of the FPI resulting in the highest AA for a given S_i and thereby give highest sensitivity k_{max} to the trace gas i in the given band pass filter transmission window.

However due to the independent integrations of the numerator and denominator in Equation 3.4 the proportionality $\tau \propto S$ is not given any more as $k \neq const$. However, Equation 3.4 can be linearised under the assumption $\sigma \cdot S \ll 1$ yielding the proportionality $AA_{FPI} \propto S$. The linearisation procedure can be seen in Appendix A.1. Although, in the case of SO_2 measurement high values of S_{SO_2} are possible (e.g., volcanoes) that

can lead to a flattening of the calibration curve which is denoted as saturation effect. A qualitative explanation is, that high for optical densities τ trace gases are capable of absorbing almost the complete incident radiation (even more efficient at maxima of $\sigma_i(\lambda)$). For large τ , the recorded radiance in an on-band position will be attenuated less (almost all radiation is absorbed already) compared to the recorded radiance in an off-band position. This results in a smaller difference between $\tau_{FPI}(\alpha_A)$ and $\tau_{FPI}(\alpha_B)$ and therefore reducing the sensitivity of apparent absorbance.

To observe the cross sensitivities X to other trace gas species x , they have to be added to I_{FPI} as $\exp(-\sum_x \sigma_x S_x)$. The cross sensitivities X can then be obtained by once over calculating the AA_{FPI} at the earlier determined settings α_A and α_B including the interfering species. This yields $AA'_{FPI} = AA_{FPI} + X \Rightarrow X = AA'_{FPI} - AA_{FPI}$.

3.2 Model parameters and results

The parameters of the two FPIs used for the simulation of the instrumental response AA_{FPI} given by the Equations 3.4 and 3.5 are presented in Table 3.1. The FPIs were manufactured according to the calculations in Kuhn (2015) and were implemented as „air spaced“ FPIs (two fused silica mirrors filled with air). The FPIs plate distance were characterised in the laboratory since the manufacturer provides them with a tolerance of $0.1\mu\text{m}$, not sufficient for the simulation (see Section 4). The properties for the different band pass filters used are determined in the laboratory and are presented in the last three lines of Table 3.1.

The model procedures for the considered trace gases SO_2 , BrO , and HCHO were carried out identically. In general, the model can be split up in five steps, finally yielding the theoretical calibration curve, including the cross sensitivities with other trace gas species. The steps are:

1. The incident radiation $I_0(\lambda)$ is based on a high-resolution solar atlas spectrum $I_{0,TOA}(\lambda)$ according to Chance and Kurucz (2010). To model scattered sunlight the spectrum is scaled by λ^{-4} (Rayleigh atmosphere). Further, it is multiplied with the absorption $e^{-\sigma_{\text{O}_3}(\lambda) \cdot S_{\text{O}_3}}$ of a total slant atmospheric ozone column density ($S_{\text{O}_3} \approx 2.5 \cdot 10^{19} \text{ molec/cm}^2$; with 320 DU vertical O_3 column; solar zenith angle = 70°).
2. The integrated detected radiances $I_{FPI}(\alpha)$ and $I_{0,FPI}(\alpha)$ are calculated as functions of the incident angle $\alpha \in [0^\circ, 13^\circ]$. $I_{0,FPI}(\alpha)$ is trace gas free, whilst $I_{FPI}(\alpha)$ contains the examined trace gas absorption with a column density S typical for the measurement scenario (e.g. volcanic plumes).
3. The optical densities $\tau_{FPI}(\alpha)$ as a function of the incident angle α are calculated according to Equation 3.4. Based on this function, the minimum and maximum values of $\tau(\alpha)$ are determined, specifying the incidence angle α_A and α_B corresponding to a maximum value for AA_{FPI} .

3 Model study

4. By keeping the incidence angle α_A and α_B constant whilst the column density S is varied a calibration curve $AA_{FPI} = k \cdot S$ is calculated.
5. Cross sensitivities X to other trace gases are studied by including them in $I_{FPI}(\lambda)$. We used high but still appropriate column densities of interfering species for atmospheric background and volcanic plume conditions. Like in the previous point, a calibration curve for AA'_{FPI} is calculated. The difference between AA'_{FPI} , including the interfering species, and AA_{FPI} yields the cross interference $X = AA'_{FPI} - AA_{FPI}$.

This model study was performed for SO_2 , BrO , and HCHO , respectively. Potentially interfering species (O_3 , OCIO , NO_2) were added with column densities observed within volcanic plumes or the atmospheric background. In the case of SO_2 , the column densities of interfering trace gas species were chosen higher than usually abundant under volcanic conditions (see Figure 3.1, bottom panel). Hence it is possible to investigate the applicability at higher polluted scenarios like ship or industrial stack emissions. The absorption cross sections used in this model study are based on Vandaele et al. (2009), Fleischmann et al. (2004), Bogumil et al. (2003), Serdyuchenko et al. (2014) and Chance and Orphal (2011). The typical column densities values of the modelled and the potentially interfering species are based on Roscoe et al. (2010), Gliß et al. (2015), Bobrowski and Giuffrida (2012) and Dekemper et al. (2016).

Table 3.1: Parameters of the two FPIs, band pass filters combinations used for the simulations, and differential column densities, in [molec/cm^2] assumed for different measurement scenarios.

	SO_2	BrO	HCHO	
$d[\mu\text{m}]$	21.666	12.366		FPI plate separation
$\Delta\lambda_{FPI}[\text{nm}]$	2.111	4.414		FPI free spectral range
R	0.65	0.7		FPI Reflectivity
F	7.15	8.54		FPI finesse
n	1.000288			FPI refractive index (air)
$\lambda_{BPF}[\text{nm}]$	308.5	340.4		BPF central wavelength (CW)
$\delta_{BPF}[\text{nm}]$	9	10		BPF FWHM
$T_{max,BPF}$	0.63	0.85		BPF peak transmission
S_{SO_2}	1×10^{17}	3×10^{18}		
S_{BrO}	5×10^{14}	2×10^{14}	5×10^{13}	
S_{HCHO}	5×10^{16}	5×10^{15}	5×10^{16}	
S_{OCIO}	5×10^{13}	5×10^{13}		
S_{O_3}	3×10^{17}	3×10^{17}		
S_{NO_2}	1×10^{17}	1×10^{16}		

Column densities based on Roscoe et al. (2010), Gliß et al. (2015), Bobrowski and Giuffrida (2012) and Dekemper et al. (2016). Absorption cross sections are based on Vandaele et al. (2009), Fleischmann et al. (2004), Bogumil et al. (2003) and Serdyuchenko et al. (2014).

3.2.1 Model results for SO₂

The simulation results for SO₂ are presented in Figure 3.1. Typical SO₂ column densities can reach up to $S_{\text{SO}_2} = 10^{18}$ molec/cm² (Bobrowski and Giuffrida, 2012) or more. However, in this study a rather low column density of $S_{\text{SO}_2} = 10^{17}$ molec/cm² is assumed to demonstrate the applicability to emissions of weaker SO₂ concentrations. The calculated optical density $\tau(\alpha)$ is shown as function of the FPI incident angle α in the upper panel of Figure 3.1. The maxima and minima occur for on-band and off-band settings respectively. Possible on-band configurations are $\alpha_A \in \{4.5^\circ, \mathbf{8.17^\circ}, 10.66^\circ, 12.65^\circ\}$ and off-band configurations are $\alpha_B \in \{0.00^\circ, \mathbf{6.45^\circ}, 9.37^\circ, 11.56^\circ\}$. Due to internal reflections for small angles and a decrease in the FOV for high incidence angles of the FPI the selected operational angles are in the intermediate range (bold printed).

The spectral radiances for settings $\alpha_A = 6.45^\circ$ and $\alpha_B = 8.17^\circ$ (see middle panel Figure 3.1) show ragged structures, due to the high resolution spectrum used as I_0 . Further, the rapid increase of I_0 towards higher wavelengths is dominating the recorded radiance which is shifting the maximum of transmitted light to a higher wavelength than the band pass filter's central wave length (CW).

The calibration curve for AA_{FPI} with S_{SO_2} is shown in the bottom panel of Figure 3.1. The flattening of the function towards higher column densities is due to saturation effects, where the approximation of small optical densities does not hold (mathematical description, see Appendix A.1).

The theoretical sensitivity k_{SO_2} under atmospheric conditions for small column densities (linear term of a fitted polynomial) is $k_{\text{SO}_2} \approx 1.18 \times 10^{-19}$ cm²/molec giving a calibration function of

$$AA_{\text{SO}_2} \approx 1.18 \times 10^{-19} \text{ cm}^2/\text{molec} \cdot S_{\text{SO}_2} \Leftrightarrow \quad (3.6)$$

$$S_{\text{SO}_2} \approx 8.47 \times 10^{18} \text{ molec/cm}^2 \cdot AA_{\text{SO}_2}. \quad (3.7)$$

The cross interferences (see box in bottom panel of Figure 3.1) with other trace gas species (dashed lines) are hardly identifiable. By zooming in with a factor of about 100 (inlay, lower panel Figure 3.1), the cross interferences become visible. In the case of SO₂, the cross interferences to other trace gas species are very small, with high column densities assumed under volcanic conditions. Therefore it should be possible to apply the technique even in highly polluted scenarios (with NO₂ $\approx 1 \times 10^{17}$ molec/cm²) like e.g., ship or industrial stack emission.

3.2.2 Model results for BrO

Typical BrO column densities of volcanic plumes are in the regime of 10^{14} molec/cm², hence typical BrO/SO₂ ratios lie in the regime of 10^{-5} to 10^{-4} (Bobrowski and Giuffrida, 2012). We assumed a BrO column density of $S_{\text{BrO}} = 2 \times 10^{14}$ molec/cm². The model results are shown in Figure 3.2. The graphs are presented analogous to the model results of SO₂ (see Figure 3.1).

For BrO, a compromise between sensitivity and selectivity had to be made. The highest AA signal and therefore, the best correlation between FPI transmission and σ_{BrO}

3 Model study

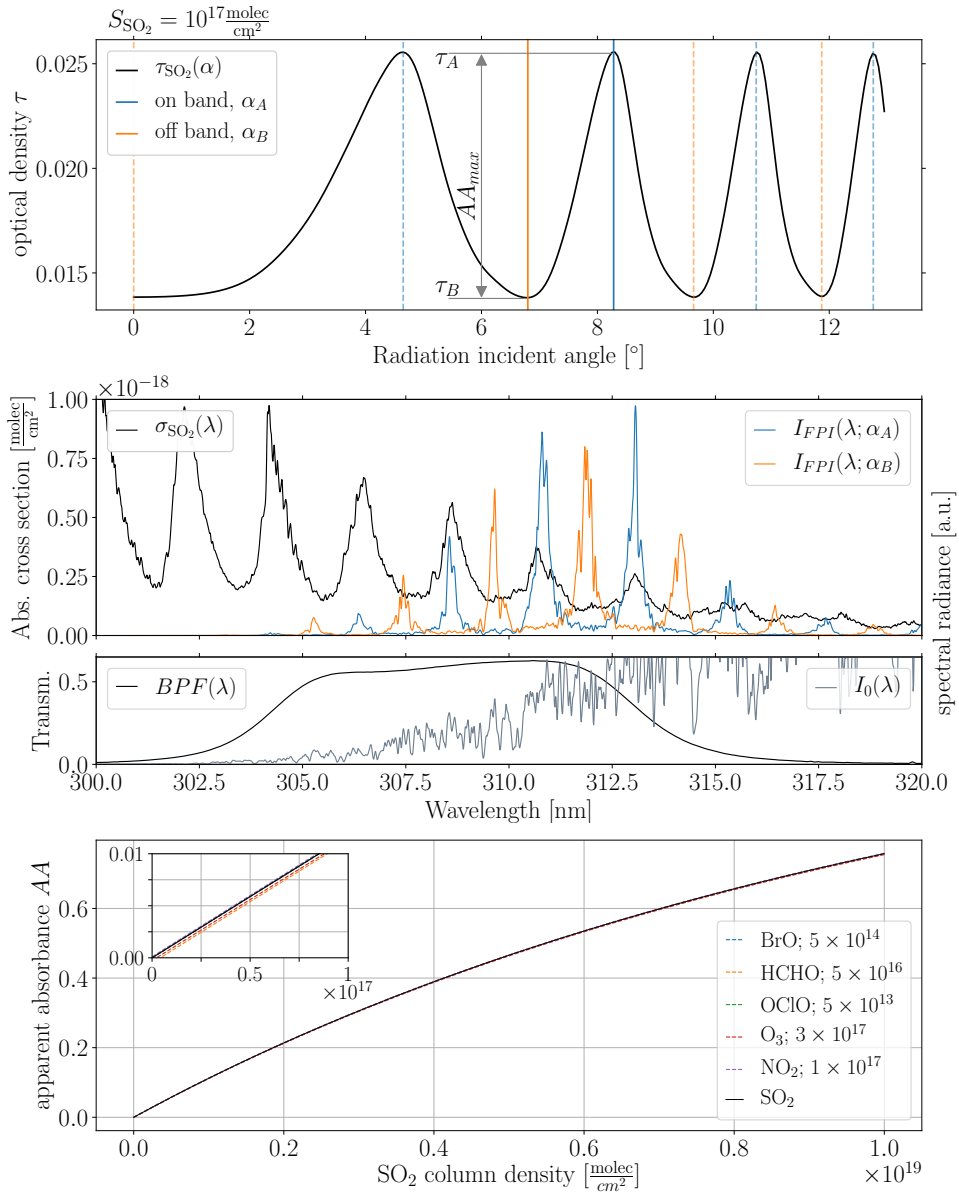


Figure 3.1: Model results for SO_2 . **upper panel:** The instrument response function for $\tau(\alpha)$ is shown. All maxima represent an on-band position (setting A, blue); all minima represent an off-band position (setting B, orange). The operating settings $\alpha_A = 8.17^\circ$ and $\alpha_B = 6.45^\circ$ resulting in a maximum apparent absorbance AA_{max} are indicated by drawn lines. **middle panels:** The recorded spectral radiances (integrand of Equation 3.3) are drawn for on-band (blue) and off-band (orange) setting in the upper panel. The correlation to differential structures of σ_{SO_2} can be seen. In the lower panel, the transmission of the employed band pass filter and the modelled scattered sunlight are presented. The product of $T_{BPF} \cdot I_0$ yields the envelope function of I_{FPI} . **bottom panel:** The calibration curve for SO_2 is shown (drawn line, black). Interfering species are included (dashed lines) with column densities in molec/cm^2 showing small cross sensitivities. The reduced slope of the calibration curve towards high S_{SO_2} is induced by saturation effects for high SO_2 column densities (see Section 3.1).

is achieved by using a band pass filter with CW 337 nm and FWHM of 10 nm shown in Appendix A.2. However, this results in a strong cross interference with SO₂ (see Figure A.2, bottom panel). By using a filter with identical FWHM but a CW of 340 nm these interferences can be reduced by several orders of magnitude (cf. bottom panels of Figure 3.2 and Figure A.2). Thereby, the loss in AA_{max} is small. For a BrO column density of $S_{BrO} = 2 \times 10^{14}$ molec/cm² the AA_{max} obtained using the filter with a CW of 337 nm is $AA_{max,337} = 1.33 \times 10^{-3}$. For the filter with a CW of 340 nm the obtained $AA_{max,340}$ is $AA_{max,340} = 1.24 \times 10^{-3}$. Hence, this corresponds to a loss in sensitivity of approximately seven percent.

The modelled instrument response for a BrO with a column density of $S_{BrO} = 2 \times 10^{14}$ molec/cm² as a function of incidence angle α is shown in the upper panel of Figure 3.2. The possible on-band settings are $\alpha_A \in \{1.35^\circ, \mathbf{9.60^\circ}\}$ and off-band settings are $\alpha_B \in \{\mathbf{6.10^\circ}, 11.30^\circ\}$. The maximum AA_{max} is obtained for the bold printed incidence angles, which will later be used to operate the FPI instrument.

In the selected spectral range of (340 ± 5) nm the FPI transmission profile is dominated by the band pass filter transmission as I_0 is quite constant in magnitude. Due to the higher FSR required for BrO, the correlation between T_{FPI} and σ_{BrO} is limited by the filter to three maxima or minima respectively.

The cross interferences with other trace gas species (see box with column densities, bottom panel, Figure 3.2) exhibit a higher impact in comparison to SO₂. The calculated sensitivity k_{BrO} for volcanic plume measurements using scattered sunlight is $k_{BrO} \approx 6.21 \times 10^{-18}$ cm²/molec yielding the calibration function

$$AA_{BrO} \approx 6.21 \times 10^{-18} \text{ cm}^2/\text{molec} \cdot S_{BrO} \Leftrightarrow \quad (3.8)$$

$$S_{BrO} \approx 1.61 \times 10^{17} \text{ molec/cm}^2 \cdot AA_{BrO}. \quad (3.9)$$

Cautiousness has to be taken concerning HCHO as the FPI settings for BrO and HCHO are almost identical (see Section 3.2.3). In this thesis, this feature was exploited and used for laboratory measurements to characterise the application of an FPI instrument on BrO (see Section 5.4).

3.2.3 Model results for HCHO

The simulated results for HCHO with an assumed column density of $S_{HCHO} = 5 \times 10^{16}$ molec/cm² are presented in Figure 3.3 analogous to the results of SO₂ and BrO (see Figure 3.1 and Figure 3.2). Additionally, the AA_{BrO} (upper panel) and σ_{BrO} (middle panel) are included to illustrate the similarity between HCHO and BrO.

In the upper panel of Figure 3.3 the calculated AA_{HCHO} for different radiance incident angles α is shown. The obtained angles for on-band and off-band settings are $\alpha_A \in \{1.10^\circ, \mathbf{9.55^\circ}\}$ and $\alpha_B \in \{\mathbf{6.15^\circ}, 11.35^\circ\}$ respectively, where the bold printed values are used for the operation of the FPI instrument. For comparison: The determined BrO on-band and off-band settings were $\alpha_{A,BrO} \in \{1.35^\circ, \mathbf{9.60^\circ}\}$ and $\alpha_{B,BrO} \in \{\mathbf{6.10^\circ}, 11.30^\circ\}$.

In the middle panels of Figure 3.3 the spectral radiances of T_{FPI} are plotted for setting

3 Model study

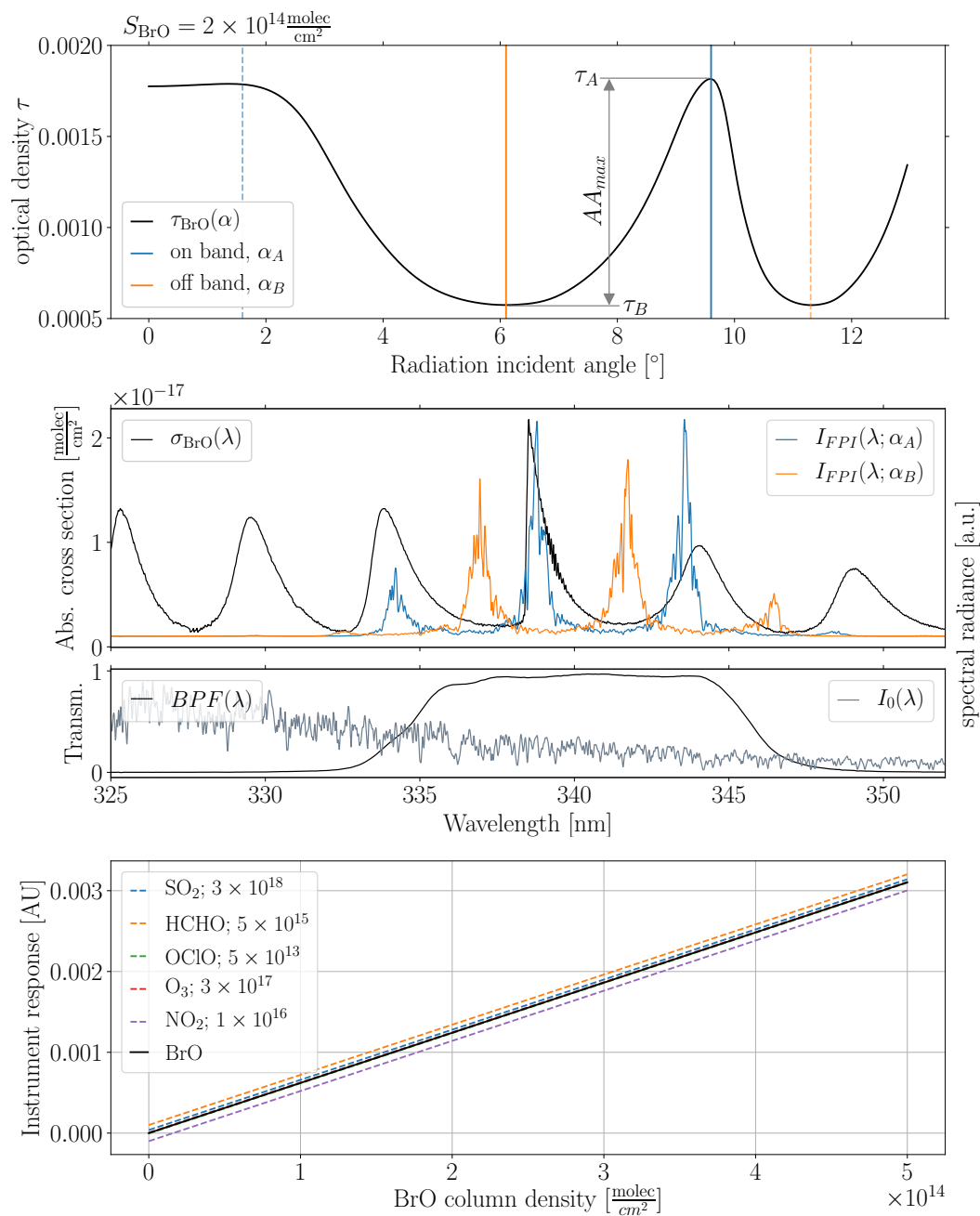


Figure 3.2: Model results for BrO. Analogous to Figure 3.1. **upper panel:** The operating settings $\alpha_A = 9.60^\circ$ (drawn, blue line) and $\alpha_B = 6.10^\circ$ (drawn, orange line) resulting in a maximum apparent absorbance AA_{max} . **middle panels:** The recorded spectral radiances are shown for on-band (blue) and off-band (orange) settings in the upper middle panel, with corresponding filter transmission (CW 340nm) and incidence spectrum in the lower middle panel. **bottom panel:** The calibration curve for BrO is shown (drawn line, black). Interfering species are included (dashed lines) with column densities in molec/cm².

α_A and α_B . The correlation in on-band setting is in the case of HCHO restricted by the band pass filter transmission to two absorption peaks of σ_{HCHO} . Again σ_{BrO} is shown to demonstrate the similar spectral features of the absorption cross section. The calibration curve for HCHO is plotted in the bottom panel of Figure 3.3. Only weak cross interferences to other trace gas species exist except for BrO. A reduced slope of the calibration curve due to saturation effects can not be observed in the regime up to column densities of $S = 5 \times 10^{17}$ molec/cm². The theoretical sensitivity under atmospheric measurement conditions is $k_{\text{HCHO}} \approx 1.99 \times 10^{-20}$ giving the calibration curve for HCHO

$$AA_{\text{HCHO}} \approx 1.99 \times 10^{-20} \text{ cm}^2/\text{molec} \cdot S_{\text{HCHO}} \Leftrightarrow \quad (3.10)$$

$$S_{\text{HCHO}} \approx 5.02 \times 10^{19} \text{ molec/cm}^2 \cdot AA_{\text{HCHO}}. \quad (3.11)$$

The study of HCHO resulted from lab studies, exploiting the cross interference with BrO. The performance of an HCHO FPI CS measurement would be much better with optimised instrument parameters (see Section 5.4). It should be noted that typical HCHO levels in volcanic plumes were found to be rather low with $S_{\text{HCHO}} < 5 \times 10^{15}$ molec/cm².

3 Model study

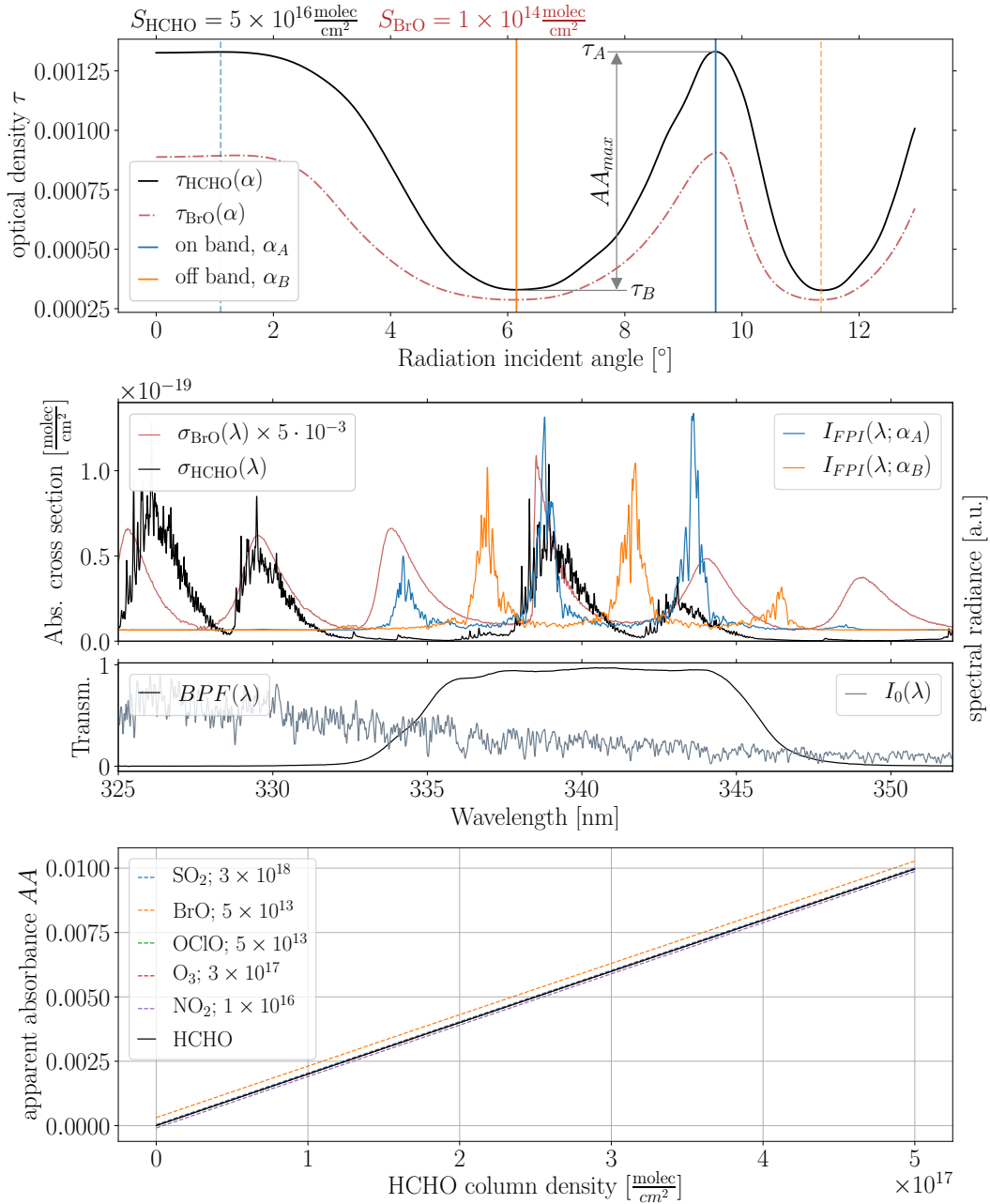


Figure 3.3: Model results for HCHO. Analogous to Figure 3.1 and 3.2. **upper panel:** The operating settings $\alpha_A = 9.55^\circ$ (drawn, blue line) and $\alpha_B = 6.15^\circ$ (drawn, orange line) resulting in a maximum apparent absorbance AA_{max} . Additional, the τ_{BrO} for $S_{BrO} = 10^{14} \text{ molec/cm}^2$ (dashed red) to demonstrate similarity of the instrument response between HCHO and BrO. **middle panels:** The recorded spectral radiances are shown for on-band (blue) and off-band (orange) setting in the upper middle panel, with corresponding filter transmission (CW 340nm) and incidence spectrum in the lower middle panel. **bottom panel:** The calibration curve for HCHO is shown (drawn line, black). Interfering species are included (dashed lines) with column densities in molec/cm².

4 The realistic Fabry-Perot Interferometer

FPIs are frequently employed in high precision applications, e.g., single-mode LASERS, H α telescopes, or gravitational wave detectors. In the field of volcanic remote sensing and for the development of a new measurement technique, the FPI needs to meet the requirements of both, accuracy and robustness at the same time. The manufacturer provided the FPIs with additional features to minimise disturbing side effects (e.g. reflections) and specified the physical properties with high tolerances that are not sufficient for our model and the application. In this chapter, the crucial features for measurements are characterised and the physical specifications are refined in the laboratory.

The FPIs for SO₂ and BrO measurements used in this thesis are provided by *SLS Optics Ltd.*. They consist of two fused silica plates, mounted inside a steel housing with a clear aperture of 20 mm (see Figure 4.1). The inner surfaces have reflective coatings with $R_{\text{SO}_2} = 0.65$ and $R_{\text{BrO}} = 0.70$ and the space in between is filled with air. The SO₂ FPI is designed for a wavelength of 305 nm giving refractive indices of $n_{\text{SO}_2,\text{air}} = 1.0029$ and $n_{\text{SO}_2,\text{glass}} = 1.4864$ for fused silica glass. The FPI optimized for BrO has a design wavelength of 330 nm yielding refractive indices of $n_{\text{BrO},\text{air}} = 1.0029$ and $n_{\text{BrO},\text{glass}} = 1.4792$ (values from Polyanskiy). In order to avoid interferences from reflections at the outer surfaces they are anti reflex coated for UV radiation (reflex coating loss 0.25%) and have opposed wedge angles of 0.5°. The wedges cause the radiation propagating on the optical axes to be slightly inclined

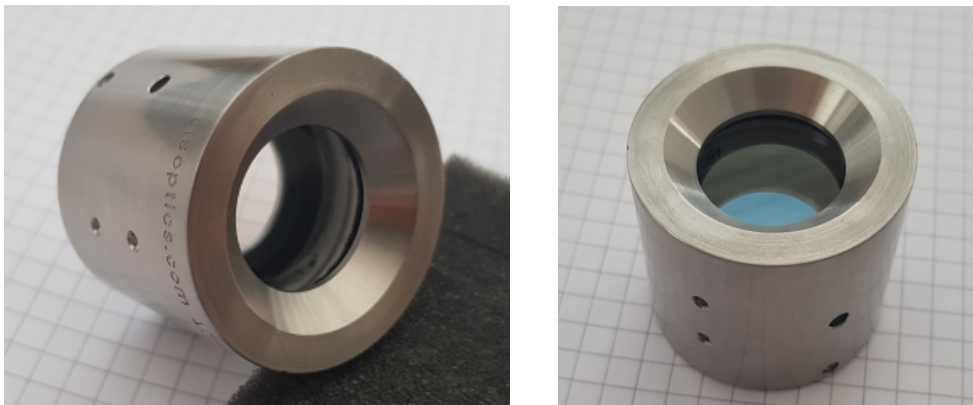


Figure 4.1: FPI manufactured by *SLS Optics Ltd.*. The fused silica plates are fitted into a steel reel with a clear aperture of 20 mm. The steel cell diameter is 38 mm and has a length of 34.5 mm.

4 The realistic Fabry-Perot Interferometer

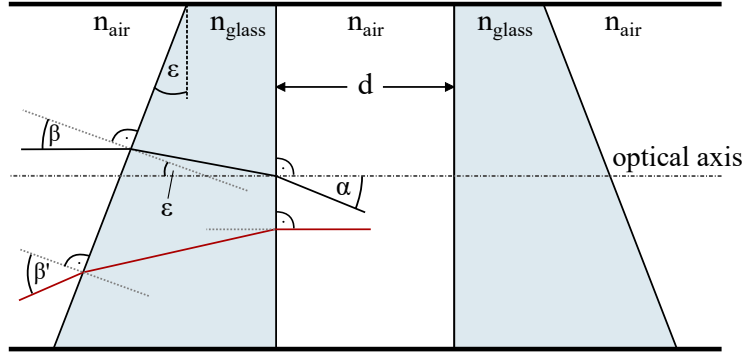


Figure 4.2: Schematic of the internal setup of an FPI (drawn overstated for clarity). The opposed wedge angles $\varepsilon = 0.5^\circ$ are part of the fused silica plates hence forming two trapezoids. A beam of light propagating parallel to the optical axis (black) will incidence onto the outer surface with angle β , which will be equal to the wedge angle $\beta = \varepsilon$. Following Snell's law, the radiation gets refracted and induces that beam will be inclined by α inside the etalon. For a particular angle of incidence β' , the light beam will be parallel to the optical axis inside the etalon (red).

inside the etalon (see Figure 4.2). The inclination α in respect to the optical axis is given by

$$\alpha = \arcsin \left(\sin(\varepsilon) \cdot \sqrt{\frac{n_{glass}^2}{n_{air}^2} - \sin^2(\beta)} - \sin(\beta) \cdot \cos(\varepsilon) \right) \quad (4.1)$$

with the wedge angle $\varepsilon = 0.5^\circ$, the angle of incidence β and the refractive indices of air n_{air} and fused silica glass n_{glass} . In example, a beam parallel to the optical axis ($\beta = \varepsilon = 0.5^\circ$) experiences an inclination of $\alpha = 0.42^\circ$. The derivation of Equation 4.1 is shown in Appendix A.3. The angle α inside the etalon determines the FPI transmission spectrum and is therefore of great importance throughout this study. The angle α was varied in the model and all measurements will refer to it.

The alignment axis of the wedge angles is not indicated and hence needs to be determined. The plate separation stated by the manufacturer is specified with $d_{SO_2} = 21.580 \mu\text{m}$ and $d_{BrO} = 12.330 \mu\text{m}$. The stated tolerances for the plate separation d are $0.100 \mu\text{m}$, which is not sufficient, neither for the model study, nor the calibration of the FPI instrument and therefore needs to be assessed more precisely.

In the following sections, a procedure to determine a more precise value for the plate separation d is explained. This procedure will further yield a state of zero inclination angle within the FPI and the orientation of the wedge angles. The general property exploited in all measurements is that for a decreasing inclination of $\alpha \rightarrow 0$, the FPI transmission peaks are shifted towards higher wavelengths (see Equation 3.1). The alignment with $\alpha = 0$ will be further referred to as „zero position“ of the applied instrument.

The measurements are performed with artificial light sources, in our case, two UV-

LEDs: for the SO₂ FPI with a CW of 305 nm and for the BrO FPI with a CW of 341 nm. The emitted light is diffused by a diffuser plate first. The diffused light is passing an aperture of ≈ 0.8 mm and a lens parallelising the beams. Afterwards the light is traversing the FPI and will be focused onto a fibre optic to measure the FPI transmission by a temperature stabilised spectrometer (*Avantes, AvaSpec-ULS2048*). To enable tuning of the FPI by varying the incident angle, it is mounted on a stepper motor with a step resolution of $6.25^\circ \times 10^{-3}$.

All measurements for the SO₂ and BrO FPI are performed analogous, therefore, the methodology is shown exemplary for the SO₂ FPI only.

4.1 The FPI wedge angle alignment

The determination of the wedge angle alignment is performed by rotating the FPI with respect to its optical axis. A rotation can induce a variation of the incident angle β , which leads to a change in α . This causes a shift in the transmission spectrum.

In general, there are two possible scenarios. First, if the incoming radiation is parallel to the optical axis with $\beta = \varepsilon$ (black beam in Figure 4.2). The rotation of the FPI around its optical axis will not result in a variation of the inclination angle α inside the etalon. The orthonormal of the outer surface will „rotate“ around the incoming beam, keeping $\beta = \varepsilon = \text{const}$. In the second scenario, radiation is propagating on a direction not parallel to the FPI optical axis (e.g., red beam in Figure 4.2). The rotation of the FPI will yield to an oscillation of the incident angle β with an amplitude of $\pm\varepsilon$. In absolute values (keeping $\beta = \text{const}$) this oscillation corresponds to a variation of $2 \times \varepsilon$ of the incidence angle β resulting in a change of the inclination angle α by $\approx 1.5^\circ$ for $\beta < 13^\circ$.

The transmission spectrum T_{FPI} is a function of $\cos(\alpha)$ (see Equation 3.1). Thus, the variation of 1.5° will induce only a small shift in the transmission spectrum if $\alpha(\beta)$ inside the FPI etalon is small (shift $\Delta_1 = 0.11$ nm for $\alpha = 0^\circ$, see black spectrum in Figure 4.3). However, the effect can be amplified by biasing $\alpha(\beta)$ before rotating the

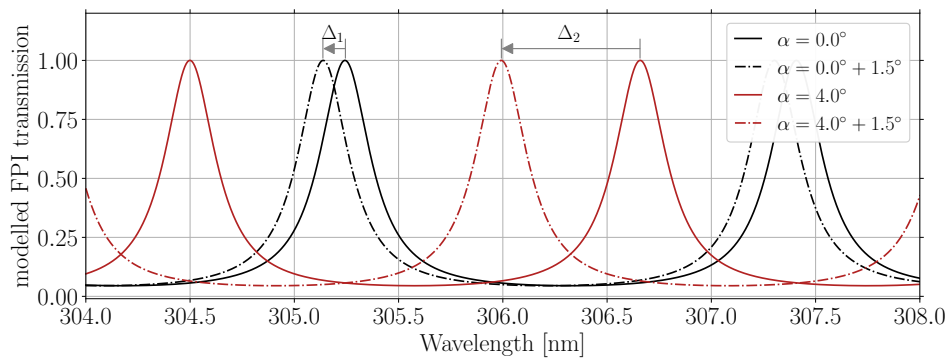


Figure 4.3: Maximum shift in the SO₂ FPI transmission spectrum over the wavelength induced by a rotation around the optical axis for different angles of α . Increasing $\alpha = 0^\circ \rightarrow \alpha = 0^\circ + 1.5^\circ$ induces the shift $\Delta_1 = 0.11$ nm (black). Biasing α to an higher angle the variation yields a shift of $\Delta_2 = 0.67$ nm for an increase of $\alpha = 4^\circ \rightarrow \alpha = 4^\circ + 1.5^\circ$ (red).

4 The realistic Fabry-Perot Interferometer

FPI (shift $\Delta_2 = 0.67$ nm for $\alpha = 4^\circ$, see red spectra in Figure 4.3). The bias for $\alpha(\beta)$ can be generated by a tilt (increasing β) of the FPI optical axis within the parallelised light beam.

During the measurement, the FPI optical axis was tilted with respect to the propagation direction of the parallelised light by $\approx 9^\circ$. The starting point of the rotation (0°) is selected arbitrarily, and the full rotation of 360° is divided into equidistant steps of 45° . The measurement results are presented in Figure 4.4.

The oscillation of T_{FPI} is visible and reaches the maximum shift towards small wavelengths at 0° rotation and towards high wavelengths for 180° . Hence, for these positions, the wedge angle is aligned in the direction of the bias tilt. For angles of 135° and 270° the wedge angle is orientated perpendicular with respect to the bias tilt of the FPI optical axis.

Based on these results, the FPI is marked to identify the wedge alignment. In further measurements, the FPI will be assembled in the instrument according to the orientation of 180° however, the orientation of 0° could be utilised likewise. In the instrumental setup, the FPI optical axis can be tilted back and forth in just a single direction. Hence, the only possibility to approach a setting with $\alpha = 0$ is by utilizing one of these two confined alignments. In all other orientations, the wedge angle will induce a slight inclination of α with respect to the optical axis within the etalon.

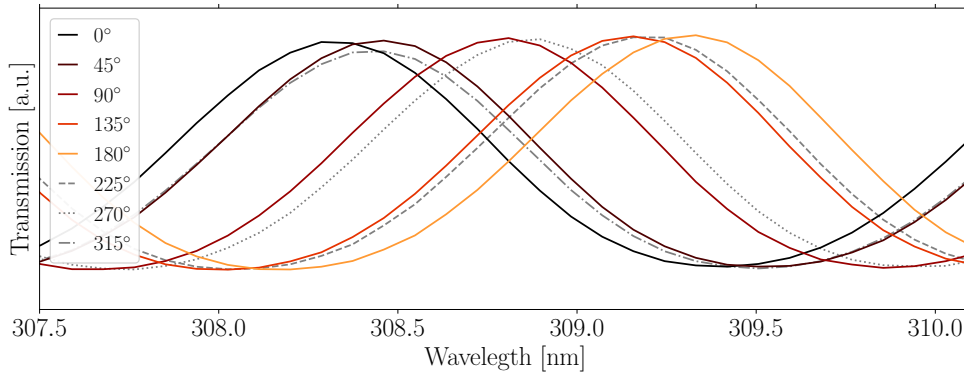


Figure 4.4: Shift of the FPI transmission spectrum T_{FPI} induced by a rotation (zoomed to one set of maxima). The FPI optical axis was tilted by $\approx 9^\circ$ within the parallelised light. First position (0°) is selected arbitrarily and the full revolution of 360° is divided in equidistant steps of 45° . The shift of T_{FPI} can be seen from small to high wavelengths (black to orange; $0^\circ \rightarrow 180^\circ$) with a maximum for 180° . For rotational angles higher 180° (dashed grey) the spectra are shifting backwards to the initial position.

4.2 Determination of the FPI zero position

The zero position of the FPI specifies the setting where the inclination $\alpha = 0$ inside the etalon yielding the maximum shift of T_{FPI} towards high wavelength. Hence this position is determining the initial point of tilting or tuning the FPI within the instrument.

4.2 Determination of the FPI zero position

To determine the zero position, an approach similar to the preceding section is applied. The FPI needs to be inserted in the instrument as described in Section 4.1 with correct alignment of the wedge angles and further, the optical axis will be tilted with respect to the parallelised incident radiation by some degrees. By reducing the applied tilt, a shift of the T_{FPI} transmission peaks towards higher wavelengths can be observed. The zero position and therefore $\alpha = 0$ can be identified by the spectrum peaking at the longest wavelength. After exceeding this setting, the spectrum will shift to smaller wavelengths as α increases again.

For the measurement, the FPI is mounted on a stepper motor with an additional 1/9 transition gear. The initial motor position is determined by an optical end switch (for more details see Section 6.3 & 6.5). The stepper motor rotation is encoded in units of μ -steps. A full revolution (incl. transition gear) of 360° accounts for 57.600 μ -steps. The starting point for the measurement was chosen by the end switch position SWP (reached by clockwise rotation) plus 740 μ -steps ($\approx 4.6^\circ$). In this setting, the FPI optical axis was visibly deflected from the instrumental optical axis. The displacement was consecutively reduced by equidistant steps of 50 μ -steps until the zero position was exceeded, which is visible by the reversal in the shift of the FPI transmission spectrum. The measurement results are shown in Figure 4.5.

The zero position for the SO₂ FPI, therefore, lies between 540 μ -steps and 490 μ -steps. A second, higher resolved measurement sequence, yields the final zero position as:

Zero Position: SO₂ FPI SWP + 510 μ -steps
 BrO FPI SWP + 460 μ -steps

In the FPI camera, these positions are referred to as zero for tilting (tuning) the FPI by the stepper motor (Note: These positions will change with modifying the setup).

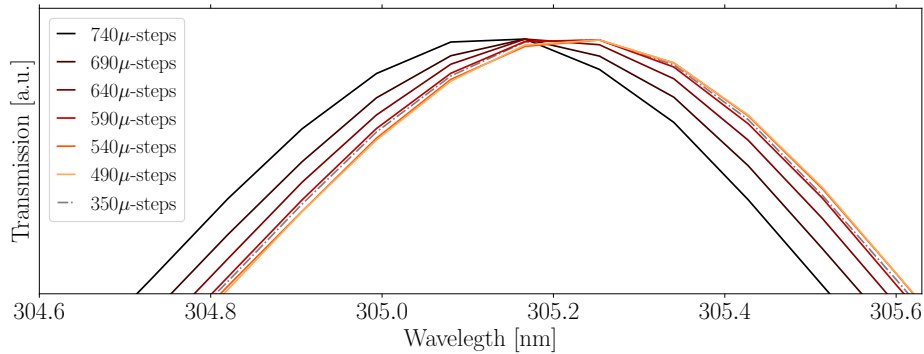


Figure 4.5: Shift of T_{FPI} towards higher wavelengths when the FPI tilt approaches the zero position. Initial deflection by 740 μ -steps is reduced consecutively by 50 μ -steps (black to orange lines). The spectra for a deflection of 540 μ -steps and 490 μ -steps are hardly discriminable, indicating the transgression of the zero position. The reversal in the shift due to transcending the zero position (zero degree tilt) can be seen for a deflection of 350 μ -steps (dashed grey).

4.3 Determination of the FPI plate distance

For a more accurate determination of plate distance d , the FPI wedge angles have to be aligned parallel to the tilt direction according to Section 4.1 and the optical axis has to be positioned in zero position as described in Section 4.2. The resulting FPI transmission spectrum now corresponds to $T_{FPI}(\alpha = 0)$ with light beams entering the etalon perpendicularly. In this setting, the transmission peaks are at their highest reachable wavelength. This defines a physical upper boundary for shifting the FPI transmission spectrum.

The modelled instrument transmission function (see Equation 3.1) allows for the assessment of the real optical plate separation. The incoming radiation in the model is a spectrum of the employed artificial light source that was recorded in the laboratory. As the inclination angle is fixed to $\alpha = 0$ in this setting, the only free parameter left in the model is the plate distance d . The separation d_0 specified by the manufacturer is adjusted in the model to d_{model} until the simulated transmission spectrum $T_{FPI,model}$ matches the measured $T_{FPI,meas}(\alpha = 0)$.

The results are shown in Figure 4.6. Using the plate distance stated by the manufacturer with $d_0 = 21.580 \mu\text{m}$ the model is not reproducing the determined spectrum for $\beta = 0$ (cf. $T_{FPI,meas}$ and $T_{FPI,model}(d_0)$) (black and grey) spectra in Figure 4.6). A slight adjustment, which lies in the given tolerances of $0.100 \mu\text{m}$, by $d_{model} = (21.580 + 0.086) \mu\text{m}$ yields an FPI transmission spectrum matching the recorded spectrum with an error of $\pm 0.002 \mu\text{m}$ (cf. $T_{FPI,meas}$ and $T_{FPI,model}(d_{model})$) (black and red spectra) in Figure 4.6).

The plate distance d_{model} was used in the model study and will further be referred to as d . The same analysis was applied for the BrO FPI yielding $d_{model} = (12.330 + 0.036) \mu\text{m}$ with an error of $\pm 0.002 \mu\text{m}$. The thereby determined optical plate separations are:

Plate distance d	SO₂ FPI	$(21.666 \pm 0.002) \mu\text{m}$
	BrO FPI	$(12.366 \pm 0.002) \mu\text{m}$

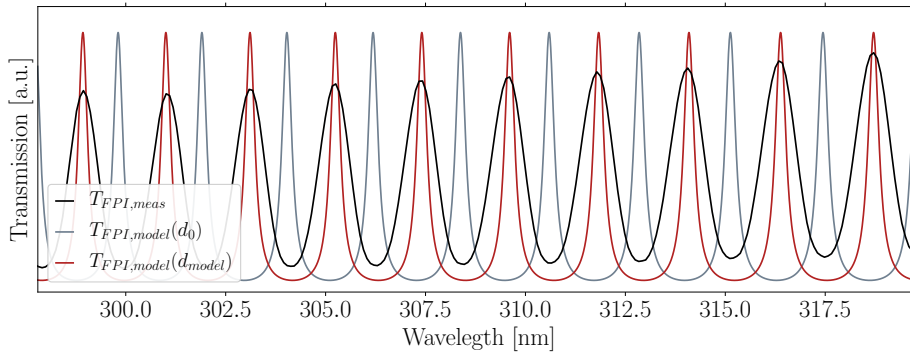


Figure 4.6: The measured $T_{FPI,meas}$ (black) for $\alpha = 0$ and modelled $T_{FPI,model}$ spectra (red and grey). The grey transmission spectrum $T_{FPI,model}(d_0)$ is simulated with $d = 21.580 \mu\text{m}$ (specified by the manufacturer) and exhibits a discrepancy in respect to the measured spectrum $T_{FPI,meas}$. Adjusting the plate distance by $d_{model} = d_0 + 0.86 \mu\text{m}$ yields the red spectrum $T_{FPI,model}(d_{model})$ matching the recorded transmission spectrum. Note that the apparently lower finesse of the measured transmission spectrum originates from the spectrometers resolution of 0.8 nm .

5 The one-pixel FPI instrument

A one-pixel FPI prototype (OP FPI) was used to study the performance of the FPI CS technique apart from imaging applications. A proof of concept study was performed for BrO (HCHO) in order to investigate the feasibility of a more complex imaging instrument.

The basic setup of an OP FPI was described in a conceptual study by Kuhn (2015), including the characterisation of optics and electronics and instrumental performance for the detection of SO₂.

In the first part of this section, the OP FPI setup and characterisation will be discussed briefly. For a more comprehensive treatment see Kuhn (2015). In the second part, the exploitation of HCHO as a spectral proxy for BrO in laboratory measurements is explained, including the preparation of HCHO gas cells and their application. Further, the first measurement results, limiting factors and difficulties in the application of the OP FPI device for laboratory measurements will be described.

5.1 The one-pixel FPI instrument setup

The OP FPI is a prototype with relatively simple optomechanics and electronics. A photograph and schematic setup is shown in Figure 5.1.

The FPI's clear aperture is 20 mm, which is reduced when the FPI is tilted. Therefore an iris aperture in front of the FPI limits the instrumental clear aperture to 10 mm. After the radiation traverses the FPI, a plano-convex lens with $f = 50$ mm focuses the light onto the OP detector, which is an UV sensitive SiC photodiode. The band pass filter is located between the lens and photodiode and is placed close to the detector to minimise stray light.

A servomotor is used for tilting the FPI. To increase the tilt resolution, a simple gearing lever is used (see Figure 5.1). An Arduino microcontroller controls the servo motor. The Arduino board is additionally equipped with a temperature and pressure sensor, which enables to monitor environmental conditions of the instrument.

The photocurrent of the SiC photodiode is amplified by a transimpedance amplifier circuit, where the current is converted into a proportional output voltage. The output voltage is digitised by an analog-to-digital converter (ADC), yielding a digital signal with a resolution of 21 bits. The amplifier circuit is mounted within a grounded aluminium housing for electromagnetic shielding. The circuit was designed by Tirpitz (2016). The output signal is recorded by an Arduino and via serial communications transmitted to a computer.

5 The one-pixel FPI instrument

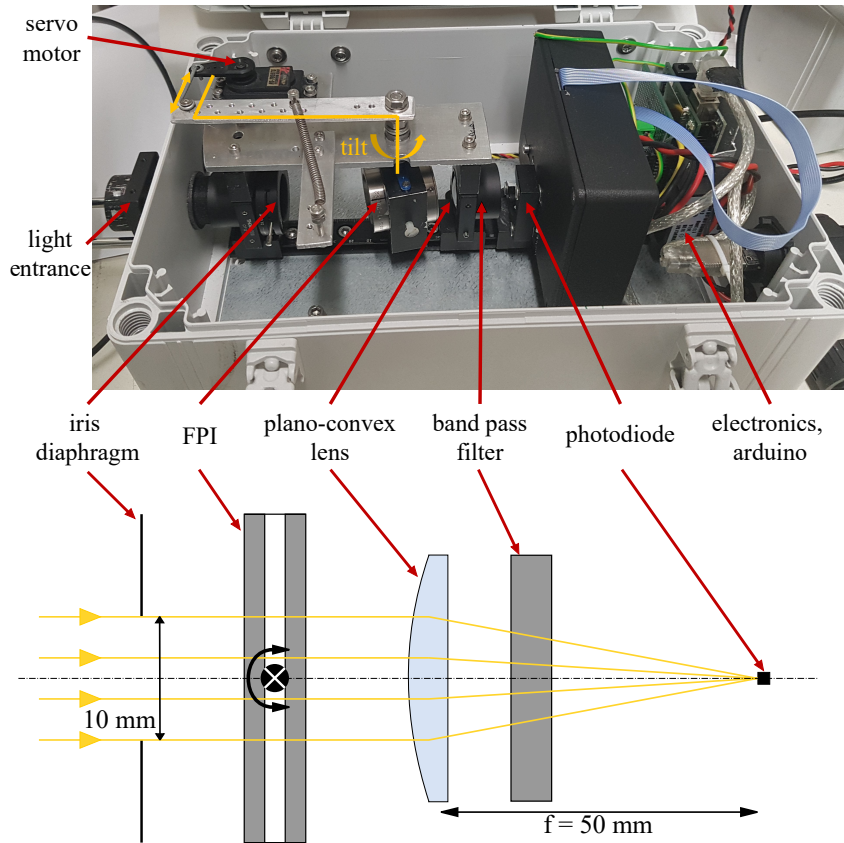


Figure 5.1: upper panel: Photograph of the full OP FPI setup used for measurements. Optomechanics and electronics are mounted within a water- and dust-proof polycarbonate box for field experiments. **lower panel:** Schematic drawing of the optical setup. The selection of parallelised light is performed by a single lens focusing the radiation onto an OP detector.

5.2 Output noise characterisation

The output noise of the OP FPI summarises all noise contributions generated by the detector and electronics. It consists of the photoelectron shot noise, the thermal noise of the electronics, the ADC output noise, and the current and voltage noise of the amplifier circuit. In the following discussion, the values given represent the root mean square (RMS) noise.

The photoelectron shot noise is a quantum noise effect induced by the random statistical fluctuations of the incident radiation and electrons current. It obeys Poisson statistics and therefore, the RMS is given by $\sqrt{N_e}$, with N_e the number of photoelectrons released from the detector. Electronic noise is always present in electronic circuits and is a result of the thermal agitation of electrons within the present electronic conductors. One component is following the Boltzmann statistics another component is proportional to $\sqrt{T \cdot R \cdot \Delta f}$ with the absolute temperature T , the ohmic resistance R of the electronic components and the bandwidth Δf over which the noise is measured.

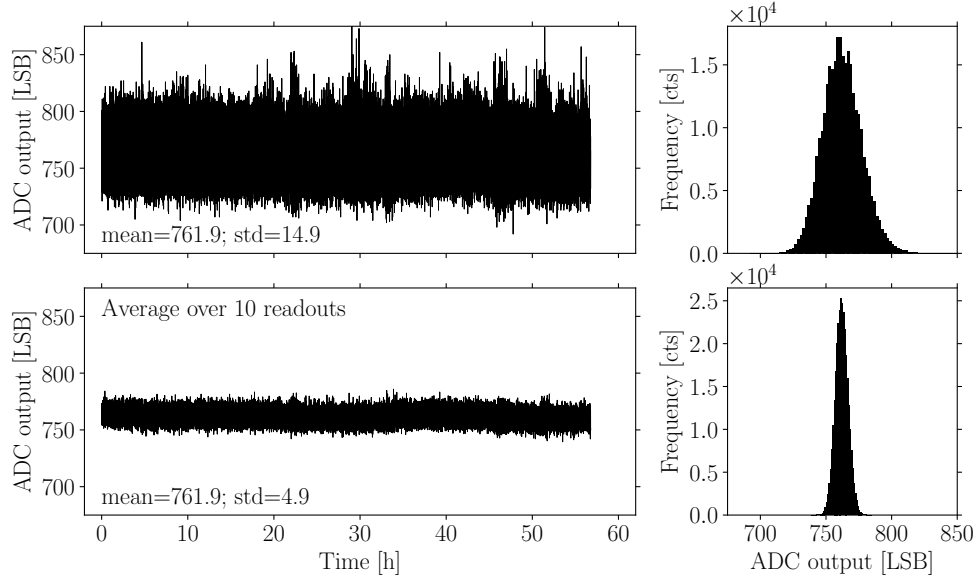


Figure 5.2: The electronic output noise measurement (dark measurement). **upper left panel:** Direct ADC readouts with a frequency of 1.5 Hz over 57 hours. **lower left panel:** Time series shown consists of the average over 10 readouts (≈ 6 s). **right panels:** The corresponding histograms are plotted.

The total electronic output noise is investigated in a long-term measurement over 57 hours, which is presented in Figure 5.2. The measurement of the intrinsic electronic output noise was performed by a dark measurement, with all electronic components running. The raw values with a time resolution of ≈ 1.5 Hz are shown in the upper panel. In the lower panel, an average over ten consecutive voltage readouts is applied. The expected decrease of the RMS noise by a factor of $\sqrt{10} \approx \frac{14.9 \text{ LSB s}^{-1/2}}{4.9 \text{ LSB s}^{-1/2}}$ (LSB: least significant bit) can be observed. The electronic offset has a value of 761.9 LSB and is low in comparison with the expected measurement signal in the order of 10^6 LSB.

By averaging the readouts over 5 minutes (≈ 450 readouts) the noise is further reduced, the temperature dependence of thermal noise becomes visible as shown in Figure 5.3. By applying a linear regression to a scatter plot, the offset-temperature correlation $\Delta(T)$ can be determined, as

$$\Delta(T) = (0.39 \pm 0.01) \frac{\text{LSB}}{\text{K}} \cdot T + 5.08 \text{ LSB} \quad (5.1)$$

where T is the absolute temperature in units of Kelvin. The coefficient of determination of the linear regression is $r^2 = 0.67$. For typical, expected gas concentrations and over a temperature range from -10 to 40 °C this induces only negligible errors of $< 10^{-5}$ on the retrieved optical densities. The dominating factor of the output noise is the photoelectron shot noise ($\propto \sqrt{N_e}$) for high radiances (see detector noise analysis in Kuhn (2015)).

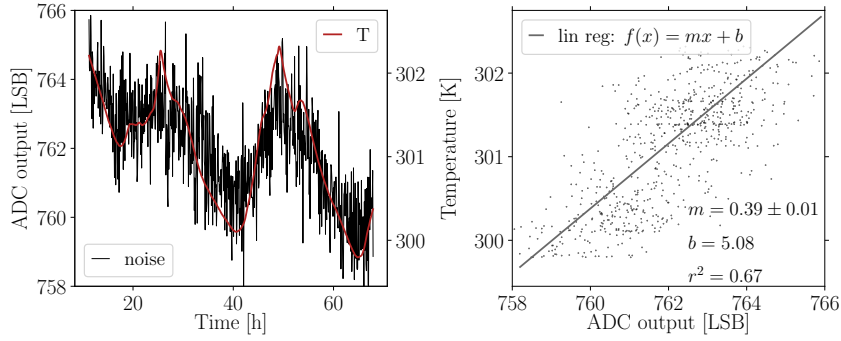


Figure 5.3: Left: The 5 minutes average of the 57-hour dark measurement of the output noise and temperature. Right: Scatterplot of temperature over output noise. A linear regression is applied, giving a coefficient of determination of $r^2 = 0.67$.

5.3 Selection of a suitable light source for calibration

An artificial light source simplifies characterising the instrument setup in the laboratory. The emission spectrum of the artificial light source should cover the instrument spectral range and should yield a temporally constant absolute intensity. Xe arc lamps are frequently used for spectroscopic UV-Vis measurements of trace gases. The emittance starts in the UV at around 240 nm and is further covering the complete visible spectral range. Despite the broadband spectral emittance of the Xe lamp, the variation of the absolute radiance on short time scales (in the order of 1%) is too high for an application with the OP FPI instrument. Since the spectral information is collected by recording different spectral channels consecutively. For each channel, the absolute spectrally integrated radiance is captured. To reduce the impact of intensity fluctuations of the light source, a UV light emitting diode (UV LED) can be employed instead of the Xe lamp. The intensity fluctuations of an LED are about one order of a magnitude lower in comparison to the Xe lamp. However, the spectral range of the emitted radiation is reduced.

To investigate the stability of intensity and long term drifts, two measurements were performed over 48 hours for a Xe lamp and a UV LED with central wavelength (CW) of 340 nm and an FWHM of 10 nm for the BrO instrument setup. The results are shown in Figure 5.4.

By tuning the FPI between two positions, the intensity is recorded for two different spectral channels to simulate a trace gas measurement. In the case of the Xe lamp, seven readouts are averaged and the temporal resolution for a measurement of the intensities in both channels is ≈ 1.8 s. For the UV LED, five readouts are averaged and the temporal resolution to record intensities in two channels is ≈ 1.5 s. To simulate a coincident record of intensities in channel one I_1 and channel two I_2 (on-band and off-band), one series of intensities is temporally interpolated. After correcting the intensities for electronic offset the logarithmic ratio $\ln(R) = \ln(I_1/I_2)$ is calculated to

5.3 Selection of a suitable light source for calibration

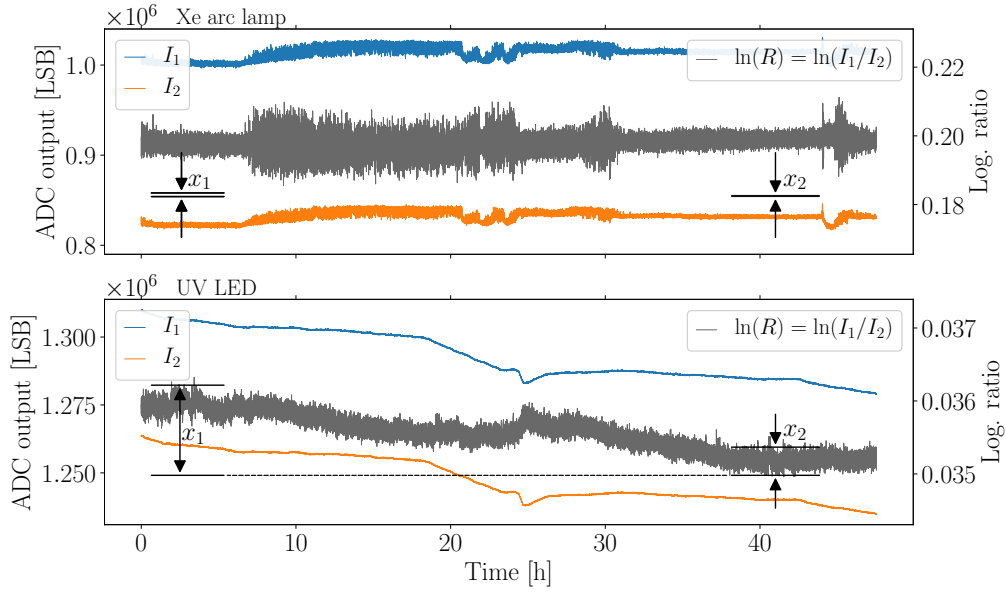


Figure 5.4: Long-term detection of drift and rapid temporal fluctuations of the emitted intensity of a Xe arc lamp (**upper panel**) and a UV LED (**lower panel**). The recorded intensities (left axis) for position 1 (setting A) I_1 (blue) and position 2 (setting B) I_2 (orange) and the calculated log. ratio $\ln(R) = \ln(I_1/I_2)$ (grey, right axis) over time. The Xe lamp does not show a long term drift but temporal rapid variations up to 1% of $\ln(R)$. The UV LED measurement exhibits a relative drift in $\ln(R)$ of $x_1 \approx 1.3 \times 10^{-3}$ and rapid temporal variations $x_2 \approx \pm 0.2 \times 10^{-3}$. The drift x_1 and fluctuations x_2 of the LED are drawn to scale into the Xe lamp panel.

cancel out electronic drift. This ratio is used to determine the strength of intensity fluctuation and the presence of long term drift.

The upper panel of Figure 5.4 shows that the logarithmic ratio $\ln(R)$ for the Xe lamp intensities, which does not indicate a directly visible long term drift. However, the log. ratio $\ln(R)$ reveals strong fluctuation between I_1 and I_2 of the order $\pm 0.5\%$ in stable periods (30-40 h) up to $\pm 1\%$ (10-20 h). These fluctuations are most probably due to the operating principle of a Xe arc lamp and the coupling of light into a fibre due to light-arc variations. By applying a voltage on two narrow located electrodes, an ionised Xe light arc is produced. The light emitted by this arc is focused by a lens and coupled into a fibre. The light arc strength and location are not totally stable and result in rapid fluctuations of intensity. Due to that problem, the Xe lamp can not be used for quantitative detection of trace gases, with an instruments measuring the intensity sequentially and where the expected signal lies in the order of 10^{-3} .

In the lower panel of Figure 5.4, the logarithmic ratio $\ln(R)$ for the UV LED is shown. The LED reveals a clearly visible long term drift over the period of measurements. However, the relative drift in $\ln(R)$ of $x_1 \approx 1.3 \times 10^{-3}$ is smaller than the overall variations in $\ln(R)$ for the Xe lamp. For a better comparison, the drift x_1 is drawn to scale in the upper (Xe lamp) panel. The rapid temporal variations of the logarithmic

ratio correspond to $x_2 \approx \pm 0.2 \times 10^{-3}$ peak to peak, which is also drawn to scale into the upper panel for comparison.

The UV LED is, therefore, a much more suitable light source for laboratory measurements, which allows quantifying signals within the sub 10^{-3} regime. Additionally, the UV LED output intensities can be further stabilised by stabilising the LED temperature (Sihler et al., 2009).

5.4 Trace gas detection with the OP FPI

In a case study performed by Kuhn et al. (2019), the feasibility of the OP FPI on SO_2 is examined. This study investigates the extension of the application to volcanic BrO . BrO is a reactive bromine radical, which furthermore is able to undergo a self reaction. Hence, it is not easy to fill appropriate amounts of BrO into gas cells for laboratory measurements. However, as shown in the model study (Chapter 3 and Figure 3.3, middle panel) the spectral similarity to HCHO can be exploited. As HCHO does not have a self reaction, it can be kept in gas cells at sufficient stable concentration levels, facilitating laboratory experiments.

5.4.1 Preparation and experimental handling of HCHO gas cells

The HCHO gas cell used in the experiments was prepared in the laboratory. Paraformaldehyde (PFA), which is a white crystalline powder, was used as a source. The PFA was filled into a heatable glass container. Further, the container and a fused silica gas cell (cuvette) are connected to an evacuated cell filling system. By warming the PFA with a heat gun above 130°C the powder starts evaporating and gaseous HCHO is flooding the system. After cooling down the HCHO gas polymerizes on the surfaces back into PFA if the saturation vapour pressure (1.93 hPa at 25°C) is exceeded. This deposition of PFA onto the gas cell surfaces can be seen in Figure 5.5, left panel.



Figure 5.5: HCHO gas cell. **left:** Gas cell in thermal equilibrium with ambient air. HCHO condensed as PFA onto the surfaces. **right:** Cell directly after reheating. The solid HCHO is vaporized and will slowly condense back as the temperature decreases.

As the gas cell is in thermal equilibrium the measurable amount of gaseous HCHO is dependent on the saturation vapour pressure of PFA. Starting from universal gas law the volumetric number density ρ can be determined as follows

$$p \cdot V = n \cdot R \cdot T \Rightarrow \rho = \frac{p}{R \cdot T} \quad (5.2)$$

with pressure p , the gas constant R and the absolute temperature T . The particle density ρ_{molec} can be calculated by multiplying $\rho_{molec} = \rho \cdot N_A$. Applying a further multiplication of ρ_{molec} by the length of the used gas cell $x_{cell} = 1 \text{ cm}$, the column density S of gaseous HCHO in thermal equilibrium can be estimated for a given HCHO saturation vapour pressure of $p_{sat} = 1.93 \text{ hPa}$ at $T = 298 \text{ K}$ as

$$S = \rho_{molec} \cdot x_{cell} = 4.7 \times 10^{16} \text{ molec/cm}^2. \quad (5.3)$$

Further, the gas cell can be reheated above 130°C inducing a re-evaporation of the solid PFA into the gaseous phase (see Figure 5.5, right panel). The increase in temperature will again initiate the process of an increase of the HCHO S inside the cell followed by an decrease in S as the gas cell is equilibrating its temperature to the ambient temperature. By non-uniform heating of the cell, blurring of the cell surfaces within the measurement light path can be reduced.

5.4.2 Experimental setup

The experimental setup of gas cell measurements is shown in 5.6. A parallelised light beam is traversing the gas cell before being coupled into a fused silica fibre transmitting the light to the entrance of the OP FPI. To obtain a beam of light more realistic to atmospheric measurement conditions (isotropic and non-parallelised), a third lens is employed. The lens 3 and fibre output are in an out-of-focus position to generate divergent light entering the OP FPI, as prevalent under atmospheric measurement conditions.

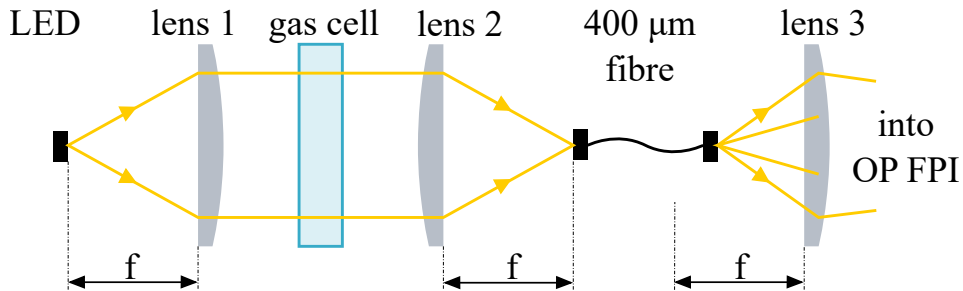


Figure 5.6: Radiation emitted by the UV LED is parallelised before traversing the gas cell. The parallelised light is coupled into a $400 \mu\text{m}$ fused silica fibre. A third lens is used in out-off-focus position to generate atmospheric divergent light before entering the OP FPI.

5.4.3 Interferograms of HCHO

The in Section 5.1 described setup allows for gradually changing the incidence angle of light onto the FPI, thereby gradually tuning its transmission spectrum. The intensities are recorded in each position generating an interferogram. The FPI is tilted in equidistant servo motor positions (smp) steps. The smp are controlled by a pulse width signal given in units of μs . After the final position is reached the scan restarts from the starting point. An interferogram of the UV LED over the possible smp range is shown in Figure 5.7.

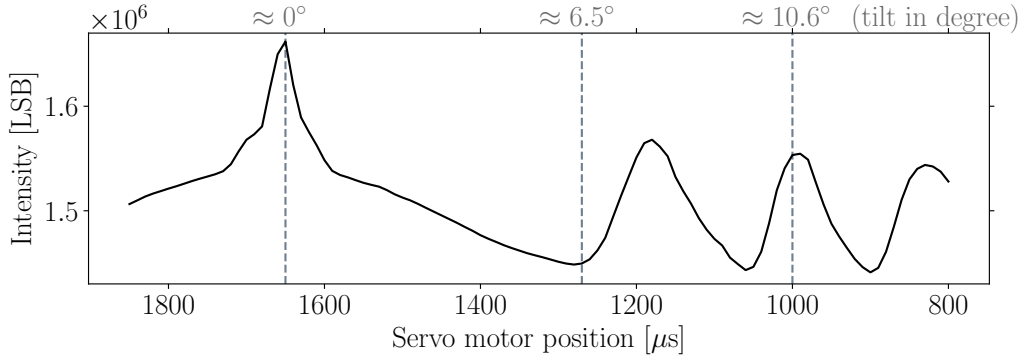


Figure 5.7: UV LED intensity interferogram averaged over ten scans. The FPI is tilted by a servo in equidistant steps of $10\mu\text{s}$. The peak at $1650\mu\text{s}$ indicates the FPI crossing a tilt of 0° . The peak is a result of reflections induced by the optics and the FPI itself. For further decreasing smp the FPI tilt angle increases. Rough FPI tilt angles in degrees are shown in grey (top of figure).

The interferogram is shown as a function of the servo positions as no servo-angular calibration was performed in this setup of the OP FPI (see Figure 5.7). The FPI tilt in units of angular tilt is decreasing from $1850\mu\text{s}$ ($\approx 3^\circ$) to $1650\mu\text{s}$ ($\approx 0^\circ$) before increasing again to $800\mu\text{s}$ ($\approx 15.2^\circ$). The peak at $1650\mu\text{s} \approx 0^\circ$ is a result of internal reflections of the optics and the FPI itself. For small angles, the reflection is hitting photodiode and therefore increasing the detected intensity. For that reasons, measurements with a tilt angle close to 0° or servo position of $1650\mu\text{s}$ are not favourable. By further decreasing the position from $1650\mu\text{s}$, the angular tilt is increasing again.

The wave-like pattern for smp $< 1300\mu\text{s}$ is induced by the tuning the FPI transmission spectrum yielding a shift in the FPI transmission maxima. The spectral range of radiation impinging on the photodiode exhibits sharp edges as it is defined by a product of the LED spectrum and the band pass filter. Due to the tuning of the FPI transmission spectrum, there will be settings where the maxima are located in positions yielding a higher light throughput than in other positions. Each peak in the interferogram, therefore, represents a shift of the FPI spectrum by approximately one spectral order.

The interferograms are now recorded with the HCHO gas cell in the light path. The cell was heated before being placed in the experimental setup as described in the former section. Due to the prior heating of the gas cell, it is cooling down whilst placed

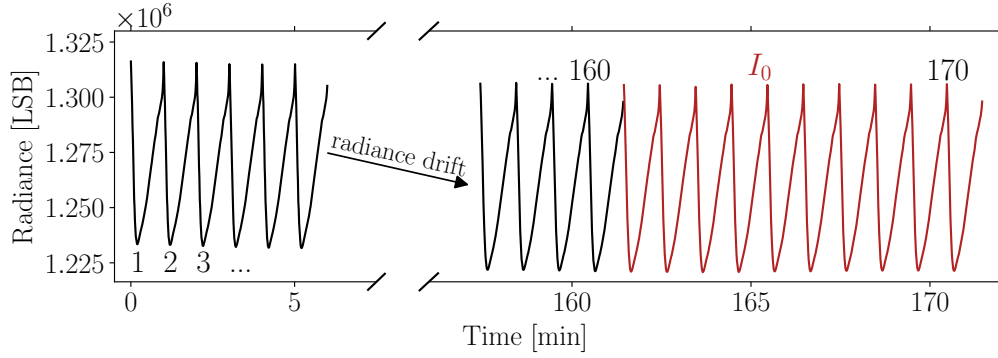


Figure 5.8: 170 interferograms of a previously heated HCHO gas cell. The time for each scan is ≈ 1 min. The overall drift in radiance is due to the condensation of HCHO onto the gas cell surfaces reducing the light transmittance. An average over the last ten scans is used as reference radiation I_0 for the calculation of the optical density since it is expected to correspond to the lowest HCHO concentration in the cell.

in the setup. Therefore, a decreasing signal in the optical density τ is expected. In total, 170 scans were performed, ranging from the smp of $1595 \mu\text{s}$ to $1270 \mu\text{s}$, which roughly corresponds to an angular range of 0.5° to 6.5° . The step resolution is $5 \mu\text{s}$ ($\approx 0.1^\circ$) and in each position 3 radiance readouts are averaged. The time required for one scan is ≈ 1 min.

The recorded time series over 170 scans is shown in Figure 5.8. It is now possible to determine the optical density according to Equation 3.4. For each scan i with $\{i \in \mathbb{N} | 0 \leq i \leq 170\}$ the optical density $\tau'_i(\text{smp})$ is calculated for each smp. As background radiance $I_0(\text{smp})$ the arithmetic mean over the last ten scans, is used (see Figure 5.8, red line). Over the last ten scans the cell is assumed to be in a state of thermal equilibrium yielding a minimum concentration of gaseous HCHO. The optical density $\tau'_i(\text{smp})$ is given by

$$\tau'_i(\text{smp}) = -\ln\left(\frac{I_i(\text{smp})}{I_0(\text{smp})}\right) \quad \text{with} \quad I_0(\text{smp}) = \frac{1}{n-i} \sum_{i=161}^{n=170} I_i(\text{smp}) \quad (5.4)$$

The mean drift of the scan's intensity, visible in Figure 5.8, is induced most probable by the condensation of HCHO onto the gas cell surfaces yielding a reduced transmittance of the cell. Average intensity drifts are here removed by subtracting the mean over the smp of each scan $\overline{\tau_i(\text{smp})} = \overline{\tau}_i$. This yields an optical density $\tau_i(\text{smp})$ relative to $I_0(\text{smp})$ as

$$\tau_i(\text{smp}) = \tau'_i(\text{smp}) - \overline{\tau}_i. \quad (5.5)$$

The $\tau_i(\text{smp})$ for the 170 scans are shown in Figure 5.9. The starting time of each scan is colour coded and is going from blue to red (0 to 170 mins). The attenuation of the maximum and minimum over time towards a zero line indicates the reduction of gaseous HCHO due to the transition into the solid phase. The negative values of τ_i are due to the correction of the drift by the mean value $\overline{\tau}_i$ of each scan. The data shown in

5 The one-pixel FPI instrument

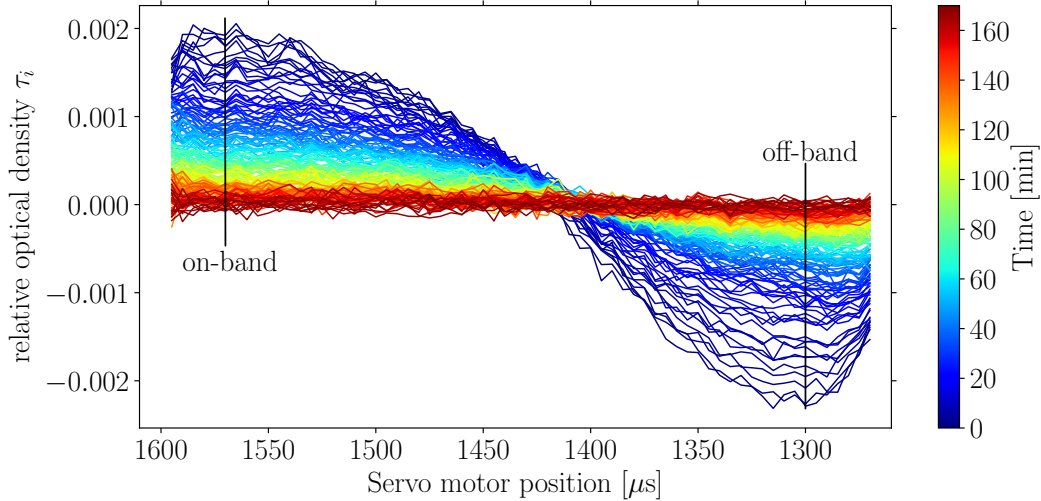


Figure 5.9: Optical density τ_i interferograms. The starting time of the scans is colour coded, starting from blue to red. The loss of gaseous HCHO due to the transition into PFA can be seen by the flattening of the maximum and minimum over time. The maximum corresponds to an on-band position at $1570\mu\text{s} \hat{=} 1.10^\circ$ and the minimum corresponds to an off-band position $1300\mu\text{s} \hat{=} 6.10^\circ$ of HCHO. Negative values for τ_i are due to the normalisation.

Figure 5.9, further allow to determine an on-band and off-band position for an HCHO measurement. The on-band position (maximum τ_i) is located at smp of $1570\mu\text{s}$ and the off-band position (minimum τ_i) at $1300\mu\text{s}$. A coarse angle calibration yielded that the covered smp range from $1595 - 1270\mu\text{s}$ corresponds to $0.5^\circ - 6.5^\circ$ tilt angle inside the FPI etalon. A comparison with the model study of HCHO (see Section 3.2.3) yields that the on-band $1570\mu\text{s}$ and off-band position $1300\mu\text{s}$ correspond to a FPI tilt of 1.10° and 6.10° respectively. These positions are used in the following section for two-position measurements.

5.4.4 Two FPI-position measurements of HCHO

During the two-position measurement, the FPI is toggled between the on-band and off-band position. This reduces the spectral information recorded but increases the temporal resolution to $\approx 1.3\text{s}$. The used positions are determined by the recorded interferograms of an HCHO cell (see former section). The on-band position is located at an smp of $1570\mu\text{s}$, and the off-band position is located at smp of $1300\mu\text{s}$. In each position, five radiance readouts are averaged in the following.

The two-position measurement of an HCHO gas cell over 110 minutes is shown in Figure 5.10. The measurement is divided into two parts. During the initial phase (0-25 min), the gas cell was not heated so that the minimum (thermal equilibrium) HCHO gas concentration could be recorded. In the second phase (25-110 min), the gas cell was reheated once before placing it into the experimental setup. The apparent

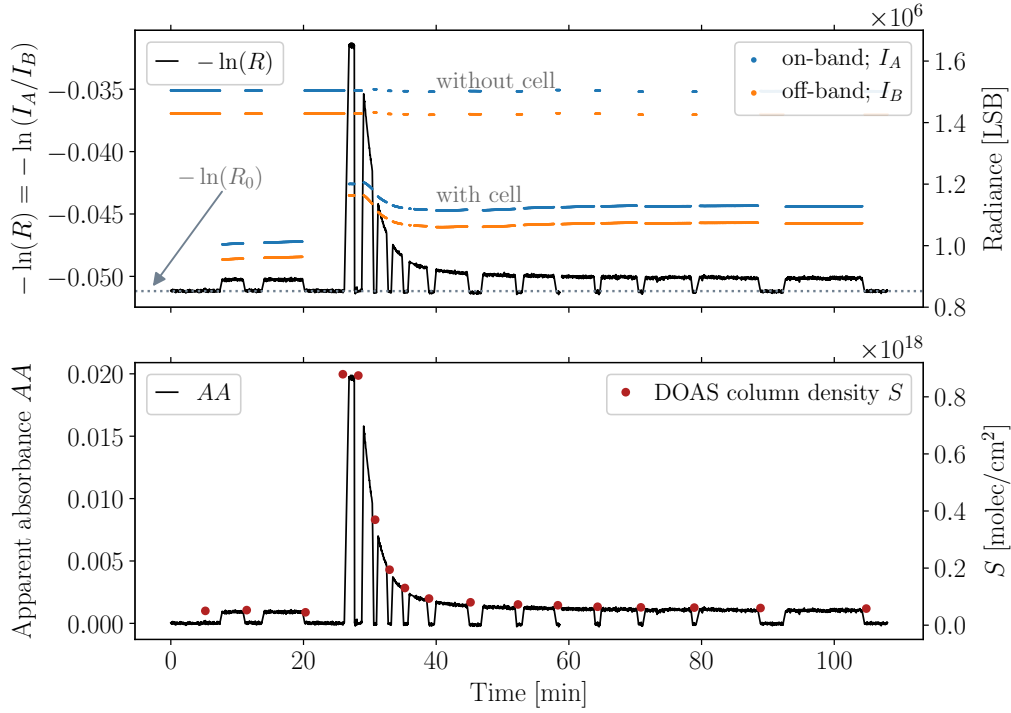


Figure 5.10: Two-position measurement of an HCHO gas cell. The gas cell is measured unheated in the initial phase (0-25 minutes). The previously heated cell was measured in the second phase (25-110 minutes). **Top panel:** The radiances in on-band (I_A , blue) and off-band (I_B , orange) positions are plotted. The jumps in intensity are due to removing the gas cell (with polymerised paraformaldehyde on the cell walls) from the setup, to determine the column density by DOAS measurements. The negative logarithm of the radiance ratio $-\ln(R) = -\ln(I_A/I_B)$ is shown in black. The ratio of the background signal $-\ln(R_0)$ and its potential drift are determined by the baseline (dotted grey). **Bottom panel:** The calculated apparent absorbance AA (black) and the data points of the column density S measured by DOAS (red) are plotted over time.

absorbance AA signal decreases as the HCHO gas concentration is reduced due to temperature equilibration with ambient conditions.

The recorded radiances I_A in on-band and I_B in off-band setting are shown in the top panel of Figure 5.10. The jumps in radiance arise from placing the gas cell in (with cell) and removing the gas cell from (without cell) the experimental setup. During the measurement periods without cell, DOAS measurements of the HCHO column density are performed. To monitor potential drifts in $I_{A,0}$ and $I_{B,0}$ during the measurement these were recorded whilst the cell was outside the setup.

The radiances I'_A and I'_B in on-band and off-band positions are used to determine the apparent absorbance. In a first step, they are corrected for the electronic offset I_D by subtraction giving $I_A = I'_A - I_D$ and $I_B = I'_B - I_D$. Further, the negative logarithm of the radiance ratio is calculated as

$$-\ln(R) = -\ln\left(\frac{I_A}{I_B}\right). \quad (5.6)$$

5 The one-pixel FPI instrument

To obtain the apparent absorbance AA as in Equation 2.13 the quantity $-\ln(R)$ needs to be corrected for the background radiances $I_{A,0} = I'_{A,0} - I_D$ and $I_{B,0} = I'_{B,0} - I_D$

$$\begin{aligned} -\ln(R) + \ln(R_0) &= -\ln\left(\frac{I_A}{I_B}\right) + \ln\left(\frac{I_{A,0}}{I_{B,0}}\right) \\ &= -\ln\left(\frac{I_A}{I_{A,0}}\right) + \ln\left(\frac{I_B}{I_{B,0}}\right) = \tau_A - \tau_B = AA. \end{aligned} \quad (5.7)$$

The resulting AA is plotted together with the column densities S retrieved by DOAS measurements in the lower panel of Figure 5.10. The evaluation of the monitored background signal yields a negligible drift of $\approx 10^{-4}$ over 110 min.

The measured apparent absorbance AA of the OP FPI is plotted as a function of S recorded by DOAS in Figure 5.11 to determine a calibration curve. Applying a linear regression yields a coefficient of determination of $R^2 = 0.99992$.

A verification of the model introduced in Chapter 3 can be performed. The single parameter adapted in the model is the incident radiation which is replaced by a recorded spectrum of the UV LED. The measured sensitivity, represented by the slope in Figure 5.11, is $k_{HCHO,meas} = 2.28 \times 10^{-20} \text{ cm}^2/\text{molec}$. The slope obtained by the model $AA = k_{HCHO,model} \cdot S_{HCHO}$ with $k_{HCHO,model} = 2.25 \times 10^{-20} \text{ cm}^2/\text{molec}$. The deviation between model and measurement is thereby only 1.3% with respect to the measured sensitivity.

Further the detection limit which is valid under laboratory conditions using an UV LED can be estimated. The standard deviation of the apparent absorbance AA over the first 320 data points (\approx seven minutes) accounts for $AA_{min} = 6.2 \times 10^{-5}$. This yields a HCHO detection limit of $S_{HCHO,min} = AA_{min} \cdot k_{HCHO,meas}^{-1} = 2.7 \times 10^{15} \text{ molec}/\text{cm}^2$.

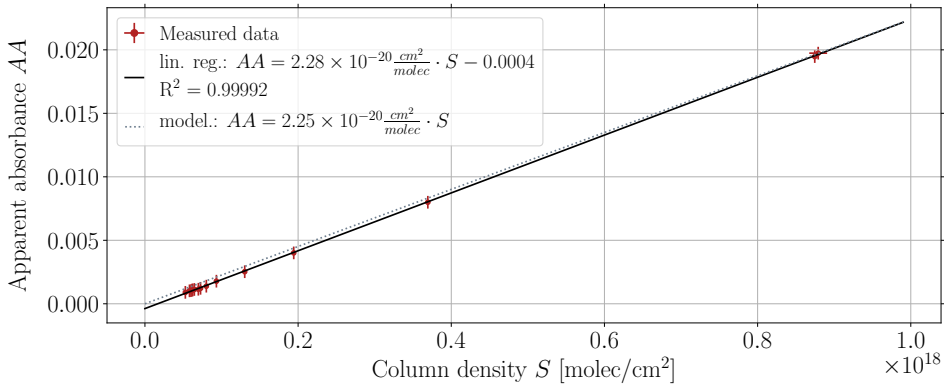


Figure 5.11: Calibration curve for the OP FPI. The column density data S are retrieved by DOAS measurements, and the apparent absorbance AA are determined by the OP FPI. A linear regression is applied yielding a coefficient of determination of $R^2 = 0.99992$ between the OP FPI and DOAS measurements. The sensitivity k accounts for $k = 2.28 \times 10^{-20} \text{ cm}^2/\text{molec}$. Furthermore, a verification of the model is applied where the incident radiation is adapted for the spectrum of the UV LED. The deviation of the modelled slope to the slope of measured data is 1.1%.

As the model and measured data exhibit a good agreement the BrO sensitivity determined by the model in Section 3.2.2 of $k_{BrO,model} = 6.21 \times 10^{-18} \text{ cm}^2/\text{molec}$ is used to estimate a BrO detection limit. This conversion yields a BrO detection limit of $S_{BrO,min} = 10^{13} \text{ molec/cm}^2$ valid under laboratory measurement conditions.

In this chapter, the feasibility of the FPI CS technique for HCHO (BrO) was demonstrated. Lab studies with an artificial light source revealed a high precision, accuracy, and stability ($AA_{min} = 6.2 \times 10^{-5}$) of the OP FPI. Further, the measured data are well represented by the modelled data. This demonstrates that the general assumptions and simplifications applied in the model are sufficient and that the model exhibits an accurate performance.

6 The FPI imaging instrument

The investigations performed in the previous chapter, demonstrate that the concept of FPI CS, as described in Section 2.4 is viable. Based on the successful application of the OP FPI to SO₂ (see Kuhn et al., 2019) and HCHO as a spectral proxy for BrO the FPI CS technique will be extended to imaging applications.

This chapter covers the development and construction of an FPI imaging instrument (FPI camera) with a description of the optical, mechanical, and electronic setup. Furthermore, the first results of field measurements acquired at Mt. Etna, Italy, in July 2019 are presented.

6.1 Optical setup of the FPI camera

The optical setup of the FPI camera is implemented as a 1" telecentric optical system. A schematic is shown in Figure 6.1. The main purpose of the selected optical system is to generate a beam of parallelised light traversing the FPI. Thereby, each pixel sees the same instrument transmission spectrum enabling FPI tuning for all pixels with two tilt settings. Alternatively, the FPI can be used in a divergent beam. The light throughput is then much higher, but the tuning process becomes complicated (see Kuhn, 2015).

Light entering the camera first traverses an iris aperture and is then parallelised by lens 1. Lens 1 is composed of a 1" positive meniscus lens with focal length $f_{pm} = 100$ mm and a 1" plano-convex lens with $f_{pc} = 100$ mm, yielding an effective focal length of $f_1 = (1/f_{pm} + 1/f_{pc})^{-1} \approx 50$ mm. This arrangement reduces spheri-

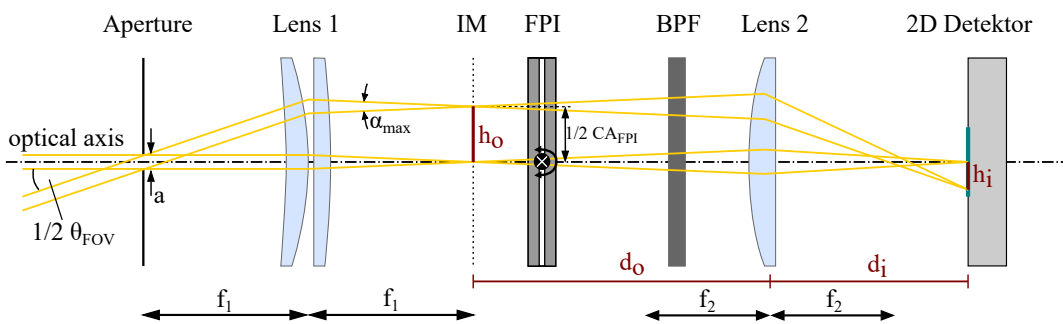


Figure 6.1: Schematic drawing of the telecentric optical system applied in the FPI camera. The lens 1 is used to parallelise the entering light before traversing the FPI and the BPF. Lens 2 projects the parallelised light onto a 2D detector. The divergence of light beams is constrained by the aperture opening diameter of a .

6 The FPI imaging instrument

cal aberration and thereby, decreases the focus spot size. The lens 1 focal length and the FPI clear aperture CA_{FPI} limit the instrumental FOV θ_{FOV} given by

$$\theta_{FOV} = 2 \cdot \arctan\left(\frac{1/2 \cdot CA_{FPI}}{f_1}\right) = 17^\circ \quad (6.1)$$

with the FPI clear aperture of $CA_{FPI} = 15$ mm instead of 20 mm as tilting is reducing the CA_{FPI} . Within the selected telecentric setup and for simplicity of the data evaluation the FPI requires parallelised incident light. However, a complete parallelisation is not achievable due to the finite aperture opening with the diameter a . The upper limit of the divergence of two light beams entering the camera parallel is set to $\alpha_{max} = 1^\circ$. This precondition confines the aperture opening diameter a by

$$\frac{\alpha_{max}}{2} = \arctan\left(\frac{1/2 \cdot a}{f_1}\right) \Leftrightarrow a = 2 \cdot \tan\left(\frac{\alpha_{max}}{2}\right) \cdot f_1 = 0.87 \text{ mm}. \quad (6.2)$$

Lens 2 with a focal length of $f_2 = 50$ mm projects the parallelised light onto a 2D detector.

The beam divergence is generating an intermediate image IM (see Figure 6.1). To render a sharp image on the detector it is beneficial to treat the IM as the object that will be mapped onto the detector. The size of the IM (object, o) is fixed to $h_o = 1/2 CA_{FPI}$. Lens 2 further determines the magnification of the IM and therefore the size of the image h_i projected on the detector according to

$$\frac{h_i}{h_o} = \frac{d_i}{d_o} = \frac{d_i - f_2}{f_2} \Leftrightarrow h_i = h_o \cdot \frac{d_i}{d_o} = h_o \cdot \frac{d_i - f_2}{f_2}. \quad (6.3)$$

with the the object distance d_o and image distance d_i . The positioning of lens 2 and the detector have to follow the proportions induced by Equation 6.3.

Due to the possibility to selected the image size h_i projected on the detector it is possible to decrease the image dimensions smaller than the detector dimension. This will cause a reduction of spatial resolution but increases the radiation per pixel as more light impinges onto a smaller detector area. This additional feature can be applied in conditions with low radiances.

Additionally to the optical system shown in Figure 6.1, a co-aligned DOAS setup is mounted within the FPI camera. The DOAS setup FOV is located within the imaging setup FOV and therefore allows to validate the calibration of the camera (see Section 2.4.2 and Lübcke et al. (2013)). The DOAS optics will be connected to an external spectrograph by a fused silica fibre.

The optic and optomechanic parts are provided by *Thorlabs*. All parts except for the FPI are assembled by a cage system for high solidity, alignment accuracy, and modularity of the optical system. The optomechanics facilitate an easy replacement and adjustment of the optical components. The FPI is placed in an aluminium housing manufactured by the IUP workshop. The housing is fixed on the axis of a stepper motor via a 1/9 transition gear.

6.2 The imaging detector

The detector used in the instrument is the camera SCM2020-UV provided by *EHD imaging GmbH* (see Figure 6.2, left panel). The SCM2020-UV is a UV enhanced camera with a USB3.0 connection for high data transfer rates. The detector's peak quantum efficiency is 94% at 550 nm. In the investigated spectral range from 300-350 nm the quantum efficiency is 33% to 40% (see Figure 6.2, right panel). The camera is using a UV sensitive 1.2" sensor, the GSENSE2020-BSI produced by *Gpixel Inc.*. The GSENSE2020-BSI is a back-illuminated scientific sCMOS image sensor with a resolution of 4 MP. The image data output depth can be set to 11-bit or 12-bit. The camera and sensor key specifications are listed in Table 6.1.

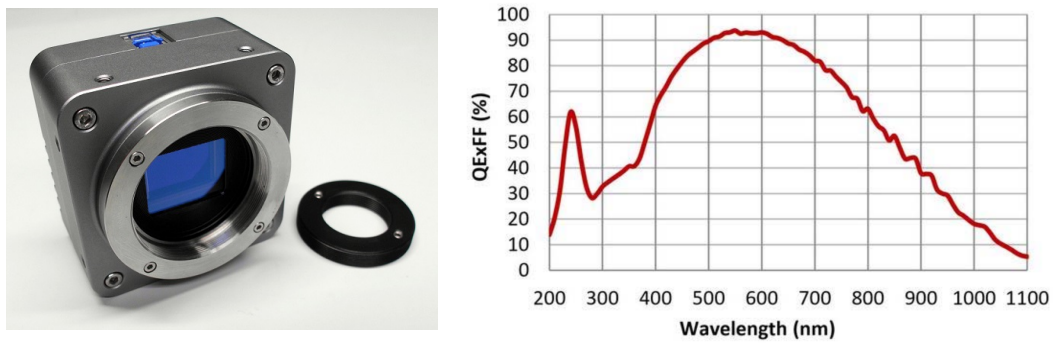


Figure 6.2: Left: Image of the 2D UV detector SCM2020-UV employed in the FPI camera supplied by *EHD imaging GmbH*. Right: Quantum efficiency of the SCM2020-UV with 33% to 40% in the spectral range from 300 - 350 nm. Images from *EHD imaging GmbH*.

Table 6.1: Specifications of the SCM2020-UV camera (values at room temperature; 25°C) at high gain setting for image acquisition.

Parameter	low gain image	high gain image
Sensor size [mm]	13.3 × 13.3	
Pixel size [μm]	6.5 × 6.5	
Resolution (H×V)	2048 × 2046	
Amplifier gain	×1.5	×10.5
conversion factor [LSB/e ⁻]	0.0718	2.2
Full well depth [ke ⁻]	54	1.8
Dark current [e ⁻ /s/pix]	not specified	25
Read out noise [e ⁻]	23	1.6
Exposure time [s]	10 ⁻⁴ – 1000	
Max. frame rate [fps]	45	
Power supply	5 V DC via USB3.0	
Dimensions (W×H×D) [mm]	68 × 68 × 43.4	

6 The FPI imaging instrument

According to Kuhn et al. (2019), the number of counted photoelectrons per pixel and image $N_{\text{phe/pix}}$ with an uncertainty (shot noise) $\Delta N_{\text{phe/pix}}$ can be determined by

$$N_{\text{phe/pix}} = I E_{\text{pix}} \eta \Delta t \quad \Delta N_{\text{phe/pix}} = \sqrt{N_{\text{phe/pix}}} \quad (6.4)$$

with the detected radiances I including the FPI transmission in on-band position and the BPF transmission, the etendue per pixel E_{pix} , the exposure time Δt and the loss factor η combining the detector quantum efficiency and losses within the optics. The etendue per pixel is calculated by

$$E_{\text{pix}} = A_{\text{pix}} \Omega_{\text{pix}} \approx \frac{a^2}{4} \pi^2 \sin^2 \left(\frac{\Theta_{\text{FOV}}}{2 \cdot n_{\text{pix}}} \right) \approx 3.43 \times 10^{-5} \quad (\text{SO}_2) \quad (6.5)$$

$$\approx 8.57 \times 10^{-6} \quad (\text{BrO})$$

with the aperture opening diameter a , the instrumental FOV Θ_{FOV} , and the number of pixel n_{pix} along a column of a square detector. Using the variables and parameters shown in Table 6.2 and inserting them in Equation 6.4 the photon can be calculated yielding, $\Delta N_{\text{phe/pix,SO}_2} = 175$ and $\Delta N_{\text{phe/pix,BrO}} = 503$ (adapted from Kuhn et al. (2019)). As the dark current noise $\Delta DC_{\text{max}} = 25$, the readout noise $\Delta RO_{\text{max}} = 1.6$ and shot noise $\Delta N_{\text{phe/pix}}$ are independent they sum up by the root sum of squares as

$$\Delta = \sqrt{\Delta DC_{\text{max}}^2 + \Delta RO_{\text{max}}^2 + N_{\text{phe/pix}}^2}$$

$$= \sqrt{25^2 + 1.6^2 + 175^2} = 177 \approx \Delta N_{\text{phe/pix,SO}_2} \quad \text{for SO}_2 \quad (6.6)$$

$$= \sqrt{25^2 + 1.6^2 + 503^2} = 504 \approx \Delta N_{\text{phe/pix,BrO}} \quad \text{for BrO.}$$

This shows that the photon shot noise dominates FPI camera noise.

Table 6.2: FPI camera parameters and variables required for the shot noise calculation. Radiances I adapted from Kuhn et al. (2019).

	SO ₂	BrO	
a [mm]		1.7	aperture diameter
n_{pix} (binning)	512 (4)	1024 (2)	pixel along a column
θ_{FOV} [°]		17	FOV
E_{pix} [mm ² sr]	3.43×10^{-5}	8.57×10^{-6}	etendue per pixel
I [photons/(s mm ² sr)]	4.51×10^9	1.48×10^{11}	radiance
η		0.2	loss factor
Δt [s]		1	exposure time

6.3 The stepper motor

The stepper motor applied in the FPI camera is a standard motor with dimensions $42 \times 42 \times 33.5$ mm. The motor ST4209S1006-A is equipped with a precision planetary

gear GPLE22-2S-9, both provided by *Nanotec Electronic GmbH & Co. KG* (see Figure 6.3, left). The stepper motor itself has a step resolution of 0.9° per full step. The planetary gearbox with a reduction rate of $1/9$ decreases the step resolution to 0.1° per full step. The applied planetary gear will cause a backlash of $\approx 0.92^\circ$ which can be prevented by a spring applying torque onto the stepper motor axis.

The stepper motor is controlled by the Envimes SMC v1.0 controller board designed by *Airyx GmbH* (see Figure 6.3, right). The stepper motor control board (SMC) is based on the micro stepping stepper motor controller TMC222 of *TRINAMIC Motion Control GmbH & Co. KG*. The SMC enables to operate the stepper motor in a μ -stepping mode improving the step resolution by a factor up to 16. This yields the final step resolution of $6.25^\circ \times 10^{-3}$ per μ -step or 57600 steps needed for a full axial revolution. The stepper motor is provided without a position encoder and therefore requires an additional end switch. The optical end switch, used is a photoelectric sensor the PM-L-25 by *Panasonic*. The status query of the end switch is executed by the SMC.

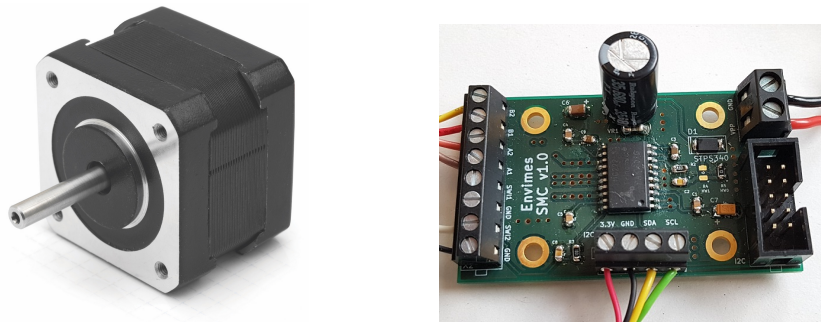


Figure 6.3: Left: Image of the stepper motor ST4209S1006-A (without planetary gear box) provided by *Nanotec Electronic GmbH & CO. KG* (Taken from Nanotec). Right: Image of the Envimes SMC v1.0 stepper motor controller board designed by *Airyx GmbH*.

6.4 Electronic setup

The detector described in Section 6.2 is powered by a USB3.0 connection and controlled by an image analysing software (EHDView V4.7.14294 provided by *EHD imaging GmbH*).

An *Arduino* masters the stepper by a microcontroller board via I²C bus connection with the SMC. A 12V battery powers the stepper motor.

A combined temperature, pressure, and humidity sensor (based on the *BME280*) is placed additionally inside the FPI camera, which enables to record the ambient conditions. The sensor is powered and read out by the *Arduino* using an I²C bus connection.

The software is based on libraries provided by the manufactures and is able to send and receive data via serial communication to a computer.

6.5 The complete FPI-camera setup

The combined FPI camera setup is shown in Figure 6.4. The housing is a dustproof and waterproof polycarbonate box with dimensions $200 \times 300 \times 130$ mm and a total weight of ≈ 4.8 kg. The *Thorlabs* cage system (steel rods) is connecting all optical elements ensuring a correct and stable alignment. In Table 6.3 the used parts are listed.

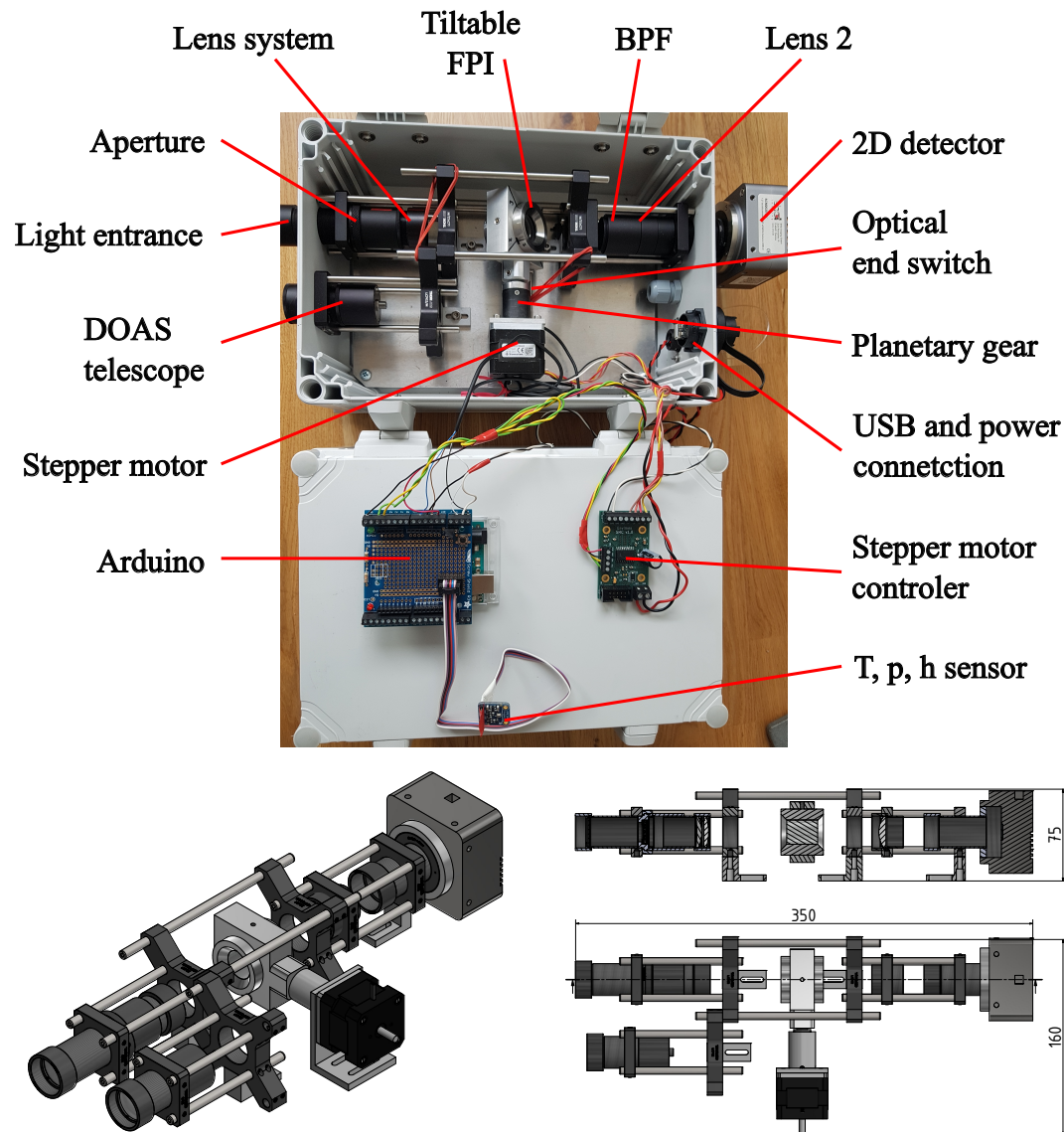


Figure 6.4: **Top:** Image of the complete setup of the FPI imaging instrument including optics, optomechanics, electronics, detector and housing. **Bottom, left:** CAD drawing of the FPI optical setup in 3D projection. **Bottom, right:** CAD drawing in top view of the FPI optics, with a cut (dashed line) through the imaging optics, and the dimensions [mm].

Table 6.3: Part list of the FPI imaging instrument; all prices in Euro, without taxes.

component	supplier	specification	price	comment
optics				
SO ₂ FPI	<i>SLS optics</i>	A20 FIX B	≈ 4400	
BrO FPI	<i>SLS optics</i>	A1001.1	≈ 3130	
2D detector	<i>EHD</i>	SCM2020UV	5100.00	
fused silica lens	<i>Thorlabs</i>	LA4148-UV	111.73	1" plano convex
fused silica lens	<i>Thorlabs</i>	LA4380-UV	101.23	1" plano convex
fused silica lens	<i>Thorlabs</i>	LB4096-UV	106.96	1" bi convex
fused silica lens	<i>Thorlabs</i>	LE4173-UV	101.23	1" pos. menisc.
UV window	<i>Thorlabs</i>	WG41010-UV	97.41	
filter BrO	<i>Edmund</i>	65-129	199.00	(340 ± 5) nm
filter SO ₂	<i>bk</i>	bk-280-310-S	299.00	(310 ± 5) nm
aperture	<i>Thorlabs</i>	SM1D12D	62.79	
cage system	<i>Thorlabs</i>	various	≈ 400	various parts
mechanics				
stepper motor	<i>Nanotec</i>	ST4209S1006-A	}231.50	incl. assembly
planetary gear	<i>Nanotec</i>	GPLE22-2S-9		
mounting plate	<i>IUP</i>	self-built		aluminium
optics mount	<i>IUP</i>	self-built		×5, aluminium
stepper mount	<i>IUP</i>	self-built		aluminium
FPI mount	<i>IUP</i>	self-built		aluminium
housing	<i>Ensto</i>	WPCP203013G	67.80	polycarbonate
electronics				
microcontroller	<i>Arduino</i>	Arduino UNO	17.18	
screw shield	<i>Adafruit</i>	196	13.32	for Arduino
T,p,h sensor	<i>Adafruit</i>	26523	17.78	breakout board
end switch	<i>Panasonic</i>	PM-L25	8.08	optical
power connector	<i>Hirschmann</i>	CA 3 GS	6.18	with dust cap
USB connector	<i>Bulgin</i>	Px0842/B	14.38	with dust cap

6.6 Calibration of the stepper motor position

The inclination of the FPI inside the parallelised light path is specified in rotation steps of the stepper motor position (smp). To determine the incidence angle α of the radiance onto the FPI etalon, a calibration is required.

To investigate the angle of incidence α - smp relation the UV sensitive 2D detector is replaced by a spectrograph, analogous to the measurement setup used to characterise the FPI in Chapter 4. The FPI is mounted with a correct rotational alignment of the wedge angles (see Section 4.1). The zero point for the rotation (smp = 0 = SWP + 510 μ -steps; with the end-switch position SWP) is used according to the results of Section 4.2 for the SO₂ FPI.

The FPI is rotated from $\{-2000 \mu\text{-steps}, 2000 \mu\text{-steps}\}$ with steps sizes of 200 μ -steps. In each rotation position, the FPI transmission spectrum is recorded. The spectra are compared with modelled transmission spectra (analogous to the determination of the plate separation in Section 4.3). The incidence angle α in the model is varied until the modelled and recorded transmission spectrum best fit. The measurement results are shown in Figure 6.5.

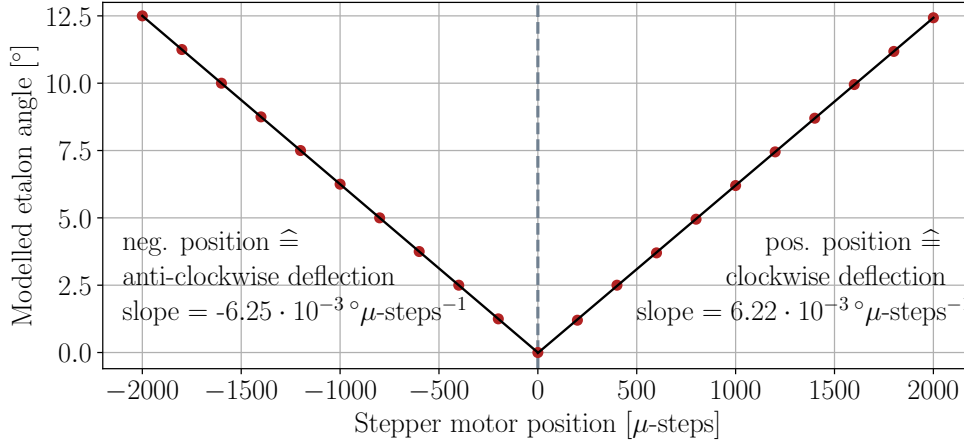


Figure 6.5: Tilt angle-stepper motor position calibration. A linear regression for positive and negative smp yields the conversion factor of smp into angle of incidence. The theoretical value expected is $6.25^{\circ} \times 10^{-3}$.

A linear regression is used to evaluate the angle-smp calibration. For negative smp corresponding to a anti-clockwise deflection of the FPI optical axis to the zero position the regression yields

$$\alpha_{neg} = 6.25 \times 10^{-3} \text{ }^{\circ} \mu\text{-steps}^{-1} \cdot \text{smp} \quad (6.7)$$

with an coefficient of determination $R^2 = 1$. For positive smp the regression yields

$$\alpha_{pos} = 6.22 \times 10^{-3} \text{ }^{\circ} \mu\text{-steps}^{-1} \cdot \text{smp} - 1.81^{\circ} \times 10^{-2} \quad (6.8)$$

with $R^2 = 0.99998$. The theoretical conversion factor (full revolution of 360° requires 57600 μ -steps) is given by $\alpha_{theo} = 6.25 \times 10^{-3} \text{ }^{\circ} \mu\text{-steps}^{-1}$.

6.7 SO₂ measurements: Mt. Etna

The first field measurements with the FPI camera prototype were performed at Mt Etna, Italy, from 20 July to 27 July 2019. The measurements were taken at the Osservatorio, Pizzi Deneri (37°45'57.1"N; 15°00'59.5"E), which is located close to the summit area on 2800 m asl.

In this study, the measurements performed on the 22 July 2019 from 09:00 to 10:00 CET will be demonstrated representative for the field campaign. The measurement was performed under clear sky conditions with a wind direction of $\approx 5^\circ$ and a wind speed of ≈ 6 m/s (wind data from EarthNullschool). An image of the weather conditions is shown in Figure 6.6, left panel. The volcanic plume showed slight condensation. The mean solar location during the measurement had a solar azimuth angle of $SAA \approx 95^\circ$ and solar zenith angle of $SZA = 49^\circ$.

The measurement geometry is shown in Figure 6.6, right panel. The viewing direction was $\approx 204^\circ$ (southwest direction) with an elevation angle of $\approx 5^\circ$. The camera FOV was $\theta_{FOV} \approx 17^\circ$ as determined in Equation 6.1. The FOV is partially covering the plume of the southeast crater (SE). Due to the wind conditions the plumes of the northeast (NE) and central craters (CC) intruding the FOV on the right-hand side.

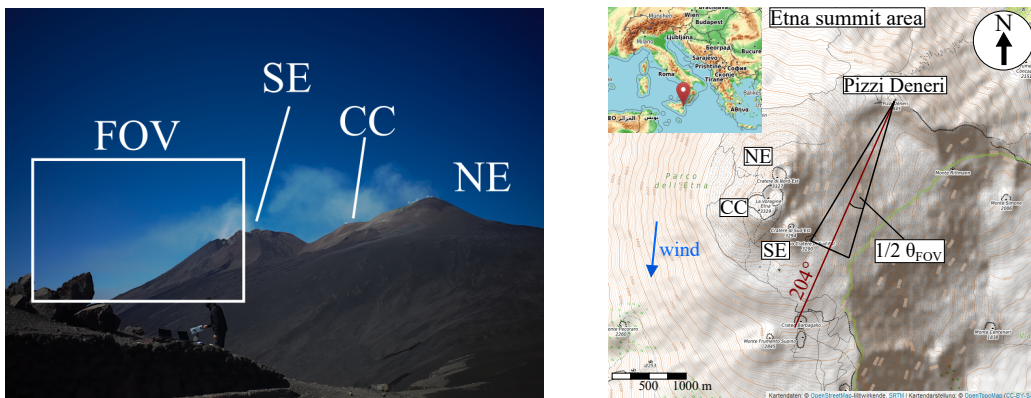


Figure 6.6: **Left:** Image of the measurement conditions on 22 July 2019. The FOV is partly covering the southeast crater (SE) plume. Due to wind conditions, the plumes of the northeast (NE) and central craters (CC) intruding the FOV on the right-hand side. **Right:** Topographic map of the Mt. Etna summit area, including the viewing geometry on 22.07.2019. The red line indicates the central viewing direction of 204° and the blue arrow the wind direction of $\approx 5^\circ$. Base map from OpenTopoMap.

An overall software that is controlling both the detector and stepper motor was not completed for the measurement. Therefore, the acquisition of images and tilting of the FPI was triggered by hand yielding a temporal resolution of ≈ 6 s for one pair of images. The image exposure time was set to 1 s and detector resolution is reduced to 512×512 pixel (4×4 binning) resulting in-half saturation of the detector photon well depth. The FPI tilt in on-band position was set to $8.17^\circ \hat{=} -1307 \mu$ -steps and in off-band position $6.45^\circ \hat{=} -1032 \mu$ -steps.

The measurement procedure started with the acquisition of a dark image I_D containing the instrumental stray light and detectors' electronic offset and dark current. It was determined by the arithmetic mean over ten images acquired under conditions with no light entering the camera setup. The exposure time thereby was set equal to the measurement exposure time (1 s).

In a second step, reference images $I_{A,0}$ and $I_{B,0}$ in a plume free area of the sky were being acquired in on-band (A) and off-band (B) FPI setting respectively. To reduce noise, the arithmetic mean over ten images in each setting was determined. $I_{A,0}$ and $I_{B,0}$ are required to perform a flat-field correction, which is later used to normalise the different integrated spectral radiances of the measurement images I_A and I_B . $I_{A,0}$ and $I_{B,0}$ only contain the radiance conversion factor between the on-band and off-band setting and do not need to represent the background sky conditions as required in the evaluation of SO₂ camera data. The reference images, therefore, only need to be recorded once for the different tilt positions of the FPI either in the laboratory (e.g. with an integrating sphere) or by using a plume free area of the sky like in our measurement.

In a third step, two gas cells with different SO₂ concentrations were placed in front of the cameras' light entrance covering the complete FOV. For each cell the mean over five images was used to determine $I_{A,C}$ and $I_{B,C}$. To enable a column density calibration of the camera a DOAS instrument additionally measures the gas cells.

To perform volcanic plume measurements, the FPI camera FOV was adjusted so that it contains the plume partially. During the measurement, the FPI was toggled between on-band (A) and off-band (B) setting acquiring measurement images I_A and I_B in each setting consecutively.

6.7.1 Calibration of the FPI camera AA

To calibrate the FPI camera, two gas cells with different SO₂ concentrations are used. Both cells were measured with the FPI camera to determine the two different apparent absorbances AA and by a DOAS instrument to evaluate the column density S .

The evaluation of the cell AA is performed pixel-wise. In a first step, it is required to correct for the dark signal by subtracting the dark image I_D from the reference images $I_{A,0}$, $I_{B,0}$, and the cell images $I_{A,C}$, $I_{B,C}$. The further evaluation will be performed analogously to the evaluation done for HCHO in Equation 5.7. The cell AA, therefore, is given by

$$AA = -\ln\left(\frac{I_{A,C} - I_D}{I_{B,C} - I_D}\right) + \ln\left(\frac{I_{A,0} - I_D}{I_{B,0} - I_D}\right) \quad (6.9)$$

Thereby the second term of Equation 6.9 contains the flat-field correction only.

The obtained AA for cell 1 and cell 2 are shown in Figure 6.7. An inhomogeneous AA distribution over the FOV is visible and exhibits a similar trend for both cells. This inhomogeneity is induced by an altered illumination of the FOV due to multiple scattering and reflections on the surfaces of the gas cells (see Lübcke et al., 2013).

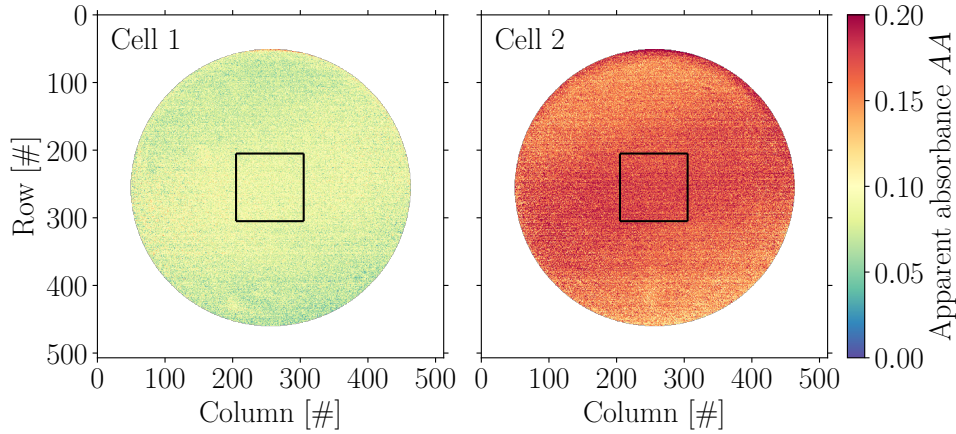


Figure 6.7: SO₂ gas cell AA. The black square centred in the FOV is used to determine the cell's AA arithmetic mean and standard deviation yielding for cell 1: $\overline{AA}_1 = 0.086 \pm 0.013$ and for cell 2: $\overline{AA}_2 = 0.173 \pm 0.018$. The inhomogeneities of the AA visible are induced by multiple scattering on the cell surfaces altering the illumination.

Therefore, the centre area of the FOV (black squares in Figure 6.7) is used to determine the cell's AA. The computation of the arithmetic mean and standard deviation of the squared area yields an apparent absorbance of $\overline{AA}_1 = 0.086 \pm 0.013$ for cell 1 and $\overline{AA}_2 = 0.173 \pm 0.018$ for cell 2. Further, weak horizontal and vertical lines are identifiable in the cell AA images. These are induced by the horizontal banding noise of the CMOS detector. The banding noise is caused by multiple hardware sources e.g., the sensor readout, the amplification, ADC conversion but can be reduced by digital image processing (see Zhang et al., 1999; Kaur and Singh, 2012).

A DOAS measurement determines the cells' column density S . The evaluation requires a reference spectrum of the background sky conditions and a measurement spectrum with the cell placed in front of the DOAS telescope. Further, dark current and offset spectra are acquired to correct the spectrometer dark signal. To evaluate the spectra, the DOASIS software is used. In a simple DOASIS evaluation scenario, the SO₂ absorption cross section is fitted to the obtained spectral optical densities. The spectral fit region for SO₂ is selected according to standard evaluation range of NOVAC (Network for Observation of Volcanic and Atmospheric Change) ranging from 314.8 nm to 326.8 nm (see Lübcke et al., 2014; Warnach et al., 2019). The retrieved column densities are $S_1 = (1.176 \pm 0.048) \times 10^{18}$ molec/cm² for cell 1 and $S_2 = (2.496 \pm 0.074) \times 10^{18}$ molec/cm² for cell 2.

The measured data points are shown in Figure 6.8. Additionally, the modelled calibration function calculated for SO₂ in Section 3.2.1 is plotted (drawn, black). A discrepancy between the modelled and measured sensitivities can be observed. This is a result of the simplified simulation used in this thesis to determine the FPI camera's calibration curve. The incident light onto the FPI is assumed to be non-divergent in the simulation. A more realistic approach is to assume a cone-shaped beam of light (see Kuhn, 2015). The tilting of the FPI then will result in a non-uniform angle of

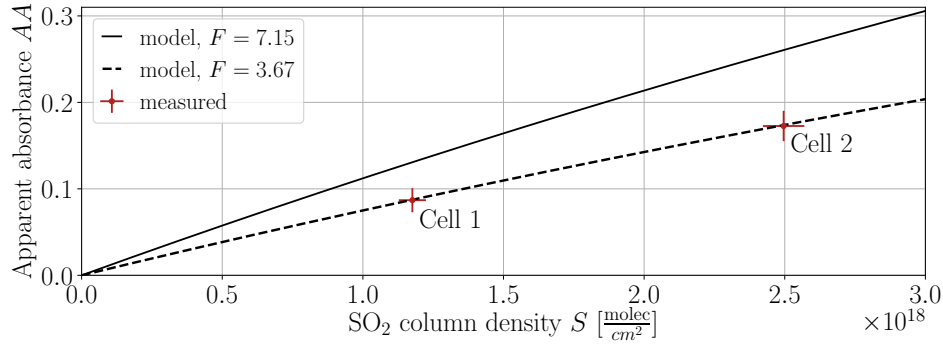


Figure 6.8: Gas cell calibration of the FPI camera. The apparent absorbance AA of the two cells is determined with the FPI camera and the column densities S are retrieved by a DOAS evaluation (red data points). The modelled calibration function with an FPI finesse of $F = 7.15$ according to the simulation used in this thesis (drawn, black) is showing a discrepancy to the measured data. This is a result of simplifications applied in the simulation keeping the effective finesse F constant. By decreasing the effective finesse F (as expected) from 7.15 to 3.67 the modelled calibration function (dashed, black) represents the measured data.

incidence for the radiation impinging onto the FPI. This leads to a decrease in the effective finesse F (see Kuhn, 2015). By adapting the finesse in the simulation from 7.15 to 3.76, the measured calibration function can be well represented by modelled calibration function (dashed black, Figure 6.8). The decrease in finesse leads to a blurring of the FPI transmission peaks. This reduces the correlation (anti-correlation) of the FPI transmission spectrum to the differential absorption structures of SO_2 in on-band (off-band) setting. For now, the finesse is changed to fit the cell measurements. In reality, the effective finesse for setting A and B won't be the same. In future work, a more detailed instrument model will be used to account for beam geometry and to calculate the effective finesse from the optical setup parameters, as done in Kuhn et al. (2019).

The modelled calibration curve (polynomial) with an adapted effective finesse of $F = 3.67$ can now be used to convert measured AA into the column density S distributions. Thereby, it is beneficial to use the simulated calibration curve as the saturation effects for high S are included.

6.7.2 Evaluation of the FPI camera measurement

The evaluation of the FPI camera data requires five images in total. The dark image I_D , two reference images $I_{A,0}$ and $I_{B,0}$ for the flat-field correction, and two measurement images I_A and I_B containing the volcanic plume in on-band (A) and off-band (B) setting respectively. In general, the evaluation of the volcanic plume measurement can be performed analogous to the evaluation of the gas cells in the former section, by replacing $I_{A,C}$, $I_{B,C}$ with I_A , I_B in Equation 6.9. However, to visualize the functional principle of the FPI camera, an intermediate step is performed by cal-

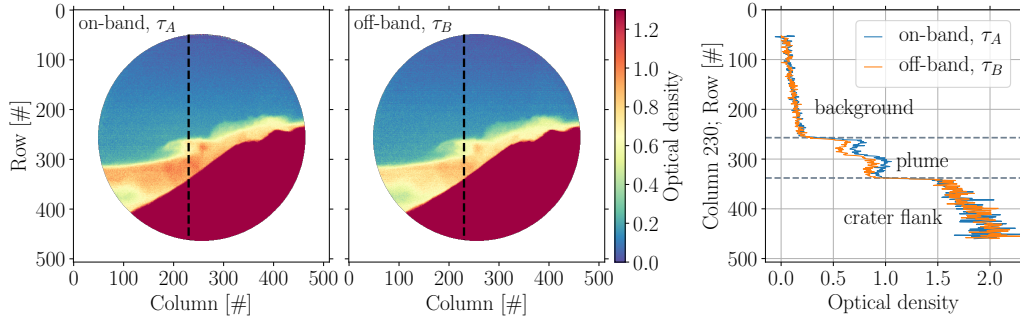


Figure 6.9: Optical density τ_A in on-band position (**left**) and τ_B in off-band position (**middle**) are shown as images with 512×512 pixels. The lower optical density in off-band position is visible. **Right:** τ_A (blue) and τ_B (orange) of column 230 (dashed black, left and middle) are plotted row-wise to emphasize the difference. In the background and crater flank area $\tau_A = \tau_B$, whereas in the plume region $\tau_A > \tau_B$.

culating the optical densities as explained in Sections 2.3.2 and 2.4.2. Rearranging Equation 6.9 as

$$AA = \tau_A - \tau_B = -\ln\left(\frac{I_A - I_D}{I_{A,0} - I_D}\right) + \ln\left(\frac{I_B - I_D}{I_{B,0} - I_D}\right) \quad (6.10)$$

yields the optical densities τ_A and τ_B in on-band and off-band setting of the FPI. In Figure 6.9 the τ_A (left panel) and τ_B (middle panel) are shown for an exemplary set of images. The outer areas are flagged as the circular FPI housing covers them. The employed BPF with a CW of 308 nm induces that the broadband absorption of SO₂ (see Figure 2.4) is visible in both on-band and off-band setting. Nevertheless, the reduction of the optical density in the off-band setting is distinct. To further visualise and emphasise the difference between τ_A and τ_B , the optical densities of the image's column 230 is plotted in Figure 6.9, right panel. In the background and the crater flank area the optical densities are equal $\tau_A = \tau_B$, whereas in the plume area the on-band optical density (blue line in Figure 6.9) is higher than the off-band optical density (orange line in Figure 6.9) $\tau_A > \tau_B$.

The calculated AA is shown in Figure 6.10. To emphasize the magnitude of the AA and its noise an exemplary column (column 230; dashed line, left panel) is displayed in the right panel of 6.10. In both, the image and single column of the AA the background, the plume and crater flank regions are clearly distinguishable. To determine the offset of the background apparent absorbance AA_{BG} the arithmetic mean over a square with 100×100 pixel (see Figure 6.10, left panel) of a plume free region is calculated, yielding $AA_{BG} = 4.3 \times 10^{-3}$. To estimate the detection limit, the standard deviation σ_{AA} is calculated for the same area, yielding $\sigma_{AA} = 2.97 \times 10^{-2}$.

Further, the CMOS sensor horizontal banding noise can be seen as for the cell images in the former section.

The calibration curve determined in Section 6.7.1 can now be used to convert the calculated AA distribution into a column density distribution. The resulting image is

6 The FPI imaging instrument

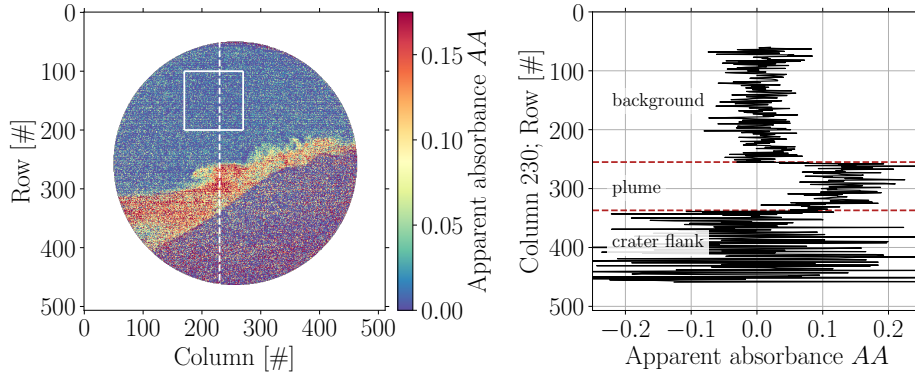


Figure 6.10: The apparent absorbance AA calculated for the optical densities in Figure 6.9. **left:** 512×512 pixel image of the AA distribution. Squared area is used to determine background offset $AA_{BG} = 4.3 \times 10^{-3}$ by averaging and to estimate the detection limit $\sigma_{AA} = 2.97 \times 10^{-2}$ given by the standard deviation. **right:** Column 230 (dashed white in left panel) is separately shown to identify scattering of the determined AA .

shown in Figure 6.11. The background column density offset S_{BG} and detection limit σ_S are now determined in the same plume free area as for the AA in Figure 6.10. This yields $S_{BG} = 6.20 \times 10^{16}$ molec/cm² and $\sigma_S = 3.78 \times 10^{17}$ molec/cm² \sqrt{s} . The detection limit thereby lies in the same order of magnitude compared with other imaging instruments applied for SO₂ (see Kern et al., 2015).

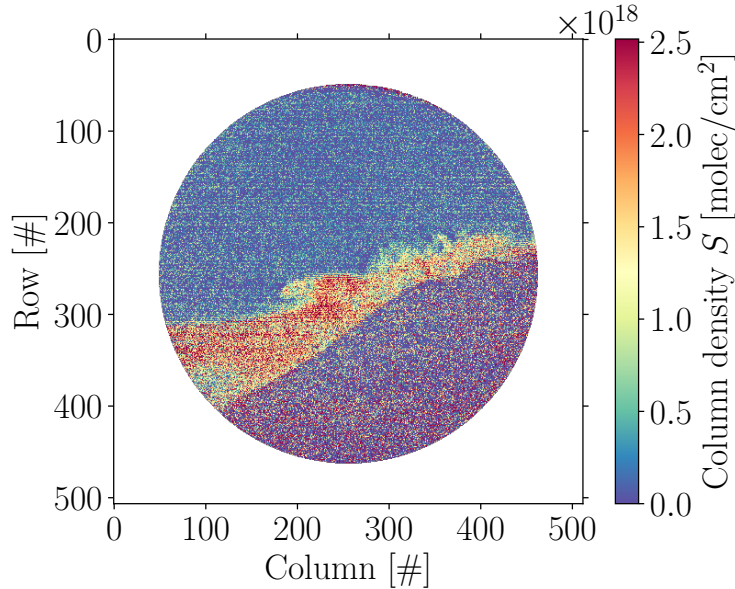


Figure 6.11: SO₂ column density distribution of the volcanic plume of Mt. Etna shown as an images with resolution of 512×512 pixels. For the calibration the simulated calibration function with an adapted FPI finesse of $F = 3.67$ is used (see Figure 6.10, dashed black).

With this data, the plume is visualised on its intrinsic spatio temporal scale. From time series with high time resolution, emission rates can be calculated (see Kern et al., 2015; Gliß et al., 2017). Compared to presently used filter-based systems, the novel technique uses much more detailed spectral information and therefore should yield much better accuracy.

6.7.3 Estimation of SO₂ emission rates

To estimate the SO₂ emission rates (SO₂ fluxes, Φ) an integration of the evaluated SO₂ column density distribution (e.g. in Figure 6.11) along a cross section x through the volcanic plume is required. The integral further needs to be multiplied with the wind speed component v_{\perp} perpendicular to the viewing direction yielding the SO₂ flux through the cross section. The flux Φ given by

$$\Phi = v_{\perp} \cdot \int S_{\text{SO}_2} dx. \quad (6.11)$$

As the SO₂ column density distribution is recorded by an detector with finite pixel size the integral in Equation 6.11 needs to be discretised by sum over the pixel i containing the plume. Equation 6.11 then reads as

$$\Phi = v_{\perp} \cdot \sum_i (S_{\text{SO}_2,i} \cdot \Delta s_i) \quad (6.12)$$

with the height Δs_i of a pixel. Δs_i can be calculated using geometric considerations by

$$\Delta s_i = d \cdot \tan\left(\frac{\theta_{FOV}}{n}\right) \approx 2.7 \text{ m} \quad (6.13)$$

with the number of pixels $n_{pix} \approx 400$ inside the FOV with $\theta_{FOV} \approx 17^\circ$ and the distance $d \approx 3500 \text{ m}$ between the camera and the volcanic plume, see Figure 6.6.

The calculation of Φ for the acquired data is performed exemplarily for the SO₂ column density evaluated in Figure 6.11. The summation in Equation 6.12 is performed for the pixels of column 230 and rows 240 to 340 yielding an average integrated SO₂ concentration of $1.43 \times 10^{20} \text{ molec/cm}$ per pixel. The wind speed perpendicular to the viewing direction can again be determined by geometric consideration. With an viewing direction of $\approx 204^\circ \text{ N}$ and wind direction of 185° N (inclination of 19° between wind and viewing direction), the orthogonal proportion is given by $v_{\perp} = v \cdot \sin(19^\circ) \approx 2 \text{ m/s}$ for a given wind speed of $v \approx 6 \text{ m/s}$. This yields a molecular flux of $\Phi_{molec} \approx 2.86 \times 10^{24} \text{ molec/s}$ which corresponds to a mass flux of $\Phi_{mass} \approx 0.29 \text{ kgSO}_2/\text{s} \hat{=} 25.3 \times 10^3 \text{ kgSO}_2/\text{d}$. These values are only a rough estimation demonstrating the principle of the SO₂ flux determination.

The total SO₂ mass flux of all craters for Mt. Etna is one to two orders of magnitudes higher than the retrieved flux (e.g., Aiuppa et al., 2008; Salerno et al., 2009). In our measurement, the plume of the southeast crater only was examined. Further, significant parts of the plume were covered by the crater flank, which thereby reduces the amount of SO₂ visible for the camera. Under these considerations, the estimated SO₂ flux is reasonable and is compatible with other flux measurements of the southeast crater only (e.g., D'Aleo et al., 2016).

7 Conclusion & outlook

Conclusion

Fabry-Perot interferometer correlation spectroscopy (FPI CS) uses the spectral correlation of the FPI transmission and molecule absorption. This thesis investigates the applicability of FPI CS to atmospheric trace gas remote sensing. In particular, it is shown that FPI CS can be used to largely increase the spatio-temporal resolution of trace gas measurements at point sources like e.g. volcanoes.

To give proof of concept of the FPI CS for BrO, a one-pixel FPI prototype (OP FPI) was used. The OP FPI performance was examined and characterised in laboratory measurements.

As BrO can undergo a self reaction, it can not be trapped in gas cells making laboratory measurements difficult. However, a model study showed, that the operation settings of the OP FPI are almost identical for HCHO and BrO, due to the spectral similarity in the used wavelength range. Therefore, it was possible to exploit HCHO as a proxy for BrO in laboratory measurements.

The same instrument model is used to compare the theoretical with the measured sensitivity of the OP FPI. The model, however, requires precise specifications of the FPIs used in the instrument in order to determine their tuning settings. As the FPIs are custom made and designed as air-spaced etalons with a fixed mirror separation, they need to be thoroughly characterised in the laboratory. A methodology for the characterisation of air-spaced FPIs using a grating spectrograph is proposed in this work.

The obtained sensitivities (weighted mean trace gas absorption cross section) are listed in Table 7.1. The modelled and measured sensitivities of the OP FPI for HCHO are in good agreement showing a deviation of 1.3% only. Further, the conformity of model and measured data allows to state that the instrument model can be used to approximate the OP FPI sensitivity for BrO shown in Table 7.1. The determined sensitivities are comparable to those of DOAS measurements of HCHO and BrO.

After the application of the OP FPI device, an imaging FPI CS prototype (FPI camera) was designed to investigate the behaviour of FPI CS in imaging applications. The prototype FPI camera built is a robust, compact ($200 \times 120 \times 350$ mm) and lightweight (4.8 kg) device and is hence easily portable and applicable for volcanic measurements.

The first imaging measurements based on FPI CS concentrated on the detection of SO₂, as a strong absorption signal is expected under volcanic measurement condi-

7 Conclusion & outlook

tions. This makes it easier to verify the applicability and evaluate the performance of the imaging FPI CS technique.

Field measurements of SO₂ were performed on a campaign at Mt. Etna, Italy. The acquired data showed that the FPI camera can resolve SO₂ trace gas distributions of volcanic plumes with a high spatial resolution. The obtained detection limit of the FPI camera prototype for SO₂ is shown in Table 7.1 and is comparable with other presently applied SO₂ camera systems, but with reduced cross sensitivities to other trace gases and aerosols. Further, the spatial resolution was sufficient to estimate volcanic SO₂ emission rates, which demonstrates the potential for FPI CS to be used as a new volcanic monitoring technique.

A SO₂ cell calibration determined the FPI camera sensitivity. However, the measured sensitivity is 33% lower than the modelled sensitivity displayed in Table 7.1. This deviation is due to the simplifications made in the model, which does not account for the changes in the FPI's effective finesse due to tuning (tilting). The reduction in the effective finesse is resulting in a blurring of the FPI transmission spectrum. This leads to a decreasing sharpness of the FPI's transmission peaks and, therefore, to a reduction in sensitivity. These effects are more pronounced for SO₂ than for BrO and HCHO because the different spectral shapes of the absorption cross section determine the impacts of effective finesse changes.

Table 7.1: Overview of the sensitivities and detection limits obtained by the model and measurements for the different instruments and trace gas species. Sensitivities (weighted mean trace gas absorption cross section) in units of [cm² molec⁻¹]; detection limits in AA and S [molec cm² s^{-1/2}].

instrument	trace gas	model. sensitivity	meas. sensitivity	detec. limit
OP FPI	HCHO	2.25×10^{-20} (1)	2.28×10^{-20}	AA: 6.2×10^{-5} (2) S: 2.7×10^{15} (2)
OP FPI	BrO	6.21×10^{-18}	-	AA: - S: 1×10^{13} (2)
FPI camera	SO ₂	1.18×10^{-19}	0.79×10^{-19}	AA: 2.97×10^{-2} S: 3.78×10^{17}

(1): Light source in model was adapted (high resolution solar spectrum → UV LED spectrum) for laboratory measurements yielding a different HCHO sensitivity than shown in Section 3.2.3.

(2): Values for laboratory studies with UV LED as light source. Detection limits will differ under atmospheric measurement conditions.

Outlook

Within the scope of this thesis, the feasibility of an FPI based remote sensing technique for volcanic trace gases, the FPI CS, was successfully demonstrated. Nonetheless, there are various possibilities to further improve the understanding, performance, and application of FPI CS by continuing the work of this project.

The instrumental model used in this thesis is relying on several simplifications. Modelling divergent light incidence onto the FPI can replace the approach of parallel light rays. Further, the implemented FPI transmission function can be revised by including the influences of FPI wedge angles and a tilt dependent finesse. These improvements should allow the model to adequately calculate the instrument sensitivity from literature absorption cross sections, making in-field calibration redundant.

The most significant uncertainty in the characterisation of the FPI is induced by the low resolution of the applied spectrograph (0.8 nm). The spectrograph was not able to resolve the FPI transmission peaks entirely ($\text{FWHM} \approx 0.3 \text{ nm}$), resulting in a broadening. Hence, a more concise characterisation of the FPI can be achieved by a spectrograph with higher resolution.

The OP FPI prototype can be built more compact and robust. Further, the detection limit can be decreased using a transition for the servo motor to better resolve the FPI tilt angle. After successful applications of the OP FPI on HCHO in the laboratory, the next step could be performing field measurements of HCHO and BrO and investigate cross sensitivities.

The FPI camera in present state is only an early-stage prototype. The first crucial improvement is to increase the camera time resolution by programming a measurement software. This would further allow to utilise a co-aligned DOAS instrument to validate the modelled calibration function.

The evaluation of data recorded at Mt. Etna can be further advanced by including digital image processing approaches, e.g., edge detection to precisely overlay the images and median filters to reduce banding noise.

Additionally, the light throughput can be enhanced by replacing the used band pass filter with $\approx 60\%$ peak transmission by new recently available filters with a peak transmission of $\approx 80\%$. Furthermore, a UV detector with higher quantum yield could be employed (60% instead of 30%) in the used wavelength range. Both improvements can decrease the camera's noise and increase the spatio-temporal resolution.

Careful characterisation and investigation of cross sensitivities shows that, the FPI camera can be applied for imaging of BrO distributions in volcanic plumes. Observed BrO gradients most probably give valuable insights into recent questions of atmospheric halogen chemistry.

Finally, the FPI CS technique can, in principle, be applied for various other trace gases exhibiting periodic differential absorption structures (e.g., OCIO, IO, HCl, NO₂, CO₂, CH₄). Therefore, future studies, including additional species, will reveal a broad field of further applications of FPI CS in atmospheric remote sensing.

A Appendix

A.1 Linearisation of AA_{FPI} for small column densities

This section demonstrates the double linearisation of AA_{FPI} to demonstrate the proportionality of $AA_{FPI} \propto S$ for $\sigma \cdot S \ll 1$.

Starting from Equation 2.24 where AA_{FPI} is given by

$$AA_{FPI} = \tau_{FPI,A} - \tau_{FPI,B}. \quad (\text{A.1})$$

As the subtraction has no influence on the proportionality it is possible to write

$$AA_{FPI} \propto \tau_{FPI,A} \quad (\text{A.2})$$

By including Equation 3.4 for $\tau_{FPI,A}$ one gets:

$$AA_{FPI} \propto -\ln \left(\frac{\int I_0(\lambda) \cdot \exp(-\sigma(\lambda)S) \cdot BPF(\lambda) \cdot T_{FPI}(\lambda; \alpha) d\lambda}{\int I_0(\lambda) \cdot BPF(\lambda) \cdot T_{FPI}(\lambda; \alpha) d\lambda} \right). \quad (\text{A.3})$$

To simplify the equation we define $\Gamma(\lambda) = I_0(\lambda) \cdot BPF(\lambda) \cdot T_{FPI}(\lambda; \alpha)$ including the spectral information except for $\sigma(\lambda)$. Equation A.3 then reads:

$$AA_{FPI} \propto -\ln \left(\frac{\int \Gamma(\lambda) \cdot \exp(-\sigma(\lambda)S) d\lambda}{\int \Gamma(\lambda) d\lambda} \right). \quad (\text{A.4})$$

The first linearisation can be applied for $e^{-x} \approx 1 - x$ for $x \ll 1$ giving $e^{-\sigma(\lambda)S} \approx 1 - \sigma(\lambda)S$. By inserting and rearranging Equation A.4 we get

$$\begin{aligned} AA_{FPI} &\propto -\ln \left(\frac{\int \Gamma(\lambda) d\lambda + \int \Gamma(\lambda) \sigma(\lambda) S d\lambda}{\int \Gamma(\lambda) d\lambda} \right) \\ &= -\ln \left(1 - S \cdot \frac{\int \Gamma(\lambda) \sigma(\lambda) d\lambda}{\int \Gamma(\lambda) d\lambda} \right) \end{aligned} \quad (\text{A.5})$$

By setting $X = [\int \Gamma(\lambda) \sigma(\lambda) d\lambda] / [\int \Gamma(\lambda) d\lambda]$ we get

$$AA_{FPI} \propto -\ln(1 - S \cdot X). \quad (\text{A.6})$$

A second linearisation for $\ln(1 - x) \approx -x$ for $x \ll 1$ can be applied on $-\ln(1 - S \cdot X) \approx S \cdot X$ for $S \cdot X \ll 1$. This finally yields in the stated proportionality of

$$AA_{FPI} \propto S \cdot X \Rightarrow \mathbf{AA}_{FPI} \propto \mathbf{S} \quad (\text{A.7})$$

valid under the assumption $\sigma \cdot S \ll 1$.

A.2 BrO model results for filter with CWL 337 nm, 10 nm FWHM

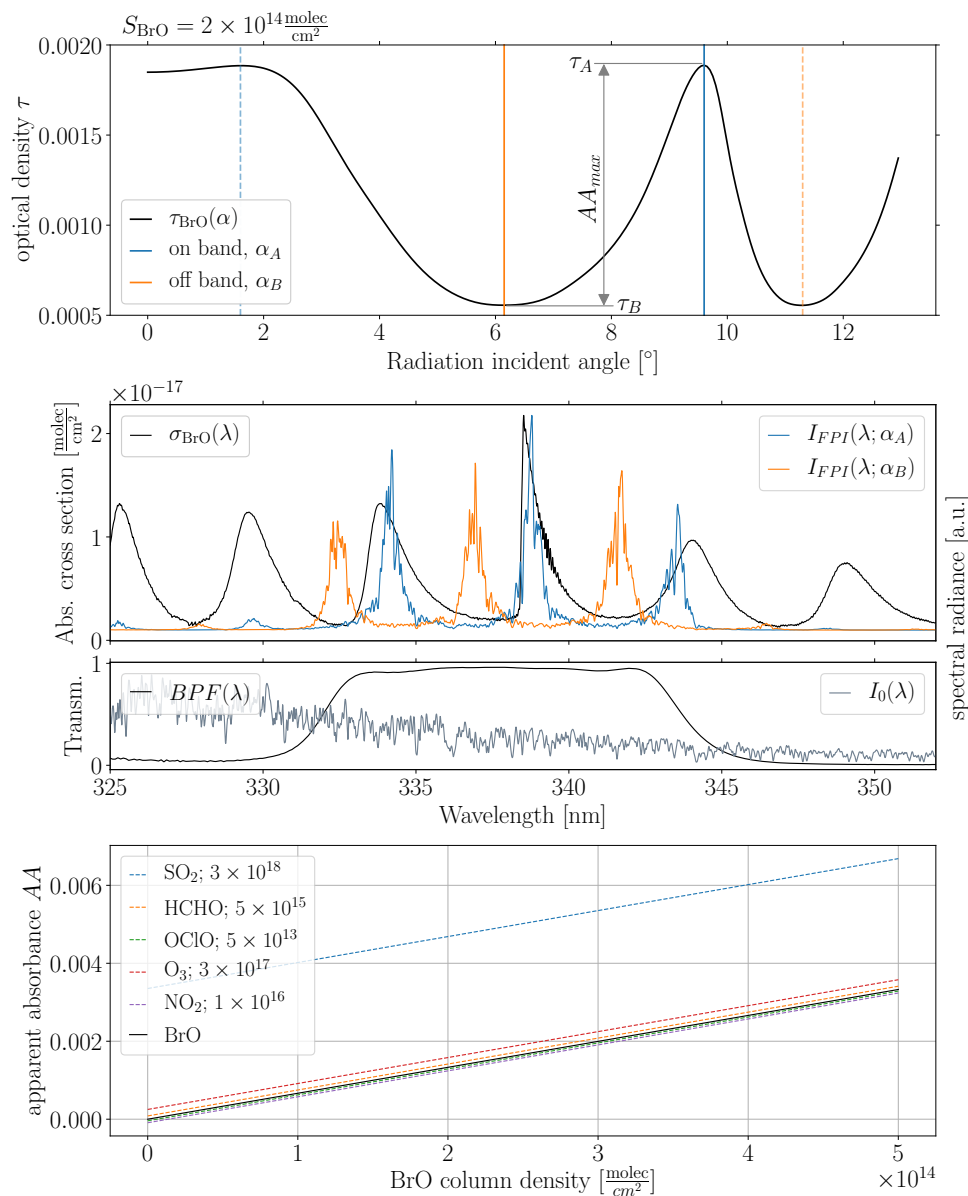


Figure A.2: Model results for BrO. Analogous to Figure 3.1. **upper panel:** The operating settings $\alpha_A = 9.6^\circ$ (drawn, blue line) and $\alpha_B = 6.15^\circ$ (drawn, orange line) resulting in a maximum apparent absorbance AA_{max} . **middle panels:** The recorded spectral radiances are shown for on-band (blue) and off-band (orange) setting in the upper middle panel, with corresponding filter transmission and incidence spectrum in the lower middle panel. **lower panel:** The calibration curve for BrO is shown (drawn line, black). Interfering species are included (dashed lines) with column densities in molec/cm². Strong SO₂ interference can be observed.

A.3 The inclination angle inside the etalon due to the FPI wedge angles

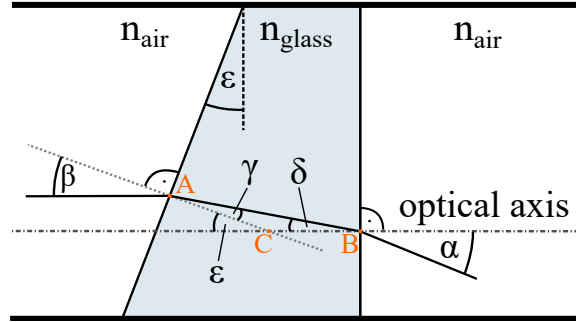


Figure A.3: Schematic of light traversing through the first fused silica plate of the FPI (drawn overstated for clarity). The wedge angle $\epsilon = 0.5^\circ$, incident angle β in respect to the surface orthonormal and the inclination angle α inside the etalon in respect to the optical axis.

Following Snell's law it is possible to devise two equations for the transitions at the interfaces

$$\begin{aligned} n_{\text{air}} \cdot \sin(\beta) &= n_{\text{glass}} \cdot \sin(\gamma) \Rightarrow \gamma = \arcsin(\tilde{n} \cdot \sin(\beta)) \\ n_{\text{glass}} \cdot \sin(\delta) &= n_{\text{air}} \cdot \sin(\alpha) \Rightarrow \delta = \arcsin(\tilde{n} \cdot \sin(\alpha)) \end{aligned} \quad (\text{A.8})$$

with angles α, β, γ and δ indicated in Figure A.3 and $\tilde{n} = n_{\text{air}}/n_{\text{glass}}$. Further the relation for the sum of angles of a triangle can be applied for $\triangle ABC$ yielding

$$\gamma + \delta + (180^\circ - \epsilon) = 180^\circ \Rightarrow \epsilon = \gamma + \delta. \quad (\text{A.9})$$

The Equations A.8 can now be inserted in Equation A.9 giving

$$\epsilon = \arcsin(\tilde{n} \cdot \sin(\beta)) + \arcsin(\tilde{n} \cdot \sin(\alpha)) \quad (\text{A.10})$$

This formula can now be arranged for β as following

$$\alpha = \arcsin\left(\frac{1}{\tilde{n}} \cdot \sin(\epsilon - \arcsin[\tilde{n} \cdot \sin(\beta)])\right) \quad (\text{A.11})$$

By applying the relation $\sin(x - \arcsin(y)) = \sin(x)\sqrt{1-y^2} - y \cdot \cos(x)$ and expansion of the product $1/n^*$ we finally get

$$\alpha = \arcsin\left(\sin(\epsilon) \cdot \sqrt{\frac{1}{\tilde{n}^2} - \sin^2(\beta)} - \sin(\beta) \cdot \cos(\epsilon)\right) \quad (\text{A.12})$$

which is equal to Equation 4.1 after inserting $\tilde{n} = n_{\text{air}}/n_{\text{glass}}$. Further the incident angle β in respect to the optical axis is given by $\beta_{\text{OA}} = \beta - \epsilon$.

B Lists

B.1 List of Figures

2.1	Attenuation of solar radiation through Earth's atmosphere	6
2.2	Absorption cross section of various species	9
2.3	DOAS principle	10
2.4	SO ₂ camera principle	13
2.5	Schematic of an FPI	16
2.6	FPI transmittance spectrum	17
2.7	FPI CS principle	19
3.1	Model results for SO ₂	26
3.2	Model results for BrO	28
3.3	Model results for HCHO	30
4.1	Image of the FPI	31
4.2	Schematic of the FPI setup	32
4.3	Shift of FPI transmission spectrum due to rotation	33
4.4	Determination of the FPI wedge angle alignment	34
4.5	Determination of the FPI zero position	35
4.6	Specification of the FPI plate distance	36
5.1	Setup of OP FPI instrument	38
5.2	Long-term measurement of the OP FPI electronic noise	39
5.3	Temperature dependency of the OP FPI output noise	40
5.4	Comparison of Xe-arc lamp and UV LED intensity fluctuations	41
5.5	HCHO gas cell images	42
5.6	Experimental setup of HCHO measurements by OP FPI	43
5.7	OP FPI interferograms	44
5.8	OP FPI interferograms of HCHO	45
5.9	Optical density of HCHO measurement with OP FPI	46
5.10	Two-position measurement of HCHO by OP FPI	47
5.11	Calibration curve of OP FPI	48
6.1	Schematic of the FPI camera optical system	51
6.2	Image of 2D UV detector and its quantum efficiency	53
6.3	Images of stepper motor and its controller board	55
6.4	Image of complete FPI camera setup	56
6.5	Tilt angle – stepper motor position calibration.	58

B Lists

6.6	Image and map of Mt. Etna measurement conditions	59
6.7	SO ₂ gas cell apparent absorbance	61
6.8	FPI camera apparent absorbance - column density calibration	62
6.9	FPI camera optical densities in on-band and off-band setting	63
6.10	Apparent absorbance of FPI camera measurements	64
6.11	Calibrated SO ₂ column density distribution measured	64
A.2	Model results for BrO using a filter with CW of 307 nm	72
A.3	Schematic of the FPI setup with wedge angle induced inclination	73

B.2 List of Tables

3.1	FPI and BPF parameters and differential column densities used in model.	24
6.1	Specification of the 2D UV detector	53
6.2	FPI camera parameters	54
6.3	Parts list of FPI camera	57
7.1	Sensitivities and detection limits	68

C Bibliography

- Aiuppa, A., Moretti, R., Federico, C., Giudice, G., Gurrieri, S., Liuzzo, M., Papale, P., Shinohara, H., and Valenza, M.: Forecasting Etna eruptions by real-time observation of volcanic gas composition, *Geology*, 35, 1115, <https://doi.org/10.1130/g24149a.1>, 2007.
- Aiuppa, A., Giudice, G., Gurrieri, S., Liuzzo, M., Burton, M., Caltabiano, T., McGonigle, A. J. S., Salerno, G., Shinohara, H., and Valenza, M.: Total volatile flux from Mount Etna, *Geophysical Research Letters*, 35, <https://doi.org/10.1029/2008gl035871>, 2008.
- Bluth, G. J. S., Shannon, J. M., Watson, I. M., Prata, A. J., and Realmuto, V. J.: Development of an ultra-violet digital camera for volcanic SO₂ imaging, *Journal of Volcanology and Geothermal Research*, 161, 47–56, <https://doi.org/10.1016/j.jvolgeores.2006.11.004>, 2007.
- Bobrowski, N. and Giuffrida, G.: Bromine monoxide / sulphur dioxide ratios in relation to volcanological observations at Mt. Etna 2006 - 2009, *Solid Earth*, 3, 433–445, <https://doi.org/10.5194/se-3-433-2012>, 2012.
- Bobrowski, N., Hönninger, G., Lohberger, F., and Platt, U.: IDOAS: a new monitoring technique to study the 2d distribution of volcanic gas emissions, *Journal of Volcanology and Geothermal Research*, 150, 329–338, <https://doi.org/10.1016/j.jvolgeores.2005.05.004>, 2006.
- Bobrowski, N., von Glasow, R., Aiuppa, A., Inguaggiato, S., Louban, I., Ibrahim, O. W., and Platt, U.: Reactive halogen chemistry in volcanic plumes, *Journal of Geophysical Research*, 112, <https://doi.org/10.1029/2006jd007206>, 2007.
- Bogumil, K., Orphal, J., Homann, T., Voigt, S., Spietz, P., Fleischmann, O. C., Vogel, A., Hartmann, M., Kromminga, H., Bovensmann, H., Frerick, J., and Burrows, J. P.: Measurements of molecular absorption spectra with the SCIAMACHY pre-flight model: instrument characterization and reference data for atmospheric remote-sensing in the 230-2380 nm region, *Journal of Photochemistry and Photobiology A: Chemistry*, 157, 167–184, [https://doi.org/10.1016/s1010-6030\(03\)00062-5](https://doi.org/10.1016/s1010-6030(03)00062-5), 2003.
- Carn, S. A., Clarisse, L., and Prata, A. J.: Multi-decadal satellite measurements of global volcanic degassing, *Journal of Volcanology and Geothermal Research*, 311, 99–134, <https://doi.org/10.1016/j.jvolgeores.2016.01.002>, 2016.

C Bibliography

- Chance, K. and Kurucz, R. L.: An improved high-resolution solar reference spectrum for earth's atmosphere measurements in the ultraviolet, visible, and near infrared, *Journal of Quantitative Spectroscopy and Radiative Transfer*, 111, 1289–1295, <https://doi.org/10.1016/j.jqsrt.2010.01.036>, 2010.
- Chance, K. and Orphal, J.: Revised ultraviolet absorption cross sections of HCO for the HITRAN database, *Journal of Quantitative Spectroscopy and Radiative Transfer*, 112, 1509–1510, <https://doi.org/10.1016/j.jqsrt.2011.02.002>, 2011.
- D'Aleo, R., Bitetto, M., Donne, D. D., Tamburello, G., Battaglia, A., Coltelli, M., Patanè, D., Prestifilippo, M., Scotto, M., and Aiuppa, A.: Spatially resolved SO₂ flux emissions from Mt Etna, *Geophysical Research Letters*, 43, 7511–7519, <https://doi.org/10.1002/2016gl069938>, 2016.
- Dekemper, E., Vanhamel, J., Opstal, B. V., and Fussen, D.: The AOTF-based NO₂ camera, *Atmospheric Measurement Techniques*, 9, 6025–6034, <https://doi.org/10.5194/amt-9-6025-2016>, 2016.
- Demtröder: *Experimentalphysik 2*, Springer Berlin Heidelberg, <https://doi.org/10.1007/978-3-642-29944-5>, 2013.
- Dickey, T. and Falkowski, P.: *The Sea, Biological-Physical Interactions in the Sea*, vol. 12, Wiley, 2002.
- Dinger, A. S., Stebel, K., Cassiani, M., Ardeshiri, H., Bernardo, C., Kylling, A., Park, S., Pisso, I., Schmidbauer, N., Wasseng, J., and Stohl, A.: Observation of turbulent dispersion of artificially released SO₂ puffs with UV cameras, *Atmospheric Measurement Techniques*, 11, 6169–6188, <https://doi.org/10.5194/amt-11-6169-2018>, 2018.
- EarthNullschool: Wind data for Mt. Etna on 22 July 2019 at pressure level of 700 hPa, <https://earth.nullschool.net>, accessed on 2019-11-19.
- EHD imaging GmbH: SCM2020-UV data sheet, <https://www.ehd.de/products/specialapplications/SCM2020-UV.pdf>, accessed on 2019-10-18.
- Fleischmann, O. C., Hartmann, M., Burrows, J. P., and Orphal, J.: New ultraviolet absorption cross-sections of BrO at atmospheric temperatures measured by time-windowing fourier transform spectroscopy, *Journal of Photochemistry and Photobiology A: Chemistry*, 168, 117–132, <https://doi.org/10.1016/j.jphotochem.2004.03.026>, 2004.
- Gliß, J., Bobrowski, N., Vogel, L., Pöhler, D., and Platt, U.: OClO and BrO observations in the volcanic plume of Mt. Etna - implications on the chemistry of chlorine and bromine species in volcanic plumes, *Atmospheric Chemistry and Physics*, 15, 5659–5681, <https://doi.org/10.5194/acp-15-5659-2015>, 2015.

- Gliß, J., Stebel, K., Kylling, A., Dinger, A., Sihler, H., and Sudbø, A.: Pyplis - A Python Software Toolbox for the Analysis of SO₂ Camera Images for Emission Rate Retrievals from Point Sources, *Geosciences*, 7, 134, <https://doi.org/10.3390/geosciences7040134>, 2017.
- Grainger, J. F. and Ring, J.: Anomalous Fraunhofer Line Profiles, *Nature*, 193, 762–762, <https://doi.org/10.1038/193762a0>, 1962.
- Griffin, D., Zhao, X., McLinden, C. A., Boersma, F., Bourassa, A., Dammers, E., Degenstein, D., Eskes, H., Fehr, L., Fioletov, V., Hayden, K., Kharol, S. K., Li, S., Makar, P., Martin, R. V., Mihele, C., Mittermeier, R. L., Krotkov, N., Snee, M., Lamsal, L. N., ter Linden, M., van Geffen, J., Veefkind, P., and Wolde, M.: High-Resolution Mapping of Nitrogen Dioxide With TROPOMI: First Results and Validation Over the Canadian Oil Sands, *Geophysical Research Letters*, 46, 1049–1060, <https://doi.org/10.1029/2018gl081095>, 2019.
- Hansen, J., Ruedy, R., Sato, M., and Reynolds, R.: Global surface air temperature in 1995: Return to pre-Pinatubo level, *Geophysical Research Letters*, 23, 1665–1668, <https://doi.org/10.1029/96gl01040>, 1996.
- Kantzas, E. P., McGonigle, A. J. S., Tamburello, G., Aiuppa, A., and Bryant, R. G.: Protocols for UV camera volcanic SO₂ measurements, *Journal of Volcanology and Geothermal Research*, 194, 55–60, <https://doi.org/10.1016/j.jvolgeores.2010.05.003>, 2010.
- Kaur, S. and Singh, R. S. S.: An Efficient Method for Periodic Vertical Banding Noise removal in Satellite Images, in: *International Journal on Computer Science and Engineering*, 2012.
- Kern, C., Lübcke, P., Bobrowski, N., Campion, R., Mori, T., Smekens, J., Stebel, K., Tamburello, G., Burton, M., Platt, U., and Prata, F.: Intercomparison of SO₂ camera systems for imaging volcanic gas plumes, *Journal of Volcanology and Geothermal Research*, 300, 22–36, <https://doi.org/10.1016/j.jvolgeores.2014.08.026>, 2015.
- Khokhar, M. F., Frankenberg, C., Roozendaal, M. V., Beirle, S., Kühl, S., Richter, A., Platt, U., and Wagner, T.: Satellite observations of atmospheric SO₂ from volcanic eruptions during the time-period of 1996 - 2002, *Advances in Space Research*, 36, 879–887, <https://doi.org/10.1016/j.asr.2005.04.114>, 2005.
- Klein, A., Lübcke, P., Bobrowski, N., Kuhn, J., and Platt, U.: Plume propagation direction determination with SO₂ cameras, *Atmospheric Measurement Techniques*, 10, 979–987, <https://doi.org/10.5194/amt-10-979-2017>, 2017.
- Kuhn, J.: Fernerkundung von Schwefeldioxid mit einem Fabry-Perot-Interferometer, Bachelor's thesis, Institute of Environmental Physics, Ruprecht-Karls University of Heidelberg, 2012.

C Bibliography

- Kuhn, J.: Trace gas imaging in the atmosphere with a fabry-pérot interferometer - a case study for sulfur dioxide, Master's thesis, Institute of Environmental Physics, Ruprecht-Karls University of Heidelberg, 2015.
- Kuhn, J., Bobrowski, N., Lübcke, P., Vogel, L., and Platt, U.: A Fabry-Perot interferometer-based camera for two-dimensional mapping of SO₂ distributions, *Atmospheric Measurement Techniques*, 7, 3705–3715, <https://doi.org/10.5194/amt-7-3705-2014>, 2014.
- Kuhn, J., Platt, U., Bobrowski, N., and Wagner, T.: Towards imaging of atmospheric trace gases using Fabry-Perot interferometer correlation spectroscopy in the UV and visible spectral range, *Atmospheric Measurement Techniques*, 12, 735–747, <https://doi.org/10.5194/amt-12-735-2019>, 2019.
- Lübcke, P., Bobrowski, N., Illing, S., Kern, C., Nieves, J. M. A., Vogel, L., Zielcke, J., Granados, H. D., and Platt, U.: On the absolute calibration of SO₂ cameras, *Atmospheric Measurement Techniques*, 6, 677–696, <https://doi.org/10.5194/amt-6-677-2013>, 2013.
- Lübcke, P., Bobrowski, N., Arellano, S., Galle, B., Garzón, G., Vogel, L., and Platt, U.: BrO/SO₂ molar ratios from scanning DOAS measurements in the NOVAC network, *Solid Earth*, 5, 409–424, <https://doi.org/10.5194/se-5-409-2014>, 2014.
- Leue, C., Wenig, M., Wagner, T., Klimm, O., Platt, U., and Jähne, B.: Quantitative analysis of NO_x Emissions from Global Ozone Monitoring Experiment satellite image sequences, *Journal of Geophysical Research: Atmospheres*, 106, 5493–5505, <https://doi.org/10.1029/2000jd900572>, 2001.
- Lohberger, F., Hönninger, G., and Platt, U.: Ground-based imaging differential optical absorption spectroscopy of atmospheric gases, *Applied Optics*, 43, 4711, <https://doi.org/10.1364/ao.43.004711>, 2004.
- Louban, I., Bobrowski, N., Rouwet, D., Inguaggiato, S., and Platt, U.: Imaging DOAS for volcanological applications, *Bulletin of Volcanology*, 71, 753–765, <https://doi.org/10.1007/s00445-008-0262-6>, 2009.
- Manago, N., Takara, Y., Ando, F., Noro, N., Suzuki, M., Irie, H., and Kuze, H.: Visualizing spatial distribution of atmospheric nitrogen dioxide by means of hyperspectral imaging, *Applied Optics*, 57, 5970, <https://doi.org/10.1364/ao.57.005970>, 2018.
- Mori, T. and Burton, M.: The SO₂ camera: A simple, fast and cheap method for ground-based imaging of SO₂ in volcanic plumes, *Geophysical Research Letters*, 33, <https://doi.org/10.1029/2006gl027916>, 2006.
- Nanotec: Stepper motor manufactured by Nanotec GmbH & CO. KG, <https://en.nanotec.com/products/460-st4209s1006-a/>, accessed 2019-10-19.

- NOAA: Monthly average of Maona Loa CO₂ concentration, <https://www.esrl.noaa.gov/gmd/ccgg/trends/>, accessed on 2019-11-21.
- OpenTopoMap: Kartendaten: © OpenStreetMap-Mitwirkende, SRTM | Kartendarstellung: © OpenTopoMap (CC-BY-SA), <https://opentopomap.org/>, accessed 2019-11-18.
- Oppenheimer, C., Fischer, T. P., and Scaillet, B.: Volcanic Degassing: Process and Impact, in: *Treatise on Geochemistry*, pp. 111–179, Elsevier, <https://doi.org/10.1016/b978-0-08-095975-7.00304-1>, 2014.
- Perot, A. and Fabry, C.: On the application of interference phenomena to the solution of various problems of spectroscopy and metrology, *The Astrophysical Journal*, 9, 87, <https://doi.org/10.1086/140557>, 1899.
- Platt, U. and Stutz, J.: *Differential Optical Absorption Spectroscopy*, Springer Berlin Heidelberg, <https://doi.org/10.1007/978-3-540-75776-4>, 2008.
- Platt, U., Lübcke, P., Kuhn, J., Bobrowski, N., Prata, F., Burton, M., and Kern, C.: Quantitative imaging of volcanic plumes - Results, needs, and future trends, *Journal of Volcanology and Geothermal Research*, 300, 7–21, <https://doi.org/10.1016/j.jvolgeores.2014.10.006>, 2015.
- Polyanskiy, M. N.: Refractive index database, <https://refractiveindex.info>, accessed on 2019-09-13.
- Roedel, W. and Wagner, T.: *Physik unserer Umwelt: Die Atmosphäre*, Springer Berlin Heidelberg, <https://doi.org/10.1007/978-3-662-54258-3>, 2017.
- Roscoe, H. K., Roozendael, M. V., Fayt, C., du Piesanie, A., Abuhassan, N., Adams, C., Akrami, M., Cede, A., Chong, J., Clémer, K., Friess, U., Ojeda, M. G., Goutail, F., Graves, R., Griesfeller, A., Grossmann, K., Hemerijckx, G., Hendrick, F., Herman, J., Hermans, C., Irie, H., Johnston, P. V., Kanaya, Y., Kreher, K., Leigh, R., Merlaud, A., Mount, G. H., Navarro, M., Oetjen, H., Pazmino, A., Perez-Camacho, M., Peters, E., Pinardi, G., Puentedura, O., Richter, A., Schönhardt, A., Shaiganfar, R., Spinei, E., Strong, K., Takashima, H., Vlemmix, T., Vrekoussis, M., Wagner, T., Wittrock, F., Yela, M., Yilmaz, S., Boersma, F., Hains, J., Kroon, M., Piters, A., and Kim, Y. J.: Intercomparison of slant column measurements of NO and O₄ by MAX-DOAS and zenith-sky UV and visible spectrometers, *Atmospheric Measurement Techniques*, 3, 1629–1646, <https://doi.org/10.5194/amt-3-1629-2010>, 2010.
- Saiz-Lopez, A. and von Glasow, R.: Reactive halogen chemistry in the troposphere, *Chemical Society Reviews*, 41, 6448, <https://doi.org/10.1039/c2cs35208g>, 2012.
- Salerno, G. G., Burton, M. R., Oppenheimer, C., Caltabiano, T., Randazzo, D., Bruno, N., and Longo, V.: Three-years of SO₂ flux measurements of Mt. Etna using an automated UV scanner array: Comparison with conventional traverses and

C Bibliography

- uncertainties in flux retrieval, *Journal of Volcanology and Geothermal Research*, 183, 76–83, <https://doi.org/10.1016/j.jvolgeores.2009.02.013>, 2009.
- Seinfeld, J. H. and Pandis, S. N.: *Atmospheric Chemistry and Physics*, John Wiley & Sons Inc, URL https://www.ebook.de/de/product/25599491/john_h_seinfeld_spyros_n_pandis_atmospheric_chemistry_and_physics.html, 2016.
- Serdyuchenko, A., Gorshelev, V., Weber, M., Chehade, W., and Burrows, J. P.: High spectral resolution ozone absorption cross-sections - Part 2: Temperature dependence, *Atmospheric Measurement Techniques*, 7, 625–636, <https://doi.org/10.5194/amt-7-625-2014>, 2014.
- Sihler, H., Kern, C., Pöhler, D., and Platt, U.: Applying light-emitting diodes with narrowband emission features in differential spectroscopy, *Optics Letters*, 34, 3716, <https://doi.org/10.1364/ol.34.003716>, 2009.
- Solomon, S., Schmeltekopf, A. L., and Sanders, R. W.: On the interpretation of zenith sky absorption measurements, *Journal of Geophysical Research*, 92, 8311, <https://doi.org/10.1029/jd092id07p08311>, 1987.
- Tirpitz, J. L.: *Optical in-situ sulfur dioxide measurementsbin different volcanic applications*, Master's thesis, Institute of Environmental Physics, Ruprecht-Karls University of Heidelberg, 2016.
- Vandaele, A. C., Hermans, C., and Fally, S.: Fourier transform measurements of SO₂ absorption cross sections: II., *Journal of Quantitative Spectroscopy and Radiative Transfer*, 110, 2115–2126, <https://doi.org/10.1016/j.jqsrt.2009.05.006>, 2009.
- Warnach, S., Sihler, H., Borger, C., Bobrowski, N., Hörmann, C., Beirle, S., Schöne, M., Platt, U., and Wagner, T.: Bromine monoxide measurements in volcanic plumes from S5-P/Tropomi, in: *EGU General Assembly Conference Abstracts*, vol. 20, p. 15519, 2018.
- Warnach, S., Bobrowski, N., Hidalgo, S., Arellano, S., Sihler, H., Dinger, F., Lübcke, P., Battaglia, J., Steele, A., Galle, B., Platt, U., and Wagner, T.: Variation of the BrO/SO₂ Molar Ratio in the Plume of Tungurahua Volcano Between 2007 and 2017 and Its Relationship to Volcanic Activity, *Frontiers in Earth Science*, 7, <https://doi.org/10.3389/feart.2019.00132>, 2019.
- Zhang, M., Carder, K., Muller-Karger, F. E., Lee, Z., and Goldgof, D. B.: Noise Reduction and Atmospheric Correction for Coastal Applications of Landsat Thematic Mapper Imagery, *Remote Sensing of Environment*, 70, 167–180, [https://doi.org/10.1016/s0034-4257\(99\)00031-0](https://doi.org/10.1016/s0034-4257(99)00031-0), 1999.

Danksagungen

Zuerst möchte ich mich bei Prof. Ulrich Platt bedanken, der es mir ermöglicht hat an diesem faszinierenden und spannenden Thema arbeiten zu dürfen und mir mit seinem Fachwissen bei kniffligen Fragen immer zur Seite stand. Zudem möchte ich mich bedanken, dass ich an vielen Reisen ob zu Konferenzen, Messkampagnen oder Sommerschulen teilnehmen konnte.

Des Weiteren möchte ich mich bei Prof. Thomas Wagner bedanken für die unkomplizierte Übernahme der Zweitkorrektur meiner Masterarbeit.

Ein gewaltig großer Dank geht an Jonas, für die großartige Betreuung, die er geleistet hat, für seine stetige Bereitschaft zur Hilfe und Korrekturen, seiner Motivation, dem Wissen und den Anregungen für das Projekt, welche es zu dem gemacht haben was es ist. Und natürlich möchte ich mich auf für die vielen spannenden und lustigen Momenten ob am IUP, im Zug nach Sizilien oder auf dem Gipfel des Ätna bedanken. Ich habe wirklich viel von dir gelernt!

Ein weiterer großer Dank geht auch an Nicole. Als ausgezeichnete Bergführerin hat sie mich vier Mal auf den Ätna (mit Lava-Fountain) und einmal auf den Stromboli geführt - und auch wieder heil heruntergebracht! Durch Ihre Expertise und unerschöpflichen Begeisterung für und rund um Vulkane hat sie auch ich mir eine noch größere Faszination dafür erwecken können. Natürlich bedanke ich mich auch für jegliche Hilfestellungen und Korrekturen, ob an Abstracts oder eben dieser Arbeit.

Vielen Dank auch an Stefan, der es ermöglicht hat sich für eine Woche in sein Projekt einzuklinken und mir die Macht von Oreo-White-Choc als Motivator zeigte.

Natürlich möchte ich mich auch bei Lukas, Stefan und Simon für die Unterstützung beim Korrekturlesen bedanken.

Danke auch an die gesamte Arbeitsgruppe Atmosphäre für die entspannte und angenehme Atmosphäre - höhö.

Danke an das Büro 326, für die vielen nichtphysikalischen Diskussionen, witzigen Momenten, Formulierungshilfen und natürlich Clementinen in der finalen Phase dieser Arbeit.

Danke an alle meine Freunde für die Motivation, Zeit für Kaffeepausen und Ausgleich zum Uni-Alltag.

Vielen dank auch an meine WG, Vanessa und Kathi, die sich einige Probevorträge anhören mussten und es immer wieder geschafft haben mich in stressigen Phasen zu motivieren oder ausgezeichnet zu bekochen.

Zu guter Letzt, möchte ich meiner Familie Danken, meine Eltern Wolfgang und Lola, und meinen Schwestern Saskia und Corinna, für die konstante bedingungslose Unterstützung, nicht nur bei dieser Arbeit, sondern während meines ganzen Studiums.

Erklärung:

Ich versichere, dass ich diese Arbeit selbstständig verfasst habe und keine anderen als die angegebenen Quellen und Hilfsmittel benutzt habe.

Heidelberg, den 2. Dezember 2019

.....